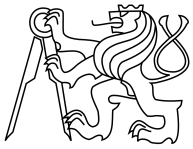

České vysoké učení technické v Praze
Fakulta jaderná a fyzikálně inženýrská

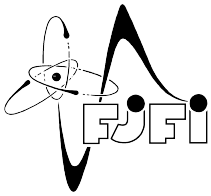

Simulace chování tepelného štítu divertoru z tekutých kovů tokamaku COMPASS Upgrade

Simulation of behavior of liquid metal divertor heat shield on tokamak COMPASS Upgrade

Diplomová práce
Master's thesis

Autor: **Bc. Jan Čečrdle**

Vedoucí práce: **Res. Prof. Mgr. Jan Horáček, Dr. és sc.**

Akademický rok: 2020/2021

Zadání

Prohlášení

Prohlašuji, že jsem svou diplomovou práci vypracoval samostatně a použil jsem pouze podklady (literaturu, projekty, SW atd.) uvedené v přiloženém seznamu.
Nemám závažný důvod proti použití tohoto školního díla ve smyslu § 60 Zákona č. 121/2000 Sb., o právu autorském, o právech souvisejících s právem autorským a o změně některých zákonů (autorský zákon).

V Praze dne ....

Bc. Jan Čečrdle

Název práce:

Simulace chování tepelného štítu divertoru z tekutých kovů tokamaku COMPASS Upgrade

Autor: Bc. Jan Čečrdle

Obor: Fyzika a technika termojaderné fúze

Druh práce: Diplomová práce

Vedoucí práce: Res. Prof. Mgr. Jan Horáček, Dr. és sc., Ústav fyziky plazmatu AV ČR, v.v.i.

Abstrakt: Problém přehřívání první stěny fúzních zařízení, je cílem výzkumu již několik desetiletí. Rešení tohoto problému, které by bezpečně splňovalo veškeré přísné požadavky, stanovené vysokou specificitou a citlivostí prostředí fúzních zařízení, se stále nepodařilo najít. Možným řešením této otázky, jsou technologie stěn z tekutých kovů. Stěna z tekutého kovu s sebou nese několik zásadních výhod oproti současně využívaným pevným materiálům. Nicméně právě tekutost těchto materiálů s sebou přináší nové výzvy a problémy, které je nutné před jejich implementací vyřešit. Jedním ze zařízení, kde se použitelnost stěn z tekutých kovů bude zkoumat bude tokamak COMPASS Upgrade. Tato práce se zabývá simulacemi chování tepelného štítu z tekutých kovů na tomto zařízení.

Klíčová slova: tokamak, COMPASS-U, divertor, tekuté kovy, kapilární porézní systém, litium, cín

Title:

Simulation of behavior of liquid metal divertor heat shield on tokamak COMPASS Upgrade

Document type: Master's thesis

Author: Bc. Jan Čečrdle

Supervisor: Res. Prof. Mgr. Jan Horáček, Dr. és sc., Institute of Plasma Physics of the CAS.

Abstract: The problem of first wall overheating has been the object of interest of the fusion research community for several decades. A solution sufficiently meeting the strict requirements set by the high specificity and sensitivity of the fusion devices has not been found yet. A possible candidate for the future heat shield is the technology based on liquid metals. A liquid metal wall has several advantages over currently used solid ones. However, the liquid state of the wall brings new challenges and obstacles, that have to be overcome before its implementation. One of the devices, where the viability of the liquid metal first wall will be tested will be the COMPASS Upgrade tokamak. This thesis focuses on simulations of the COMPASS Upgrade liquid metal heat shield behavior.

Key words: tokamak, COMPASS-U, divertor, liquid metals, capillary porous system, lithium, tin

Poděkování:
Děkuji mému školiteli Res. Prof. Mgr. Janu Horáčkovi Dr ès sc. za ochotné a trpělivé vedení diplomové práce. Dále děkuji kolegům z Institutu fyziky plazmatu a dalších institucí za přínosnou spolupráci a užitečné rady, jmenovitě zejména Mgr. Michaelovi Kommovi, Ph.D. a Dr. Davidu Tskhakayovi. Mnohokrát děkuji celé mé rodině, která mě v mých studiích podporovala.

I would also like to express my deep gratitude to Dr. Jacob Schwartz for his helpful calculations, crucial for the completion of the work in this thesis.

Publications

The work in this thesis is part of the following publications, which I am a co-author of:

- **J. Horáček, et al., Modeling of COMPASS tokamak divertor liquid metal experiments**
  Published in: *Nuclear Materials and Energy*, Vol. 25, 2020,
  `https://doi.org/10.1016/j.nme.2020.100860`
  and presented at The 24th International Conference on Plasma Surface Interaction in Fusion Devices, ICC Jeju, South Korea, 2020

- **R. Dejarnac, et al., Overview of power exhaust experiments in the COMPASS divertor with liquid metals**
  Published in *Nuclear Materials and Energy*, Vol. 25, 2020
  `https://doi.org/10.1016/j.nme.2020.100801`
  and presented at The 24th International Conference on Plasma Surface Interaction in Fusion Devices, ICC Jeju, South Korea, 2020

- **J. Horáček et al., Predictive modelling of liquid metal divertor: from COMPASS tokamak towards Upgrade**
  Submitted to: *Physica Scripta*, 2021
  and presented at The 18th International Conference on Plasma-Facing Materials and Components for Fusion Applications, Forschungszentrum Jülich, Jülich Germany, 2021

Contents

Introduction

Suitable solution for utilization of fusion power for energy production has been an objective of the scientific community for more than seventy years. The first idea of fusion energy as an energy source has been proposed in 1920, more than a hundred years ago, by Sir Arthur Eddington. This energy source would provide a cheap, safe, and clean power with practically inexhaustible fuel sources available all over the world. Transition to such technology could dramatically change the human society and even cause another industrial revolution. However, achieving control over thermonuclear fusion bears its difficulties, one of which is the confinement of the heated plasma in which the fusion reactions occur. In the last decades the most promising solution to this problem is the idea to confine the plasma with strong magnetic fields called Magnetic confinement. This idea resulted in several designs with various magnetic field configurations. The most auspicious design is the Tokamak. One of the key obstacles on the way to a workable power plant is the problem of heat loads on wall of the vessel. As the plasma needs to be heated to temperatures an order of magnitude higher than in the core of the Sun and substantial amount of energy is confined in the plasma, an immense heat load is deposited on the wall of the vessel. Recent experimental and simulation research shows, not even the best materials currently known and used will be able to provide reliable protection to the wall. To address this problem heat shield technologies based on liquid rather than solid metals are being developed and tested. For the liquid metal no risk of lattice disruption is possible. If the liquid metal is confined in a material with a higher melting temperature, the evaporation of the liquid prevents the heat shield from reaching dangerously high temperature, that would damage the solid parts of the shield. The capillary porous structure based heat shields, where the liquid is held by capillary forces, have been successfully tested in several linear devices and tokamaks. After the successful campaign with liquid metals on the COMPASS tokamak, an experiment at COMPASS-U, the successor of COMPASS, is a logical next step. Higher heat loads and longer discharges will allow an equilibrium between incoming heat-flux from the plasma and the cooling effects. This equilibrium state will be a much better base for an extrapolation of the LMD behavior at larger tokamaks and potential power plants (such as DEMO). Such experiments are of course not an easy endeavor, therefore comprehensive simulations are required for a proper preparation to be done. For the purposes of these proposed experiments, first with a small divertor target with a prospect for a full liquid divertor in the future, simulations in the 3DHeat have been conducted, to better predict the power handling and overall behavior of the liquid divertor during the COMPASS-U discharges.

This thesis summarizes the currently prospective liquid metal divertor technologies, describes the 3DHeat code and its applications, presents the results of the COMPASS-U and ALIMAT-F liquid metal experiments simulations and draws a conclusion towards the liquid metal divertor applications, based on these results.

1. Fusion Plasma Physics

1.1 Definition of plasma

Plasma is a system, where charged particles are present with the amount of positive and negative charge in a macroscopic volume being the same, making the plasma appear neutral as a whole. This characteristic is called quasi-neutrality. The presence of charged particles makes the plasma react to an electric or a magnetic field as a whole and contributes to their creation. For these distinct differences from solids, liquids and gasses, plasma is sometimes called "The fourth state of matter". Plasma can be classified by several characteristics (relativistic/non-relativistic, quantum/classical, high/low temperature etc.). Even though metals or exotic types of matter (i.e. cores of stars) fulfill the definition of plasma, the term is most commonly used for high temperature ionized gasses, as is also the case for this thesis, which is concerned with utilization of high temperature plasma as a basis for fusion energy production [1].

1.2 Thermonuclear fusion

In 1920 Sir Arthur Eddington speculated, that thermonuclear fusion reactions are the source of the Suns energy [2]. Thermonuclear fusion is a reaction between two light element nuclei resulting in a creation of different elements and release of energy. This process is the source of energy in stars. The repulsive force between two positively charged nuclei creates a strong requirement for the thermal energy and/or density of the matter if efficient fusion energy production is required. Typically, a certain threshold of the temperature-density product has to be surpassed for a required number of reactions per time to occur [1].

1.2.1 Deuterium-tritium fusion

For an artificial fusion energy source, the most accessible reaction is the Deuterium-tritium (D-T) reaction. In this reaction deuterium and tritium nuclei fuse with the creation of a helium nucleus and a neutron, while $\varepsilon_{\mathrm{D-T}} = 17.6$ MeV of energy is released

$$ {}^{2}_{1}\mathrm{D} \; + \; {}^{3}_{1}\mathrm{T} \; \rightarrow \; {}^{4}_{2}\mathrm{He} \; + \; {}^{1}_{0}\mathrm{n} + 17.6 \text{ MeV}. \tag{1.1} $$

Even though is not the only plausible reaction for Earth-based fusion energy production, it is the most easily manageable one as the cross-section/reactivity of the D-T reaction is the most favorable. The peak of the reactivity is the highest and localized at a relatively low temperature in comparison to other possible reactions as seen in Fig. 1.1 [1, 3].

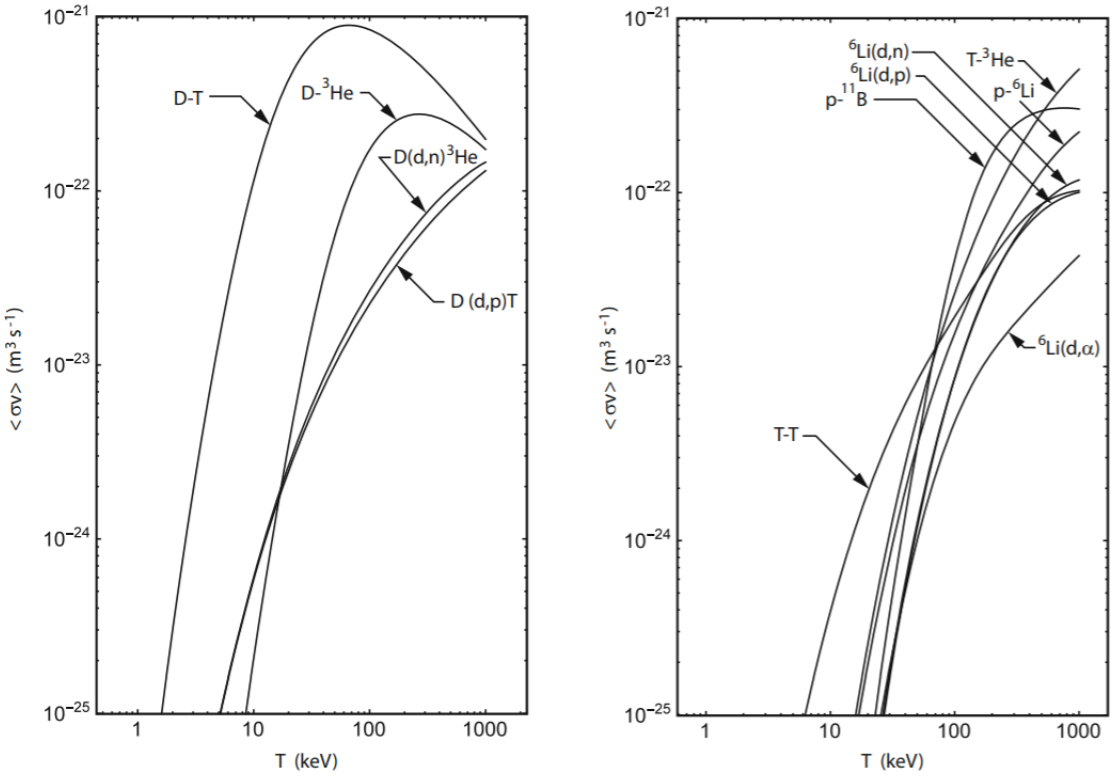

Fig. 1.1: Maxwellian-averaged reactivities $\langle \sigma v \rangle$ for fusion reactions among the light nuclides [3].

The reactivity is however not the only relevant parameter as other crucial effects apart from the nuclear reactions, such as radiative cooling, occur. To correctly assess the "ideal" conditions for a fusion reactor operation other effects, such as radiative cooling have to be considered. The Lawson criterion gives the general energy balance requirements of a fusion power plant. As a certain amount of power is required to sustain the fusion reactions, part of the power recirculates in the power plant. Because the re-circulation is not done with a 100 per cent efficiency, the losses have to be considered as well (Fig. 1.2).

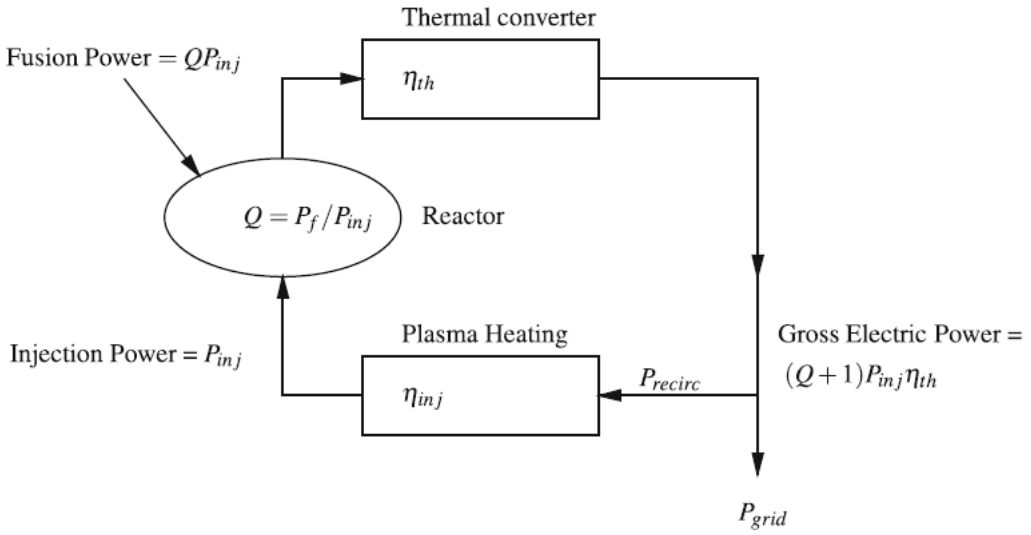

Fig. 1.2: Fusion power plant energy balance. Courtesy of [3].

The most general form of the power balance is given by the total plasma energy W_{P}, the input heating power P_{H}, the fusion power P_{f} and the power of losses P_{L} as:

$$\frac{\mathrm{d}W_{\mathrm{P}}}{\mathrm{d}t} = P_{\mathrm{H}} + P_{\mathrm{f}} - P_{\mathrm{L}}. \tag{1.2}$$

For a magnetically confined D-T plasma the balance can be expanded with:

- **Fusion power** being equal to the power from charged (confined) fusion products - alpha particles in case of D-T carrying 1/5 of the fusion power. For density n in a volume V the power is $P_{\mathrm{f}} = P_{\alpha} = \frac{1}{5}P_{\mathrm{D-T}} = \frac{1}{20}\overline{n^2 \langle \sigma v \rangle}\varepsilon_{\mathrm{D-T}}V$.
- **Plasma energy** is equal to the total energy of all N particles $W_{\mathrm{P}} = 3k_{\mathrm{B}}TN$.
- Energy losses can be expressed as $P_{\mathrm{L}} = \frac{W_{\mathrm{P}}}{\tau_{\mathrm{E}}}$, where τ_{E} is the energy confinement time in seconds.

The energy balance equation is then

$$\frac{\mathrm{d}3nk_{\mathrm{B}}T}{\mathrm{d}t} = P_{\mathrm{H}} - \frac{nk_{\mathrm{B}}T}{\tau_{\mathrm{E}}} + \frac{1}{20}\overline{n^2 \langle \sigma v \rangle}\varepsilon_{\mathrm{D-T}}V. \tag{1.3}$$

and adjusted so that

$$n\tau_{\mathrm{E}} \geq f(T). \tag{1.4}$$

It has to be noted, that the ideal conditions for a fusion power plant are not entirely given by the reactivity of the fuel. The maximum of D-T reactivity is at 60 keV (Fig. 1.1), but the Lawson criterion (1.4) gives the ideal temperature of 30 keV. This is due to the fact, that not only the reactivity, but also the energy confinement time and density are temperature dependent i.e., higher temperature means not only higher fusion power, but also higher power losses.

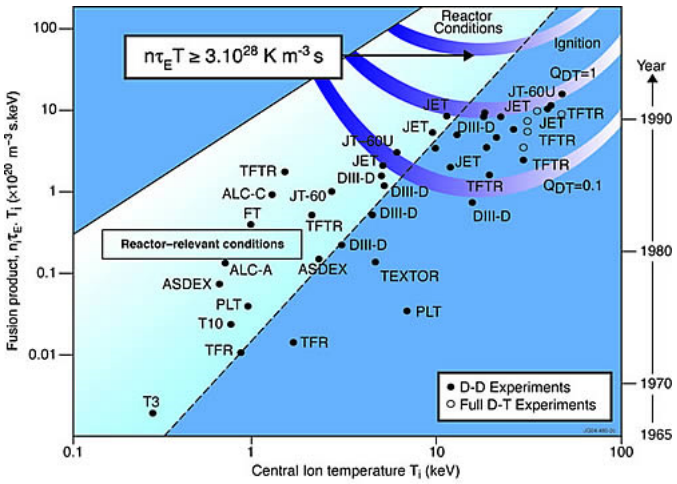

Fig. 1.3: The evolution of maximal fusion triple product $n\tau_E T$ for D-T fusion power for various fusion devices over time. Courtesy of [4].

For the specific conditions of a D-T fusion power plant the so called fusion triple product $n\tau_E T$ is used to derive the ideal conditions of the fusion power plant ($T = 10 - 20$ keV). The fusion triple product is depicted in Fig 1.3. In order to achieve ignition (production of fusion power without external heating) with D-T fusion the condition for triple product is [1, 3, 5]

$$n\tau_E T \geq 3 \times 10^{21} \ [\mathrm{m}^{-3}\mathrm{keVs}]. \tag{1.5}$$

1.3 Magnetic confinement

Crucial in fusion energy production is the confinement of the heated plasma. As the optimal temperatures range from 100-150 million K, substantial measures are needed to confine the plasma at required parameters for sufficient energy confinement time of few seconds and to keep it from damaging the confinement vessel. Assuming the ideal temperature in range $T = 10 - 20$ keV, discussed in the previous section, the condition gives a minimum value of the $n\tau_E$ product. This condition can be approached from both sides. Either have a reaction at large density with a short confinement time, called *inertial confinement*, essentially a controlled fusion explosion or have a low-density reaction with long confinement time (in seconds). A "middle way" of moderate density and moderate confinement time is also possible [3]. This thesis focuses on the problems and solutions in the second approach, low density, and long confinement. As the fuel in the fusion reactor needs to be heated to tens of thousands of electron volts (hundreds of millions of kelvin), it is always in plasmatic state. This fact can be utilized, as the ionized particles are subjected to electromagnetic forces. A carefully designed field will confine the particles away from the wall of the fusion vessel. This approach is called *magnetic confinement*.

Magnetic confinement is an approach to confine plasma in an equilibrium of magnetic and thermal pressure. Historically several designs have been tested, such as magnetic mirrors, pinches (both linear and circular) and other more exotic designs. Currently the most promising and tested design is the tokamak. [3, 5, 1].

1.3.1 Tokamak

Tokamak is the most successful reactor design utilizing the magnetic confinement approach. Tokamak is an abbreviation of the Russian name meaning *Toroidal vessel with magnetic fields*. The most basic shape of a tokamak plasma is the torus with the major radius R and minor radius r. With the aim to increase the performance, the shape of the plasma can be different from a perfect torus (e.g. D-shaped, spherical). If the particles were confined only by a magnetic field in the toroidal direction (toroidal magnetic field) a resulting particle drift would prohibit any particle confinement. A second, poloidal component of the magnetic field is necessary to create a helical total field, negating the drift. In tokamaks, toroidal field $\mathbf{B}_\mathrm{t}$ is created by toroidal coils and poloidal field $\mathbf{B}_\mathrm{p}$ by induced plasma current. A diagram of a tokamak can be seen on Fig. 1.4 [1, 5, 3].

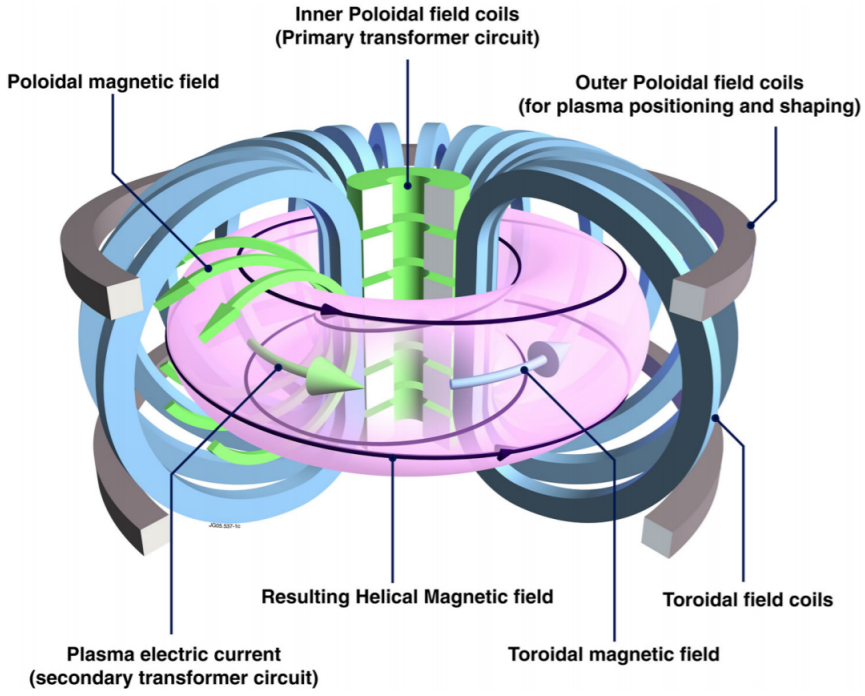

Fig. 1.4: A scheme of a tokamak showing the magnetic fields created by the coils and plasma current [6].

1.3.2 Safety factor

In tokamak physics a general quantity called *Safety factor* is used to describe the ratio between $\mathbf{B}_\mathrm{t}$ and $\mathbf{B}_\mathrm{p}$. The most generalized formula is

$$q = \frac{\mathrm{d}\Phi}{\mathrm{d}\Psi}, \tag{1.6}$$

where Φ is the toroidal and Ψ the poloidal magnetic induction flux. For a circular plasma, safety factor can be written as

$$q \approx \frac{rB_t}{RB_p}. \tag{1.7}$$

The main importance of the safety factor is, that if the value at the last closed flux surface is below 2, the plasma is magneto-hydrodynamically unstable. Safety factor can be described as "Number of toroidal circulations per one poloidal" done by a particle. It is therefore a toroidally symmetrical

quantity, therefore defined for each individual flux surface. In its nature the safety factor can be written as a dimensionless quantity and is often expressed as a function of minor radius (q(r)), because of the field variation across the poloidal cross section. Because of this, and also because it carries useful information about the magnetic field, it is used as one of the comparative quantities between all tokamaks. If the magnetic field has an X-point (see. section 1.4.2), the safety factor would reach infinity at LCFS. As this would be a nonsensical value, the q_{95} quantity has been introduced. This is the safety factor at the surface enclosing 95 % of the toroidal flux. In most tokamaks in current operation regimes $q_{95} \approx 3$.

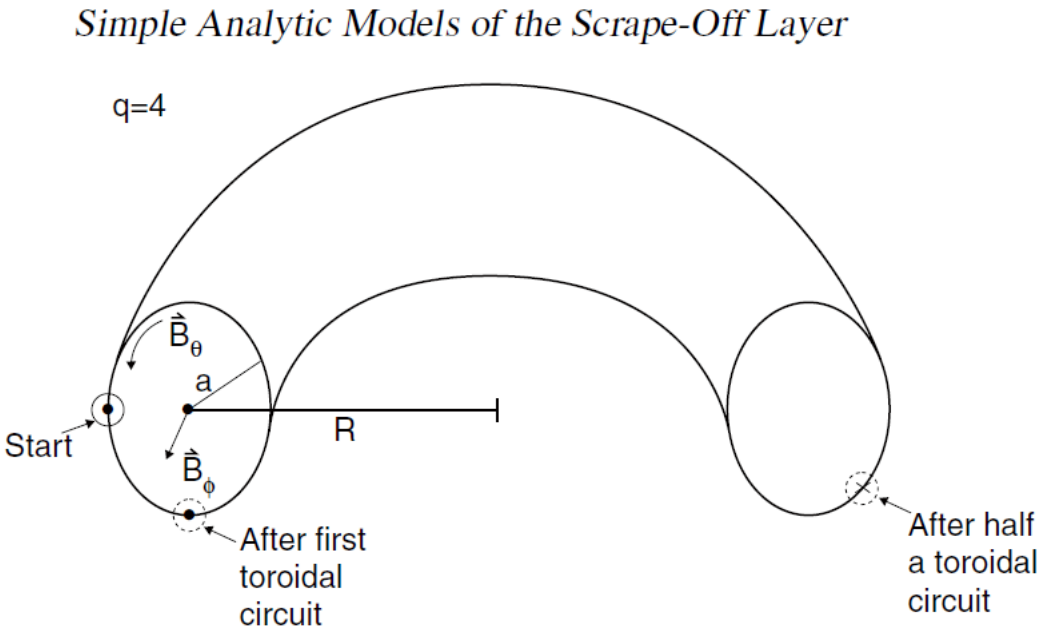

Fig. 1.5: Schematic illustration of a circular cross section plasma surface with q=4 [7].

1.3.3 H-mode

If sufficient plasma heating is provided, the increase of electron temperature causes a creation of a transport barrier at the plasma edge. This barrier is referred to as *outer transport barrier* (OTB). It is still unclear, what mechanism is responsible for the creation. One model proposes it is due to a suppression of turbulent transport by shear forces. The presence of the outer transport barrier results in higher confinement time, better confinement of particles and energy and overall better plasma performance. The tokamak regime utilizing this mechanism is called H-mode. H-mode has been experimentally discovered at ASDEX tokamak in 1982. Unfortunately, the better confinement is accompanied by higher thermal loads on the tokamak wall mainly due to the Edge localized modes (see Section 1.6.1). [7, 3, 8]

1.4 Scrape-Off layer

The plasma inside a tokamak can be divided into two sections. So called core plasma and edge plasma. Core plasma is located inside the last closed flux surface (LCFS,separatrix), The last magnetic flux surface not connected to the vacuum vessel. Edge plasma is located outside the LCFS. The area between LCFS and the vessel wall is called the *Scrape-Off Layer*. Because of

the open field lines, convection is the dominant transport mechanism in SOL, as opposed to core plasma, where diffusion is the main transport mechanism. As most of the heat from the plasma (apart from radiation) is deposited on the vessel wall at the place where magnetic lines touch the vessel, an intended component with high heat resilience must be installed to absorb the heat loads. Two approaches are used in current tokamaks, limiter and divertor [5, 7]

1.4.1 Limiter

Limiter is a component located inside the vacuum vessel, to which the magnetic field lines are connected to (It "limits" the plasma). In tokamaks either a poloidal or a toroidal limiter can be installed. The advantage of a limiter is its easy construction and therefore lower price. The problem is that the LCFS is defined by the component making core plasma connected to the limiter. In this case, release of impurities into core plasma can be very prevalent. As the limiter needs to be constructed from resilient materials (further discussed in Section 1.9) which are usually highly disruptive in a plasma (both by fusion reaction decrease and radiative cooling of the plasma) limiters are currently used mainly as a local backup protection for important in-vessel components, such as diagnostics, antennas etc. and during discharge start-up and run-down phases [7]

1.4.2 Divertor

With the goal to move the LCFS further away from the point where field lines connect to the vessel wall, the divertor configuration has been created. The idea is to create a X-point in the magnetic flux lines by specific (divertor coils), running electric current in the same direction as the plasma current outside the plasma. The resulting configuration (in Fig 1.6) is better at keeping impurities from entering core plasma and fuel recycling. The divertor area is also where pumping occurs, further increasing the positive effects. The downside however is higher complexity of the vessel design and construction price. [7]

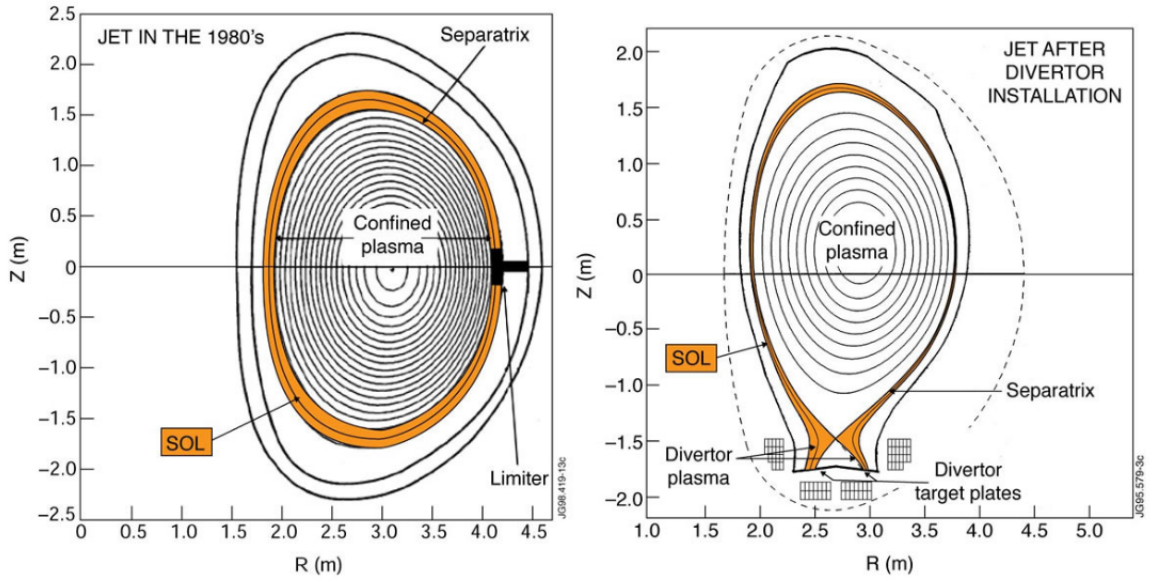

Fig. 1.6: Poloidal cross-section of the JET tokamak magnetic surfaces configurations in a limited plasma (left) and after divertor installation (right) [9].

1.5 SOL physics

1.5.1 Connection length

For a perfectly circular shaped limiter plasma limited by a **poloidal** limiters placed at n toroidal locations in the vessel, the typical distance a particle traverses inside the SOL along the magnetic field before reaching the limiter can be calculated as

$$L \approx \frac{\pi R}{n}, \tag{1.8}$$

where R is the major radius of the torus. This distance is called *connection length*. The distance between two points of contact with the surface along the magnetic field lines is easily derived as 2L.
For a **toroidal** limiter i.e., a toroidally symmetric rail along the whole vessel the connection length can be calculated as

$$L \approx \pi R q. \tag{1.9}$$

The larger value of L is caused by a small pitch angle between the field lines and the surface ($B_t >> B_p$). Typical values for current tokamaks are in the order of units and tens of meters, ($\approx$ 40 m for JET).

Calculation of the connection length for **divertor** plasma can be difficult, because the safety factor q is not constant radially in the SOL and reaches infinity close to the separatrix. The line infinity at separatrix and the very long values close to it are however neglected by both cross-field transport and field errors. For configurations with short divertor legs (poloidal distance from the x-point to the surface), the average connection length is the same as for the toroidal limiter case and therefore calculated with Eq. 1.9 [7]. When analyzing plasma behavior in the SOL in the simplest approach, neo-classical effects, that are normally present in tokamak plasma, can be neglected due to the high collisionality in the SOL, a characterization of a cold plasma. The SOL can be effectively "straightened". The resulting model (1D or 2D) of particle transport is driven by slow cross-field transport into SOL followed by rapid transport along the magnetic field to the surface. The diagram of this approximation is shown in Fig 1.7.

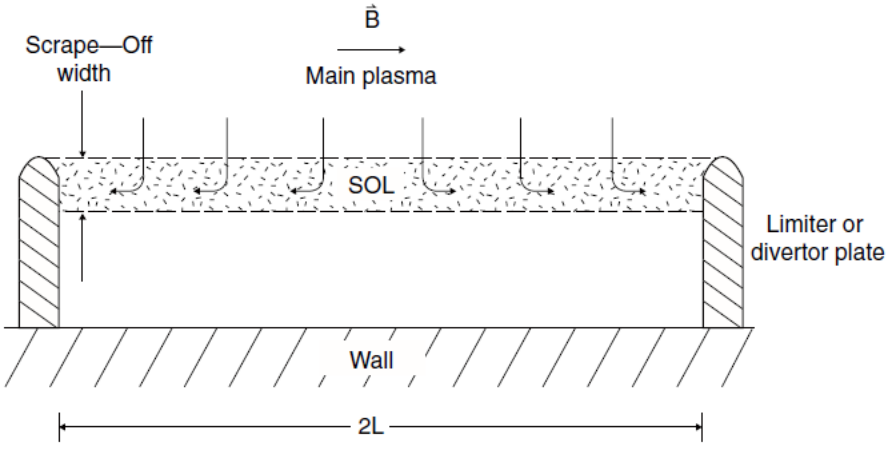

Fig. 1.7: Diagram of the simple SOL model with marked particle transport [7].

The high ratio of $v_{\parallel}$ and $v_{\perp}$ makes the width of the SOL only about 1 cm. The SOL region is further divided into *near SOL* and *main SOL* regions (Fig. 1.8).

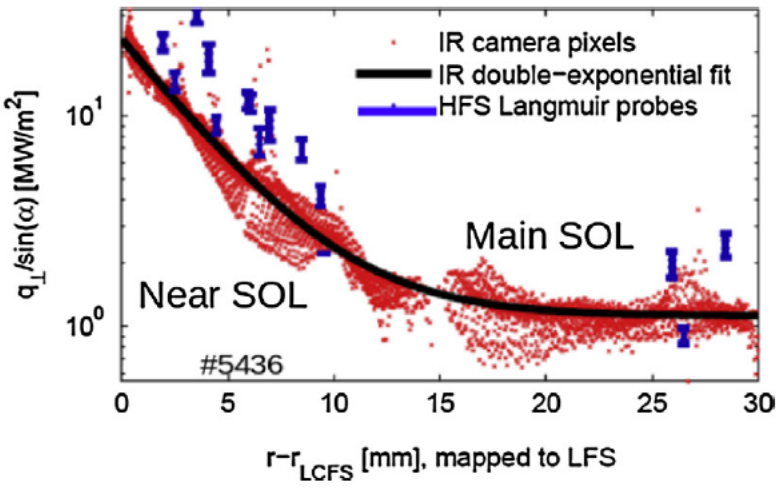

Fig. 1.8: The SOL $q_{\parallel}$ profile measured by Langmuir probes (blue) and IR camera (red) and the two-exponential fit (1.10)(black). Courtesy of [10].

The widths of the two regions can be derived from heat flux fitting by the following two exponential decay equation

$$q_{\parallel} = q_{\parallel,0}^{\text{main}} \left[\exp\left(-r/\lambda_{\text{q}}^{\text{near}}\right) + R_q^{-1} \exp\left(-r/\lambda_{\text{q}}^{\text{main}}\right) \right], \tag{1.10}$$

where $\lambda_{\text{q}}^{\text{near}}$ and $\lambda_{\text{q}}^{\text{main}}$ are the near and main SOL widths, $q_{\parallel,0}^{\text{main}}$ is the heat flux extrapolated to r_{LCFS} assuming only main SOL and R_q is the ratio of $q_{\parallel,0}^{\text{near}}$ and $q_{\parallel,0}^{\text{main}}$ at $r = r_{\text{LCFS}}$.

1.5.2 Simple divertor two-point model

In order to calculate the plasma temperature and density the so called *Two-point model* can be used. The two point model calculates these parameters at two points in the SOL *upstream*, where the plasma crosses separatrix (half-way between divertor targets or at mid-plane) and the target or *downstream* (Fig. 1.9). The name of the model is derived from the fact, that it is not concerned with the values of the temperature and density in between these two points.

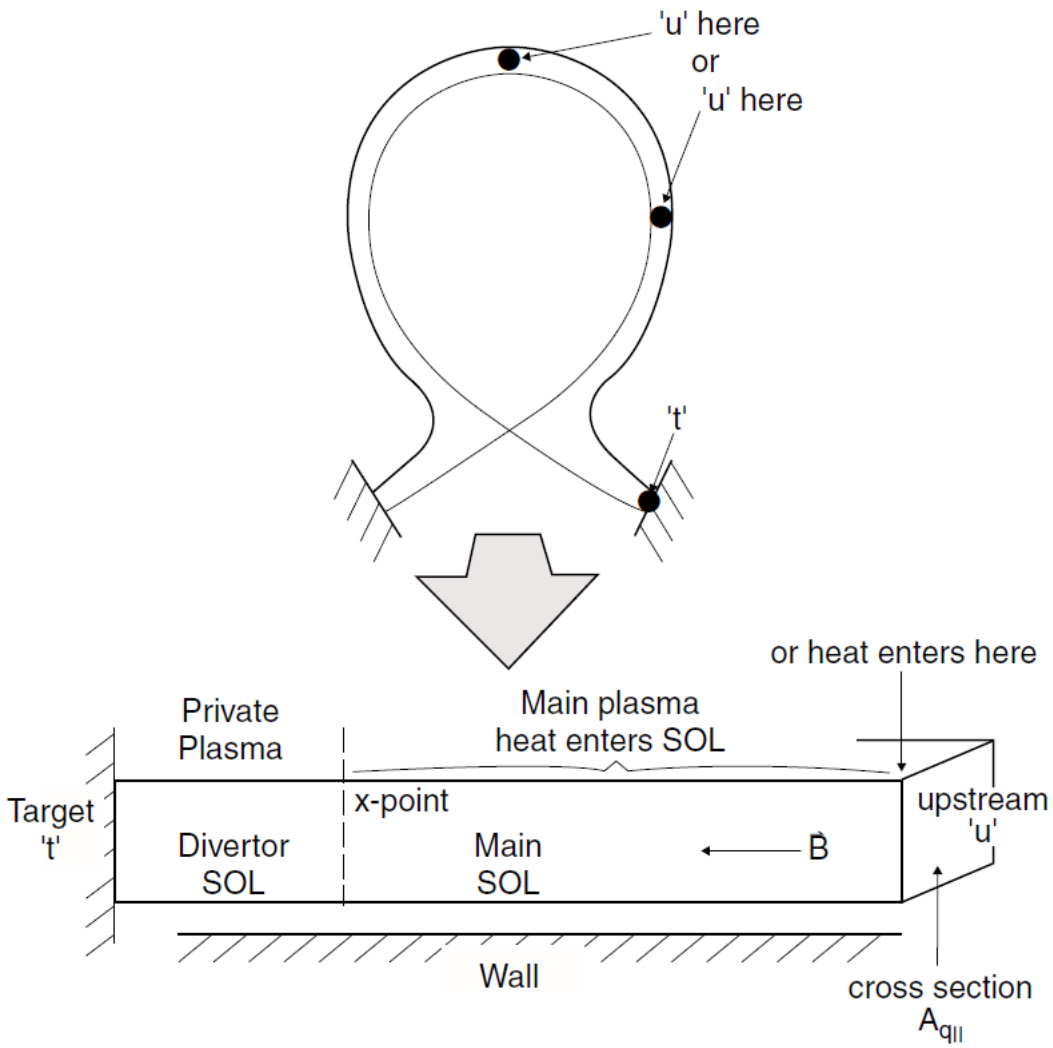

Fig. 1.9: Diagram of the points in the Two-point model and the "straighten out" SOL. Courtesy of [7].

The simple two-point model consists of the following assumptions and equations:

1. **Particle balance** - It is assumed, that all recycled neutrals are ionized in a thin layer above the target surface. The neutrals resulting from an ion, traveling along a particular field line, colliding with the target wall are re-ionized on the same field line. Each magnetic field line is therefore in its own localized particle balance. This means, there is no crossline transport of particles i.e., the balance is one dimensional. There is no parallel flow outside the ionization region. In the ionization region the flow speed increases from zero to a certain speed taken as the sound speed $c_{\mathrm{sd}} = (2k_{\mathrm{B}}T_{\mathrm{d}}/m_{\mathrm{i}})^{1/2}$.

2. **Pressure balance** - No friction and no viscous effects in the ionization region are assumed. The resulting pressure balance is

$$p + nmv^2 = const. \tag{1.11}$$

The dynamic part of the pressure $p_{\mathrm{dyn}} = nmv^2$ outside the ionization region is equal to zero as there is no parallel flow. The flow velocity at the target, taken as sound speed is $v_{\mathrm{d}} = c_{\mathrm{s}} = (2k_{\mathrm{B}}T_{\mathrm{i}}/m_{\mathrm{i}})^{1/2}$. If equal ion and electron temperatures $T_{\mathrm{e}} = T_{\mathrm{i}}$ are further assumed,

the resulting static pressure (for a hydrogen plasma) will be $p_{\mathrm{stat}} = nk_{\mathrm{B}}T_{\mathrm{e}} + nk_{\mathrm{B}}T_{\mathrm{i}} = 2nk_{\mathrm{B}}T_{\mathrm{e}}$ giving the total pressure balance between the upstream and downstream as

$$\begin{aligned} n(2k_{\mathrm{B}}T_{\mathrm{d}} + mv_{\mathrm{d}}^2) &= 2n_{\mathrm{u}}k_{\mathrm{B}}T_{\mathrm{u}}, \\ 2n_{\mathrm{d}}T_{\mathrm{d}} &= n_{\mathrm{u}}T_{\mathrm{u}}. \end{aligned} \tag{1.12}$$

3. **Power balance** - Because the flow velocity is equal to zero almost everywhere except the thin ionization zone, heat is transferred from upstream to downstream by heat conduction. If the assumption of only parallel heat flux $q_{\parallel}$ that all enters SOL at upstream and is removed at the target at the distance L is considered, the power balance is

$$T_{\mathrm{u}}^{7/2} = T_{\mathrm{d}}^{7/2} + \frac{7}{2}q_{\parallel}\frac{L}{\kappa_{0\mathrm{e}}}, \tag{1.13}$$

where $\kappa_{0\mathrm{e}}$ is the electron parallel conductivity. It is further assumed, that electrons and ions are thermally coupled, and the ion heat conductivity is negligible in comparison to the electrons. There is a temperature variation in the ionization zone, but since it is assumed to be thin, T_{d} is taken as equal to the temperature at the sheath edge. The last equation in the two-point model is the relation for parallel heat flux at the target

$$q_{\parallel} = \gamma n_{\mathrm{d}}k_{\mathrm{B}}T_{\mathrm{d}}c_{\mathrm{sd}}, \tag{1.14}$$

where γ is the sheath heat transmission coefficient. In summary the two point model gives a set of three equations for three unknown variables (usually either $q_{\parallel}, T_{\mathrm{d}}$ and n_{d} or $q_{\parallel}, T_{\mathrm{u}}$ and n_{u}) [7]

$$\begin{aligned} 2n_{\mathrm{d}}T_{\mathrm{d}} &= n_{\mathrm{u}}T_{\mathrm{u}}, \\ T_{\mathrm{u}}^{7/2} &= T_{\mathrm{d}}^{7/2} + \frac{7}{2}q_{\parallel}\frac{L}{\kappa_{0\mathrm{e}}}, \\ q_{\parallel} &= \gamma n_{\mathrm{d}}k_{\mathrm{B}}T_{\mathrm{d}}c_{\mathrm{sd}}. \end{aligned} \tag{1.15}$$

1.5.3 Edge plasma operation regimes

In standard tokamak operation, several regimes of SOL operation are recognized. These regimes differ in temperature and density gradients, radiative cooling, collisionality and other parameters. Theoretically all of the listed regimes could be achieved in both limiter and divertor tokamaks, however since the biggest differences between the regimes occur at the target, it is much easier to achieve some of them in divertor tokamaks. The broadest differentiation of the SOL operation regimes is:

1. **Sheath-limited regime (Low-recycling)**
   This is the most basic regime of SOL operation. The sheath-limited regime is characterized by very low temperature gradients along the SOL field lines (the plasma is iso-thermal in most of the SOL). This regime is sometimes referred to as *Low recycling*, due to low fuel recycling. In this regime the plasma-wall interaction and the parameters in the vicinity of the target are given by the plasma sheath. The plasma sheath is a region where the electric potential drops rapidly, as electrons which have much larger velocity than ions (due to low mass), arrive to the wall faster, thus breaking the ambipolar diffusion. The created electric field attracts ions and repels electrons. The attractive force can accelerate ions to $\approx 3T_{\mathrm{e}}$. Since in the sheath-limited regime the electron temperature can be very high (for COMPASS tokamak

typically tens of electron-volts [11]), the resulting ion temperature, or rather kinetic energy, causes strong sputtering of the wall material. This effect can be problematic especially in tokamaks with high heat and particle loads. As such, this regime is considered undesirable for utilization in potential power plants [7, 1].

2. **Conduction-limited regime (High recycling)**
   This regime is characterized by significant drop of T_e along the SOL flux tubes, due to the finite value of heat conductivity. In opposition to the sheath-limited regime, most of the parallel heat flux is transferred through the SOL via heat conduction rather than by heat convection. The finite heat conductivity then causes the large temperature gradients. To cause the conduction to overtake the convection large collisionality has to be present. This can generally be achieved by an increase in the electron density n_e. The increased density also causes larger recycling of the fuel and subsequent source of the impacting ions to be shifted from the upstream closer to the target. As a result, the sputtering and general erosion of the target are lower. It has to be noted, that the total heat load deposited on the target is the same as in the sheath limited regime (because the radiation losses are comparable). The main advantage of the conduction-limited regime is the lower impact energy of the ions. The so called *high-recycling regime* can be distinguished. The conduction-limited regime is accompanied by higher recycling than the sheath-limited regime, however in the high-recycling regime the dependency of recycling on the density goes from linear towards quadratic, thus further increasing it [7, 1].

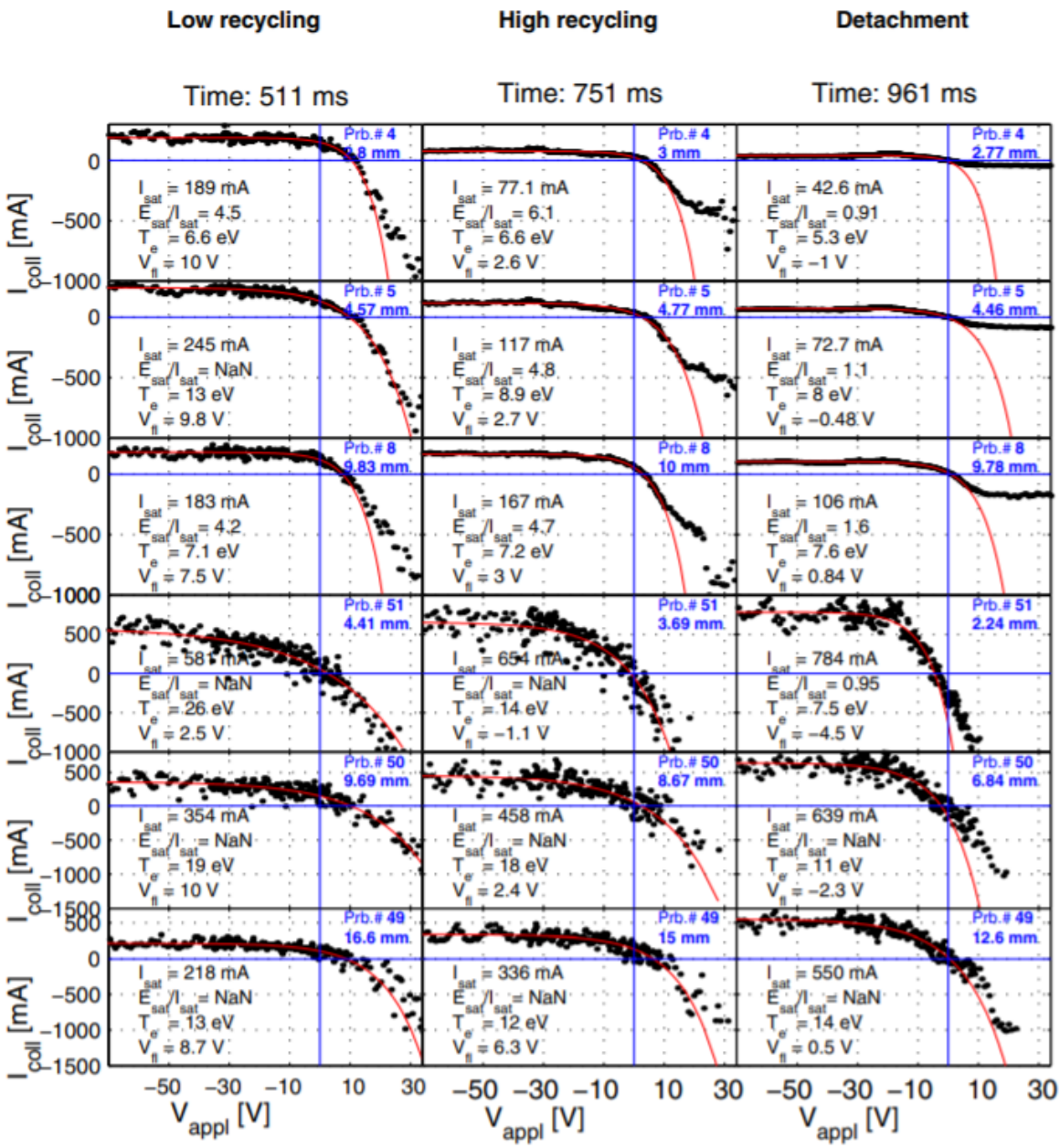

Fig. 1.10: Comparison of low-recycling, high-recycling and detached regimes in TCV tokamak Langmuir probes I-V characteristics. Courtesy of [12].

3. **Detached regime**
   If the temperature drops below few electron-volts, for example as a result of further increase in plasma density and recycling or by impurity seeding, a layer of neutral gas forms in front of the target. The plasma is therefore effectively striped from the target and attached to the neutral gas instead. The total power deposited to the target (or rather the cloud) is still the same as in the case of regimes 1) and 2), but the interaction of the electrons from the plasma with the neutral gas causes strong radiation power loss. This means that a potentially significant amount of power can be deposited homogeneously on a large area of the vessel wall, rather than a small area (especially in divertor plasmas). The decrease in power loads

to the target due to strong radiation is very beneficial in its protection. For this reason, the detached regime is highly desirable as an operation regime for tokamaks with high heat loads and potential power plants. The disadvantage of the detached regime, that bears a risk for the operation is the propagation of the neutral gas towards and across separatrix into the confined plasma. If the neutral gas crosses separatrix fuel dilution and radiation disruptions can occur. To counter this risk the so called *partial detachment* regime is targeted in operation, where the positive effect of detachment is maximized while the risk of neutral gas separatrix crossing is kept within an acceptable limit [7, 1, 13, 14].

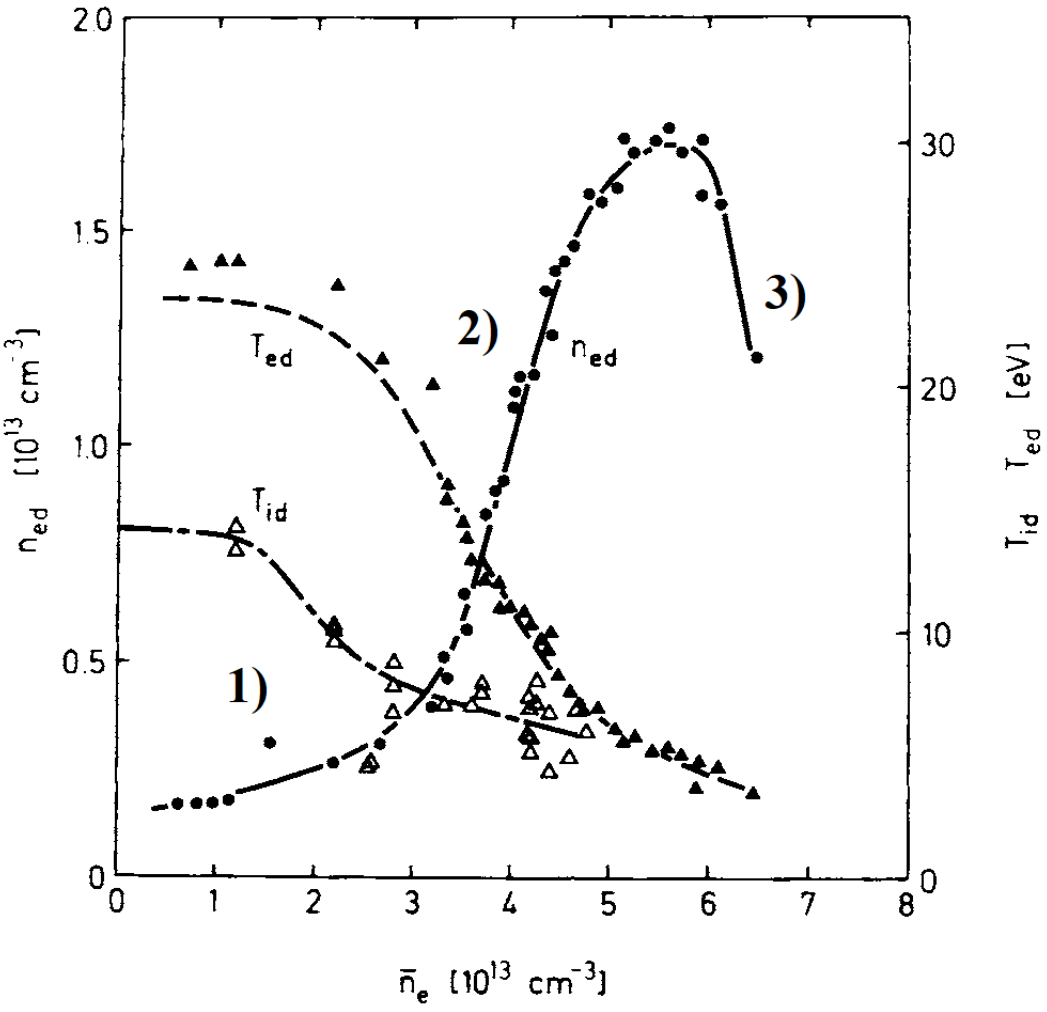

Fig. 1.11: Divertor density $n_{e,d}$, electron temperature $T_{e,d}$ and ion temperature $T_{i,d}$ dependence on line-averaged density $\bar{n}_e$, measured by Langmuir probes on ASDEX tokamak. Ion temperature is derived from Doppler-broadened CIII radiation. Adopted and edited from [7].

1.6 Transient heat events

Apart from steady state heat flux, transient heat events must be considered, when designing plasma facing components and their cooling. Even though they are short in duration, these events can create high enough heat loads and thermal shocks, to irreversibly damage PFCs. In tokamaks with divertor configuration these include ELMs, VDE, and disruptions, each with specific duration

and heat load. This problem is more apparent in larger devices especially with generation of fusion power, such as ITER or DEMO.
For example, the DEMO heat shock during an unmitigated disruption can exceed 100 MJ $m^{-2}s^{-1/2}$, critically damaging the heat shield [15].

1.6.1 Edge Localized Modes

Edge localized modes are periodic magneto-hydrodynamic instabilities occurring in tokamak plasma in H-mode operation regime. This regime occurs when total heating power exceeds a threshold value. Edge transport barrier, which is present in H-modes, results in accumulation of energy in confined plasma, which is then periodically released into SOL resulting in characteristic spiking in measured quantities (H_α radiation, heat flux, density, and others).

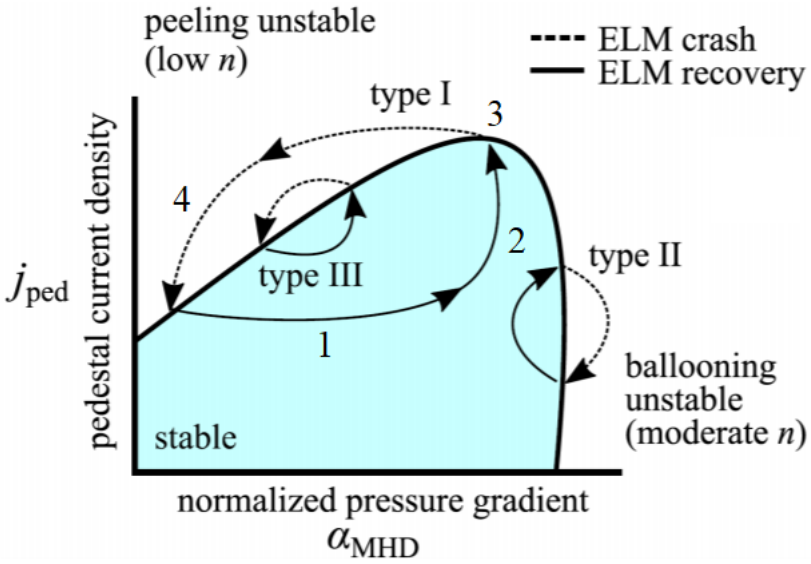

Fig. 1.12: Diagram of the ELM cycle in the peeling ballooning graph of tokamak edge stability. Adapted from [16].

When the edge transport barrier is created due to L-H transition, a steep pressure gradient (pedestal) forms. With further heating, the pressure gradient increases to the ballooning limit (Section 1 in Fig. 1.12). Current density (Sec. 2 in Fig. 1.12), generated by the bootstrap mechanism shifts the edge plasma parameters to the upper right corner of the stability boundary (Sec. 3 in Fig. 1.12), resulting in ELM crash (Sec. 4 in Fig. 1.12). The cycle is then repeated [5].

There are three types of ELMs distinguished by dependence of repetition frequency ν_{elm} and power crossing the separatrix P_{sep}. This dependence is used to for identification of Type I and Type III ELMs for $\frac{d\nu_{\mathrm{elm}}}{P_{\mathrm{sep}}} > 0$ and $\frac{d\nu_{\mathrm{elm}}}{P_{\mathrm{sep}}} < 0$ respectively. In case of Type II ELMs, no apparent dependence of ν_{elm} and P_{sep} is observed. Type II ELMs are usually present in strongly shaped plasmas. Type III ELMs typically occur close to L-H transition threshold. In current devices the ELM crash time $\tau_{\mathrm{elm}} = \frac{c_{\mathrm{i}}(T_{\mathrm{ped}})}{L_{\parallel}}$ is in range of hundreds of microseconds to few milliseconds [5].

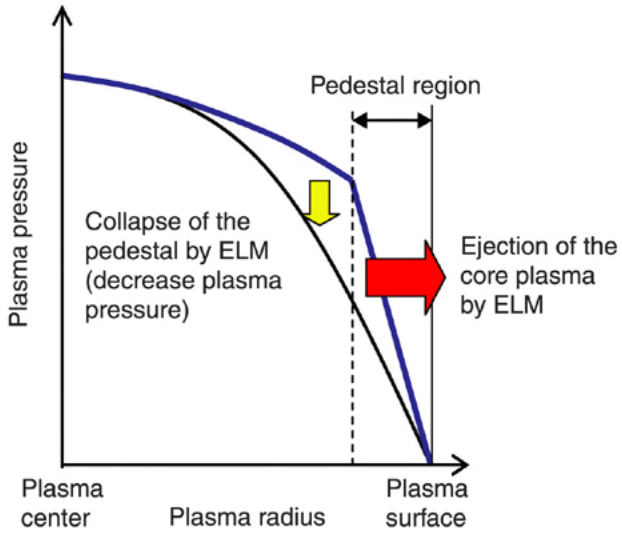

Fig. 1.13: Diagram of ELM pedestal collapse and subsequent pressure relaxation. Courtesy of [17].

The predicted heat shocks of ITER ELMs are 66 $\mathrm{MJm^{-2}s^{-1/2}}$ [15]. This is enough to locally melt the tungsten monoblock plasma facing units. Mitigation, suppression, or other form of lowering the heat shock of the ELMs or new divertor design is therefore required [15, 18].

ELM energy fluence scaling

Energy fluence $\varepsilon_{\parallel}$, the main parameter for ELMs, can be empirically scaled from other devices, similarly to other parameters in tokamak physics. Empirical scaling law derived in [19] uses the pedestal electron density $n_{\mathrm{e,ped}}$ in $[10^{20}\ \mathrm{m^{-3}}]$, pedestal electron temperature $T_{\mathrm{e,ped}}$ in [keV], relative ELM size ΔE_{ELM} in [%] and major radius R in [m]. The derived scaling formula is

$$\varepsilon_{\parallel} = 0.28 \pm 0.14 \frac{\mathrm{MJ}}{\mathrm{m^2}} \times n_{\mathrm{e,ped}}^{0.75\pm0.15} \times T_{\mathrm{e,ped}}^{0.98\pm0.1} \times \Delta E_{\mathrm{ELM}}^{0.52\pm0.16} \times R^{1\pm0.4}. \tag{1.16}$$

The data set used for the scaling law fit are in Fig. 1.14. The scattering of the data account for a margin of 3 for the scaling law.

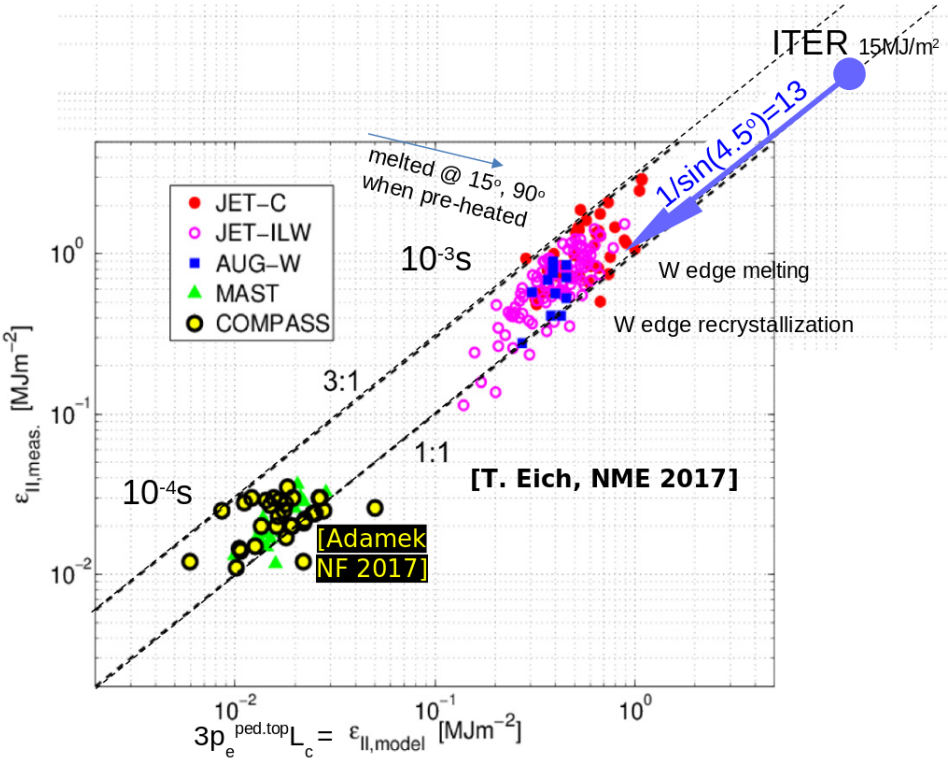

Fig. 1.14: ELM energy fluence in various devices with the empirical scaling law derived in [19] versus experimental data from [11, 19]. Courtesy of [20].

1.7 Magneto-hydrodynamic instabilities

Description of plasma as a single fluid model is done via magneto-hydrodynamics. Plasma is there for simplicity taken as one fluid and its behavior is calculated through the Maxwell's equations and the Navier-Stokes equation. This approximation is accurate in plasmas with high collisionality and with Maxwell-Boltzmann velocity distribution or a distribution close to it. Maxwell's equations are

$$\nabla \cdot \mathbf{D} = \rho_q, \tag{1.17a}$$

$$\nabla \cdot \mathbf{B} = 0, \tag{1.17b}$$

$$\nabla \times \mathbf{E} = -\frac{\partial \mathbf{B}}{\partial t}, \tag{1.17c}$$

$$\nabla \times \mathbf{H} = \mathbf{j} + \frac{\partial \mathbf{D}}{\partial t}, \tag{1.17d}$$

where $\mathbf{D}$ is electric induction, $\mathbf{B}$ is magnetic flux density, $\mathbf{E}$ is electric field intensity, $\mathbf{H}$ is magnetic field intensity, ρ_q is charge density and $\mathbf{j}$ is electric current density. And the Navier-Stokes equation (including the Lorentz force density) is

$$\rho \frac{\partial \mathbf{u}}{\partial t} + \rho(\mathbf{u} \cdot \nabla)\mathbf{u} = -\nabla p + \eta \nabla^2 \mathbf{u} + (\zeta + \frac{\eta}{3})\nabla(\mathrm{div}\mathbf{u}) + \mathbf{j} \times \mathbf{B}, \tag{1.18}$$

where $\mathbf{u}$ is flow velocity, ρ is density, p is pressure, η and ζ are first and second viscosities [1].

1.7.1 Rayleigh-Taylor Instability

Rayleigh-Taylor instability [1, 21] develops at an interface of two fluids, where the density gradient has an opposite direction to an acting force (for example a denser fluid above a thinner fluid in gravity field). For a plane interface the dispersion relation is

$$\omega^2(\rho_a + \rho_b) - \frac{1}{\mu_0}\left[(\mathbf{k}\cdot\mathbf{B}_a)^2 + (\mathbf{k}\cdot\mathbf{B}_b)^2\right] + gk(\rho_a - \rho_b) = 0, \tag{1.19}$$

where μ_0 is vacuum permeability, g is gravitational acceleration, $\rho_{a,b}$ are densities, $\mathbf{B}_{a,b}$ are magnetic fields and $\mathbf{u}_{a,b}$ are the speeds of the respective fluids. $\mathbf{k}$ is the wave number and ω is the frequency of the instability.

1.7.2 Kelvin-Helmholtz Instability

Kelvin-Helmholtz instability [1, 21] generally occurs at an interface of two fluids with a speed difference or in a continuous fluid with a sheer velocity gradient. The general dispersion relation for a plane interface is

$$(\omega - \mathbf{k}\cdot\mathbf{u}_a)^2\rho_a + (\omega - \mathbf{k}\cdot\mathbf{u}_b)^2\rho_b - \frac{1}{\mu_0}\left[(\mathbf{k}\cdot\mathbf{B}_a)^2 + (\mathbf{k}\cdot\mathbf{B}_a)^2\right] + gk(\rho_b - \rho_a) = 0. \tag{1.20}$$

1.8 Thermal effects in Plasma-Wall interaction

Effects of plasma-wall interaction caused by individual particles are discussed in Section 2.1. Based on the plasma MHD properties (density, temperature, flow speed etc.) quantities important for the thermal interaction with the wall can be derived. The most important quantity in this relation is the heat flux, the amount of heat transferred across a surface per unit of time. In tokamak physics, parallel heat flux $q_\parallel$ and perpendicular heat flux $q_\perp$ are utilized. The difference between these two is caused by the angle α between the surface and the plasma flow (magnetic field lines vector). Thus, a relation

$$q_\perp = \sin(\alpha) q_\parallel. \tag{1.21}$$

Steady state heat flux does not fully reflect the effect of an event on the surface (typically in case of transient events). Thermal pulse quantity is therefore used to quantify the thermal effect of a rapid event where the heat penetration depth d_p is shorter than the thickness of the heated material d_t ($d_p << d_t$). It is the depth to which the heated body initial temperature T_0 was significantly changed by the heating pulse applied to one end.

$$d_p = \sqrt{\frac{t\kappa}{c_\mathrm{v}}}, \tag{1.22}$$

where t is the pulse duration, κ is the heat conductivity of the material and c_v is its volumetric heat capacity ($\approx \frac{1\ \mathrm{cm}}{\sqrt{s}}$ for tungsten). In case of tokamak plasma-wall interaction, the surface (or close to it) temperature T_surf is the most important. κ varies significantly for different materials and for the most of them $c_\mathrm{v} = 3 \pm 0.5\ \mathrm{Jcm^{-3}K^{-1}}$ [20]. Thermal pulses can rapidly heat up the surface to the point of permanent damage (melting, recrystallization etc.), while the rest of the body stays at safe temperatures. The relative surface temperature increase during such events can be calculated as

$$\Delta T = 2q\sqrt{\frac{t}{\kappa c_\mathrm{v}\pi}}. \tag{1.23}$$

In total, the surface temperature of the heated wall is

$$T_{\text{surf}} = T_{\text{cool}} + q_{\perp}^{\text{steady}} \frac{d}{\kappa} + \Delta T. \tag{1.24}$$

The first addition member is the temperature of the active coolant (if present), the second, where d is the depth of the cooling pipe, is steady state heating and the last is the change due to rapid heat pulses. Note that the first and the second members are steady state, but the last one is pulsed (relative to long heating) [15, 22, 20].

1.9 Plasma facing components

Historically the first materials with direct contact with the plasma (plasma facing components) were the vacuum chamber wall materials themselves, such as glass or steel. With the ever-progressing development of the fusion plasma technologies, the increase in the contained energy inside the plasma brought increased heat loads requiring specified heat shields to be installed. Plasma facing components are subjected to high energy particle fluxes, high heat fluxes, high electrical currents and other phenomena that can be potentially dangerous and destructive to them. The most apparent material to serve as a plasma facing component is graphite. It is a broadly used material for heat shields in numerous applications, such as Space Shuttle heat shields [23]. Subsequent research has however shown that graphite is not an ideal material to serve as a plasma facing component in a fusion reactor, because of undesirable tritium fuel retention in the graphite, where it chemically bonds and creates volatile compounds (e.g. methane) and release of sputtered carbon dust into the plasma. For this reason, an extensive development of advanced materials capable of withstanding the extreme conditions inside a fusion reactor is currently undergone [24, 25]. In case of tokamaks, plasma facing components are the first wall, limiters and the divertor.

1.9.1 ITER First Wall

The first wall is essentially a limiter but not with the task to serve as a primary heat shield. Rather it serves as a protection for the vacuum vessel. In future fusion reactors, where tritium production from fusion neutrons will be crucial (DEMO and subsequent power plants) the first wall will be directly connected to the blanket, to minimize neutron losses in the first wall. The ITER first wall will be constructed from beryllium covered panels (Fig. 1.15). The usage of beryllium for the first wall is the low Z=4 requirement, due to the proximity of separatrix and potential release of the material into the core plasma, and subsequent cooling of the plasma core (Fig. 1.21).

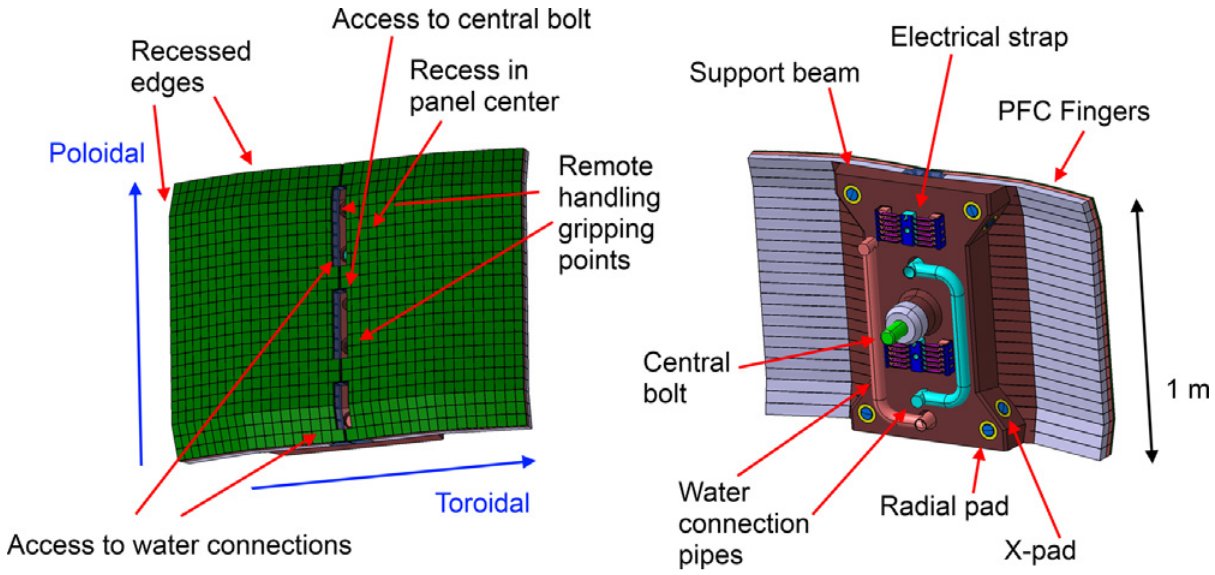

Fig. 1.15: Design of the ITER first wall panel (Blanket Module 1). Courtesy of [26].

The *Enhanced heat flux* FW design utilizing CuCrZr made heat sink with a hyper-vapotron based active cooling is capable of handling heat fluxes up to 4.7 MW/m^2. This is sufficient for ITER operation as the bulk of the total incoming heat flux from the plasma will be deposited on the divertor. The only situations when considerable heat load is deposited on the first wall is in the ramp up phase, before X-point formation (and ramp down phase), or transient events [26]. Experiments on COMPASS tokamak with IR camera observation of a specialized graphite tiles with various shapes at the center column to investigate narrow heat flux channels revealed, the narrow heat flux channels would prove problematic for heat load management at ITER limiters [10].

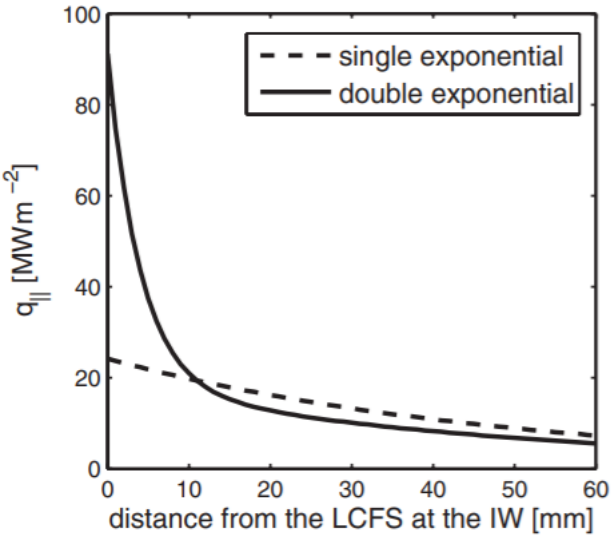

Fig. 1.16: ITER radial profiles of $q_{\parallel}$ obtained from equation (1.10) for $\lambda_{\mathrm{q,main}}^{\mathrm{design}} = 50$ mm and $R_{\mathrm{q}} = 0$ (single exponential) and $\lambda_{\mathrm{q,main}}^{\mathrm{design}} = 50$ mm $\lambda_{\mathrm{q,near}}^{\mathrm{design}} = 4$ mm and $R_{\mathrm{q}}^{\mathrm{design}} = 4$ (double exponential). $P_{\mathrm{SOL}} = 5$ MW in both cases. Courtesy of [27].

This was a crucial argument for the ITER limiter design update. The limiter shape has been optimized for $q_{||}$ prediction from Eq. (1.10) in Fig. 1.16. The resulting shape is in Fig. 1.17.

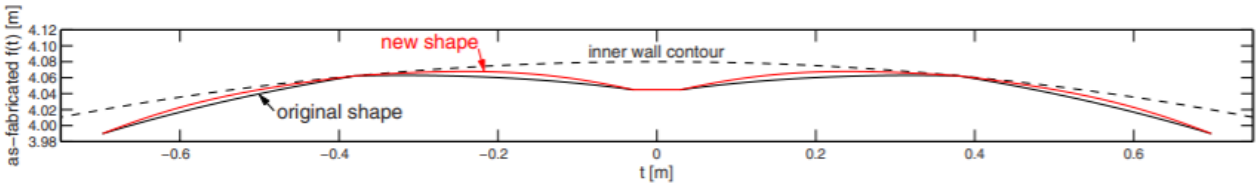

Fig. 1.17: Toroidal profile of the original and the new IW FWPs in ITER, optimized for the $q_{||}$ profiles in Fig. 1.16. Courtesy of [27].

The updated limiter shaping ensures the heat flux on the limiter will be kept below the $q_{||}^{\max} = 4.7$ MW/m^2 limit, i.e. mitigating the narrow channel effect on the heat flux, if it will be present, while only slightly increasing the peak heat flux if the narrow channel will not be present [27, 10, 26].

1.9.2 ITER Divertor

ITER divertor design is driven mainly by the heat fluxes from plasma. Since prolonged operation without extensive repairs is highly desirable, the divertor heat shield has to be carefully designed with regards to several variables. The first logical choice for the plasma facing material is graphite, as a broadly used material in tokamak plasma facing components, proven to withstand significant heat loads [28]. Graphite heat shields are however problematic for fusion devices operating with tritium, as the fuel retention by the graphite would exceed the acceptable limits [29, 30]. Other reason making graphite a nonviable option is sputtering and the resulting transport of carbon into core plasma. For these reasons, tungsten was chosen as the divertor plasma facing material. The resulting design is shown in Fig. 1.19. The concerning issue of this design is the possible cracking (at 20 MW/m^2), local melting and overall degradation of the tungsten plasma facing units. The dependence of the divertor life-time on the heat load presented in [24] and shown in Fig. 1.18 sets the acceptable recrystallization time of 2000 hours for steady state heat flux of 16 MW/m^2. If the heat flux was 20 MW/m^2, the recrystallization time would be less than a day.

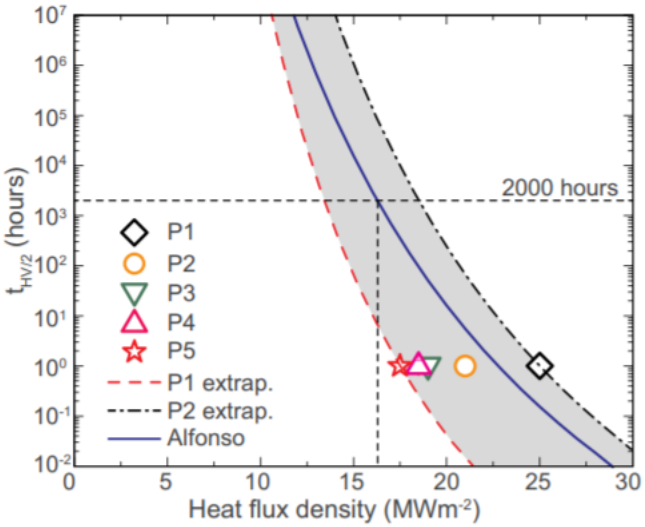

Fig. 1.18: Recrystallization time to a depth of 2 mm (using the time for material hardness to decrease by 50 % as a proxy) as a function of the surface heat flux density at the center of a 6 mm thick tungsten monoblock. Courtesy of [24].

This strictly given heat flux limit poses a considerable risk in ITER operation, as the peak heat flux predictions are still inconclusive. Empirical scalings of power decay length for ITER in [31] predict $\lambda_q \approx 1$ mm. Assuming the total SOL input power $P_{SOL} = 120$ MW (2/3 deposits on the outer target) and the area where the power is deposited $S = 2\pi f_x R_0 \lambda_q = 0.4$ m^2 give heat flux density of $q_\perp = 80$ MW/m^2 well over the given limit. With proper impurity seeding the radiation fraction f_{rad} can be increased to 85 % without significant influence on core plasma [32], decreasing the heat flux below the limit.
Other possibility is an increased power decay length due to strong turbulent behavior of the ITER plasma. If the recent simulations in turbulence models XGC1 in [33] and BOUT++ in [34] will be more closer to the reality, rather than the empirical scalings, the energy will be deposited on a 5-10 times larger area ($\lambda_q = 6$ mm due to stronger SOL turbulence caused by the larger ratio of minor radius and ion Larmor radius a/r_L^{ion}) , giving $5 < q_\perp$ [MW/m^2] < 16 [15, 30, 29, 18].

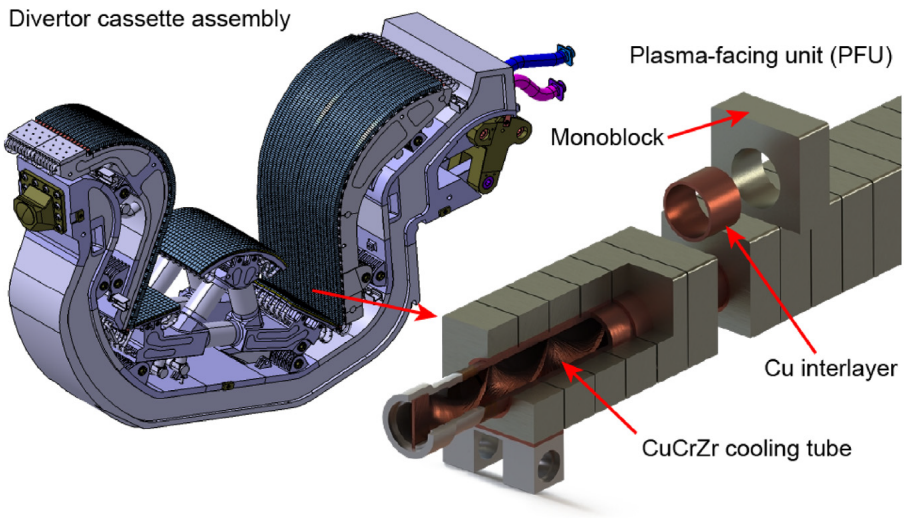

Fig. 1.19: ITER divertor cassette CAD model with the tungsten monoblock and CuCrZr cooling swirl tube pipes close up. Courtesy of [30].

Apart from steady state (inter-ELM) heat loads transient heat events also have to be considered in the ITER divertor design. Empirical scalings of ITER ELM energy in [19] (See Fig. 1.14) predict ITER ELM energy of $\varepsilon_{\parallel,} = 5$ MJ/m^2 for the $I_\mathrm{p} = 7.5$ MA scenario and $\varepsilon_{\parallel,}^{Q=10} = 15$ MJ/m^2 for the Q=10 regime [19, 11]. With the surface where the power is deposited of around 1 meter, these energies are equivalent to the explosion of more than a kilogram of TNT. As such they pose a serious hazard to the divertor (for example in the form of local flash melting of the monoblock surface) [19, 15].

The problem of the ELM heat loads must be solved in order to fulfill the predicted $Q = 10$ operation of the tokamak. If the ELM heat load is unmitigated, the threat of local flash melting of the tungsten monoblocks is imminent. The parallel ELM energy fluence on ITER is predicted to be $\varepsilon_\parallel = 15$ MJ/m^2 (Fig. 1.14). With the expected incidence angle of 4.5 degrees (3 degrees is the angle of incidence of the magnetic field lines and 1.5 degrees is the tile inclination to avoid exposure of misaligned tile edges) and the ELM decay time $t_\mathrm{ELM} = 0.5$ ms, the resulting perpendicular heat shock is $15 \times \sin(4.5°) \times \sqrt{(5 \times 10^{-4})} = 53$ MJm^{-2}s$^{-1/2}$ [15]. This is just below the tungsten flash melting point, but the margin for increase is narrow. Unlike the steady state heat flux, which is expected to be mitigated by impurity seeding, it is still unclear, whether the impurity seeding will provide sufficient protection against the ELMs, especially in high density regimes, with acceptable decrease of energy confinement [35, 36]. One option is a real time feedback control [14], however other options of wall protections, such as fast strike point sweeping [37], or liquid metal plasma facing components should also be investigated [25].

1.9.3 Other devices with high heat loads

If the proposed techniques of heat load control result in successful ITER operation even in the $Q = 10$ regime, the problem will not diminish, as these might not suffice for other future devices. The current DEMO design with fusion power of $P_\mathrm{f}^\mathrm{DEMO} = 2000$ MW and major radius of the vessel $R_\mathrm{DEMO} = 9$ m [38] will, with the same calculation as done for ITER in Section 1.9.2, result in $P_\mathrm{SOL}^\mathrm{DEMO} = 450$ MW and divertor perpendicular heat flux $q_\perp^\mathrm{DEMO} = 37$ MW/m^2. To accommodate the recrystallization limit of tungsten monoblocks in Fig. 1.18 with operation time before broad divertor repairs of at least 5000 hours ($q < 15$ MW/m^2) the radiation fraction would have to be at

least $f_{\text{rad}^{\text{DEMO}}} = 0.98$, something that has not yet been proven achievable. A possible solution is to increase radiation from the core; however the viability of this approach also has to be proven.

The goal of fusion energy design is to construct a fusion device with the highest fusion power and the smallest dimensions possible. One such endeavor, to construct a more compact device is the ARC/SPARC project. The SPARC tokamak, currently in the design stage is going to be the first of such devices. Increase in fusion power and decrease of the volume result in higher heat loads. The current predictions for SPARC in [39], predict unmitigated heat fluxes $q_{\perp} = 350$ MW/m^2 and ELM energy fluence comparable to ITER. This would require radiation fractions similar to those predicted for DEMO in this section.

1.9.4 Limits of active PFC cooling

Apart from a heat load limit set by the structural and physical properties of the PFC, discussed in the previous sections, the limit of the active cooling also has to be considered, in PFC designs. An actively cooled PFC can be kept at a steady surface temperature over long periods of time, however a not cooled one would overheat almost immediately. The active cooling power is of course limited by the properties of the coolant such as temperature, heat capacity, flow speed and the technology of the cooling system. The main constrictions giving the total cooling power are given from the engineering design (e.g. the input/output temperature difference of the coolant). Even with other power handling systems implemented, a robust active cooling system is also desirable, as it is the primary system of heat removal from the vessel.

The ITER divertor cooling system (See fig. 1.19) made from CuCrZr tubes inside the tungsten monoblocks implement swirling for better heat transfer. This system is expected to keep the monoblocks from cracking and other mechanical damaging at heat fluxes $q_{\text{peak}} \approx 16$ MW/m^2, for a timeline of 2000 hours, as discussed in Section 1.9.2. This might prove to be insufficient for devices with higher wall heat loads (See Section 1.9.3). The system potentially capable of increased heat removal, called hypervapotron. The hypervapotron has two main advantages over swirl tubes. Not only does it have a better potential of heat removal $\approx$ 25-30 MW/m^2 in ITER divertor [40], but also better heat distribution in the monoblock as the profile of the channel is rectangular and not circular (See Fig 1.20).

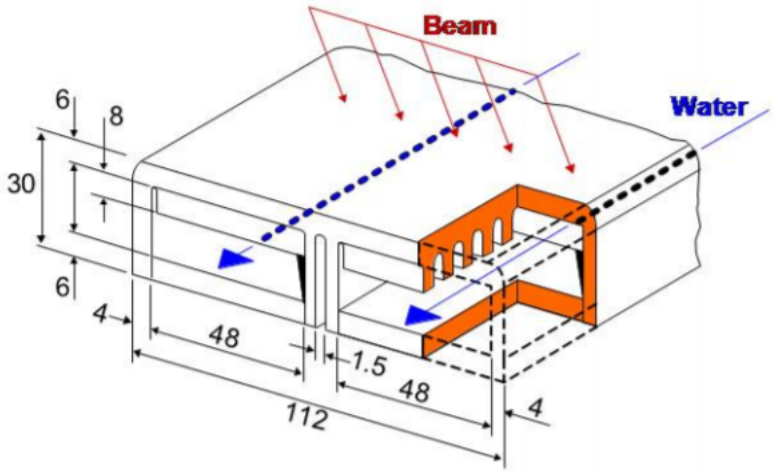

Fig. 1.20: Design of the JET NBI hypervapotron cooling channel. Courtesy of [41].

The reason for the better heat removal capabilities of the hypervapotron is the utilization of water boiling. The serrated profile of the tube (See Fig. 1.20), creates a turbulent flow further increasing the heat transfer. The amount of water vapor has to be kept below a given threshold, as the heat exchange would decrease above it. As the heat removal capabilities rely on the turbulent water/vapor flow, the simulations of this system are extremely demanding. Research presented in [42] indicates, that the heat removal potential of a hypervapotron can be even above 30 MW/m^2, however it has to be proven experimentally. Determination of the engineering limit of hypervapotron cooling should be highly prioritized, as heat removal is a crucial part of a fusion power plant design.

1.10 Radiation in tokamak plasma

Radiation in tokamak plasmas is an important field of study, with an impact on the plasma performance throughout the whole volume of the plasma. As the tokamak plasma is in a total thermal equilibrium (radiation transparency), the rate at which plasma radiates is crucial. This effect can be both beneficial and adverse. Strong radiation in SOL for example helps with distribution of the thermal load homogeneously over a larger area than the strike point. Excessive radiation from the core plasma and subsequent plasma cooling, where high temperature is a requirement, can substantially decrease the fusion reaction rate.

1.10.1 Radiation of atomic processes

In plasma interaction several radiation atomic processes occur. These can be divided into groups by the initial and resulting state of the interacting electron either free or in the electron cloud of an atom:

- bound-bound - line radiation
- free-bound - recombination

- free-free - bremsstrahlung, cyclotron

Collision events resulting in excitation, ionization or recombination can also be accompanied by photon emission. The resulting magnitude of these events and the radiated power depends mainly on density and temperature of the plasma. For low temperatures line radiation dominates. The radiated power in such conditions is calculated from evaluated equilibrium of states. The prevalence of each state with plasma density then determines the radiated power [43, 44].

1.10.2 Cyclotron radiation

When the velocity vector of an accelerated charged particle is changed, radiation with the cyclotron frequency $\omega_c = \frac{qB}{m}$ is radiated. In tokamak plasma the biggest source of cyclotron radiation is the gyro rotation of the electrons. The total radiated power by one electron through gyro rotation can be calculated as

$$P_c = C_c \left(\frac{e^2 B v_\perp}{m} \right)^2, \tag{1.25}$$

where C_c is a physical constant. For a typical tokamak plasma, the total radiated power would be orders of MW/m^3, meaning the plasma would immediately radiate all power. The tokamak plasma is however optically thick in the frequencies of the cyclotron radiation. Thus, the vast re-absorption makes the total losses negligible. Cyclotron radiation can however be utilized as an indicator of non-thermal particles. [45, 3, 46].

1.10.3 Bremsstrahlung

For clean fully ionized plasma line radiation power is negligible, since all atoms are fully striped from their electrons and the high plasma temperature prevents any recombination. Because of that bremsstrahlung overtakes the place of the most significant form of radiation. The radiated power density is

$$P_{\text{brem}} = C_b n_e^2 Z_{\text{eff}} T_e^{1/2}. \tag{1.26}$$

C_b is a physical constant, the electron density n_e is usually given by the fusion power requirement. The temperature T increase can drive up the radiation power, however it is also going to be kept (in core plasma) at a specific value for fusion power optimization. The only variable, that cannot be fully controlled is the effective charge Z_{eff}. The diffusion of impurities into the plasma can drastically increase bremsstrahlung (and total) radiated power. This applies for low Z impurities which are rapidly ionized. In case of Tungsten, a common high Z impurity, line radiation will be the dominant effect of the radiation power loss, as full ionization might not be achieved even in core plasma. This can be seen in Fig. 1.21, where even at very high temperatures tungsten radiation is not gradually increasing, as expected for bremsstrahlung radiation [47, 43].

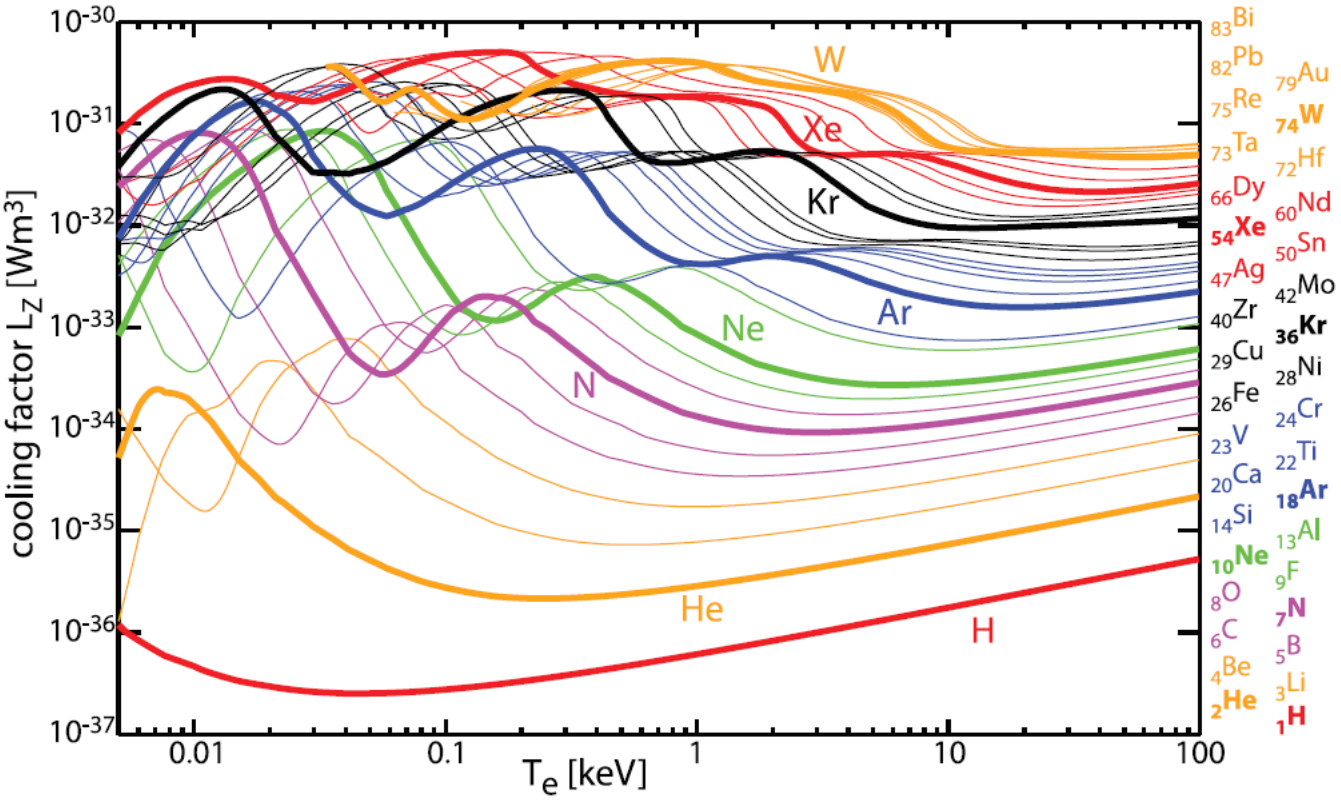

Fig. 1.21: Calculated cooling factors for elements from H to Bi (and their isotopes) at $n_e = 5 \times 10^{19}$ m^{-3}. Courtesy of [44].

2. Liquid metals as plasma facing materials

One of the potential solutions of the heat load problem can be a plasma facing component consisting of a liquid metal component. The term *liquid metal* can be broadly applied to any metallic compound in a liquid state of matter. In tokamak physics, this term is used for materials, that are in liquid state in the range of operational conditions of the device (i.e. high vacuum and temperatures in lower hundreds of degrees Celsius). Liquid metals, or alloys, can be used in tokamaks and tokamak-based power plants in a variety of applications. For example, as coolants or fuel breeding media. The advantage of a liquid plasma facing surface is the absence of a crystalline lattice. However, each of the potential materials suitable as a plasma facing material has its disadvantages, such as fuel retention or high evaporation rates in case of lithium or high proton number in case of tin. An obstacle all liquid metals share is fluidity. This property makes all efforts of designing PFCs based on liquid metals challenging. The various methods of dealing with this problem will be discussed further in this chapter.

2.1 Erosion by high energy ions

The bombardment by high energy ions of a solid, or liquid surface results in erosion of the material. The material is heated by the energy transmitted by the ions to the surface. Kinetic effects also affect the surface. This section focuses on the effects of the ion flux onto a liquid surface.

2.1.1 Sputtering

If a high energy ion strikes the liquid surface, the kinetics of this collision may result in a particle being ejected from the surface. This event is referred to as *sputtering*. If the energy of the incoming particle is high enough, a cascade of subsequent collisions may result in several displacements and potential ejections. Since it is highly dependent on the initial conditions of the collision it behaves stochastically in terms of the particle ejections. In calculations of the particle ejections per one striking ion an average value is taken (empirically measured).

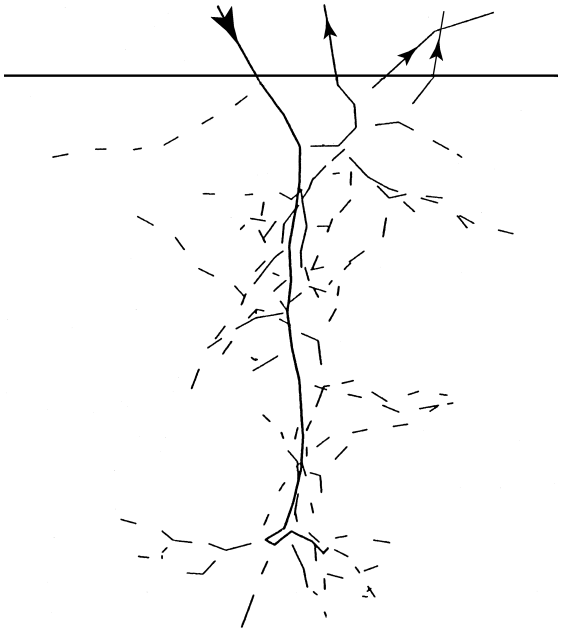

Fig. 2.1: Simulation in the TRIM.SP model of the collisional cascade caused by Ar ion with $E = 1$ keV colliding at Ni surface at an angle of 30°. Courtesy of [48].

The magnitude of the effects of physical sputtering is dependent on the mass of the interacting particles, the binding energy of the sputtered particles and the energy of the impacting ion. Other circumstances and conditions however affect the sputtering yield. The most important in case of liquid metal plasma facing components is the surface temperature. It has been empirically observed, that with rising temperature the effective yield increases [49, 50]. Models based on the formation of quasi-particles called adatoms, are the most successful in explanation of the increase. Chemical reactions resulting in formation of various compounds (CH_4, LiH, SnH_4 etc.) will also affect the yield. Other effects, such as self-sputtering, preferential sputtering (statistical preference of one element in sputtering of multi-element surfaces) and other phenomena alter the yield as well [48, 49].

2.1.2 Evaporation

Apart from the boiling state, in which liquid changes its state to gas in the whole volume, particles can be released from the liquid surface even at lower temperatures. This effect known as *evaporation* is the result of the Maxwellian distribution of velocities. Some particles may acquire energy sufficient enough to break out of the potential well of the liquid chemical bond. The resulting particle flux from or to the liquid is described by the Langmuir evaporation equation

$$\Gamma_{\mathrm{vap}}(T) = \frac{p_{\mathrm{v}}(T) - p_{\mathrm{p}}(T)}{\sqrt{2\pi m \mathrm{k_B} T}}. \tag{2.1}$$

The flux is essentially only a function of the surface temperature T. If a liquid surface is exposed to a closed box with total vacuum, the partial pressure p_{p} of the evaporating material above the surface is equal to zero. The evaporation flux is then driven only by the vapor pressure p_{v} of the liquid. As the gas fills the box, the partial pressure increases and the flux decreases until an equilibrium state, where the same number of particles is evaporated and deposited on the surface. If expansion to infinite vacuum is assumed, the flux is driven purely by the vapor pressure.

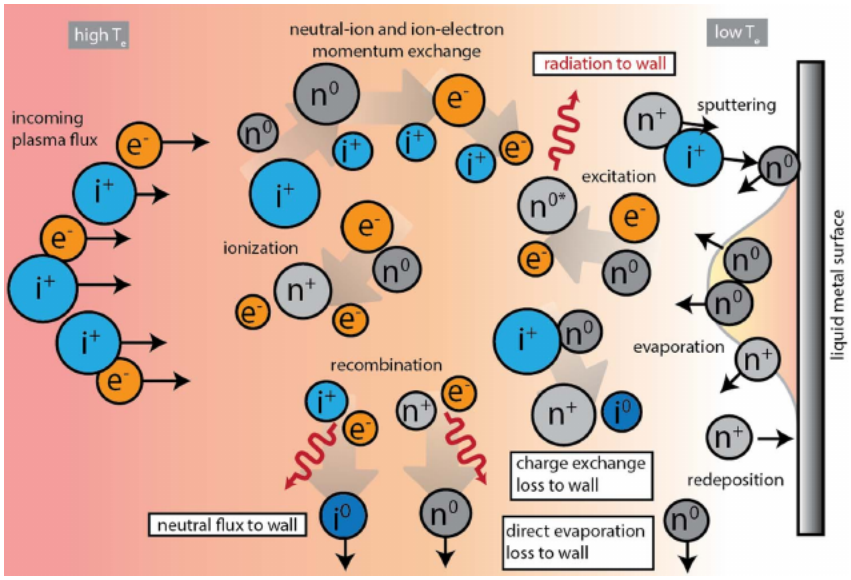

Fig. 2.2: Schematic diagram of the plasma wall interactions effects. Courtesy of [51].

2.1.3 Redeposition

Particles exhausted from the liquid surface will eventually redeposit at a generally different area of the chamber. If the particle redeposits at the liquid surface, the effect on the structure of the surface is none since liquid surfaces are always flattened. The particle might be however deposited at a different surface than the liquid. This might have a beneficial or disadvantageous effect (wall coating, diagnostic damage etc.). The redeposition of the exhausted particles has to be taken into consideration in experiments where substantial exhaust is expected and especially in potential use in fusion power plants.

Interesting and important is the so called *prompt redeposition*. Prompt redeposition is the redeposition of the exhausted particle immediately after its release. In tokamak conditions it is caused mainly by gyro-rotation, if the particle is ionized before it reaches the distance of two Larmor radii R_L from the surface. Other effects include plasma sheath and other local electric fields. The amount of promptly redeposited particle can range from ≈ 0 % to > 99 % according to the conditions of the surface proximity and has to be therefore carefully determined.

2.1.4 Vapor Shielding

Evaporated or sputtered atoms released from the liquid surface by the plasma ion flux create a dense neutral gas cloud around the surface. Interaction of the neutral cloud with the incoming plasma flux results in strong radiation. The power is radiated homogeneously in all directions and thus the heat load to the wall is decreased and the damaging effects of accelerated ions suppressed. This effect is similar to impurity seeding induced plasma cooling. The main advantage is the cooling effect is self-regulating. The higher the surface temperature, the higher particle exhaust and subsequent radiation. In tokamaks or other magnetic devices, the main driving mechanism of the magnitude of the radiation (given by temperature and density) is the surface temperature of the target. With a steady state heat flux, an equilibrium of heating and cooling is always established. If sufficient amount of liquid metal is present, the only upper limit for the cooling power is the boiling point of the liquid metal or the melting point of the holding substrate material, whichever

is lower. In practice the limit is given by a maximum acceptable release due to strong diffusion into the core plasma or due to unwanted subsequent condensation outside the liquid surface [52, 25].

2.2 Potential metals and alloys in liquid metal PFC applications

2.2.1 Lithium

Lithium is the third lightest element($Z = 3$). As such it is a promising candidate for a plasma facing material. This is due to the low proton number of the element [25]. Generally, elements with high proton numbers are undesirable in a fusion plasma, both because of radiation loses , which drastically increase with proton number, and because of the fuel dilution [44]. These two effects present a maximum allowable percentage of an element in the fusion plasma. For lithium this concentration (See Tab 2.1) is very high, compared to other potential elements for a liquid divertor. Other advantage is the fact, that lithium will be utilized as a fuel breeder to produce tritium for the power plant. This means a lithium processing facilities (for example in tritium separators) will be definitely present. Lithium is with boron one of the elements used as a wall coating material. First wall coating is a technique increasing plasma performance parameters. Therefore, the released lithium from the liquid plasma facing component could condense at the solid walls of the rest of the vessel and serve as a coating material [53, 54].
The most concerning issue regarding lithium as a plasma facing material is its relatively low boiling point (Tab. 2.1). The result is a high release of lithium atoms even at temperatures considered to be potentially common in fusion power plant operation (800-1000 °C) [30, 6]. This is although not a necessarily eliminating obstacle as the idea is to operate the fusion reactor divertor at hundreds of degrees Celsius by active cooling, where the release is manageable. The potential over-release, and subsequent fuel dilution in the core plasma, would therefore be present only during catastrophic events, that would over-heat the wall and would pose a risk for the wall. The lithium layer would then be essentially a fail-safe for such events. The viability of this solution is however still to be tested.
The second of the most pressing concerns regarding lithium is fuel retention. The tritium balance of a fusion power plant is still a work in progress and retention of tritium by the liquid lithium could jeopardize the balance and be potentially unacceptable in terms of radiation safety. The alkaline metals, lithium is part of, are highly reactive with hydrogen (or its isotopes) and oxygen. The formation of lithium hydrate and other compounds is a part of this problem. This issue will surely have to be addressed if lithium is to stay as a potential candidate for a plasma facing material. Research already done, shows that for temperatures over 300 °C the retention potential of lithium drops rapidly while the dissolved hydrogen tends to be released back from the liquid [55]. Formation of Lithium oxide, which creates a solid film on the surface does prevent the formation of a liquefied plasma facing surface, however the thin layer can be sputtered away easily. [56]

2.2.2 Tin

As opposed to lithium, tin is with Z=50 considered a high Z impurity much closer with its behavior to for example tungsten Fig. 1.21. This strongly limits the amount of tin, acceptable in the plasma, to practically zero Tab. 2.1. Tin however has significantly higher boiling point, allowing considerably higher operating temperatures without substantial tin release.(See Fig. 2.12). Tin

has more suitable chemical properties than lithium, mainly lower reactivity, and lower fuel retention potential (similar to tungsten for) [57, 58]. The tin liquid plasma facing wall would therefore be chemically more stable.
Latest research indicates a stannane (SnH_4) formation inside a tin based plasma facing wall during a prolonged exposure to high temperature hydrogen/deuterium plasma. stannane is a stable compound in gaseous state under standard operation conditions (boils at -52 °C in normal atmosphere). stannane formed inside the liquid tin can create bubbles [59]. This is an obstacle not only in reference to tin release into plasma, but also to the thermal properties of the plasma facing component (i.e. thermal conductivity).

2.2.3 Tin-lithium alloy

The idea to utilize advantages of both metals and mitigate the disadvantages, resulted in a proposal to elaborate the viability of a tin-lithium alloy. The proportions of the alloy are usually in range from 80Sn-20Li to 75Sn-25Li. The alloy does not form oxides as lithium does and has a higher melting point ($\approx$ 300-400 °C, depending on the components ratio). If a homogeneously mixed alloy is heated, the different evaporation rates of the two metals result in lithium evaporation with negligible tin release, which is a desirable state. As only small part of highly energetic atoms in the Maxwell distribution at a given temperature will be released, the evaporating lithium atoms essentially cool the tin atoms, preventing them from acquiring sufficient energy to be evaporated. The alloy is therefore more similar to lithium, with higher melting point and lesser chemical reactivity with hydrogen and oxygen. [25, 57]

Material	Li	Sn	75Sn25Li	C	Mo	W
Melting temperature T_m [°C]	180.5	231.9	334	–	2623	3422
Boiling temperature T_b [°C]	1330	2602	2325	–	4639	5930
Latent heat of evaporation L_v [eV]	1.41	3.07	1.41	–	–	–
Atomic number Z	3	50	–	6	138	173
Thermal conductivity at T_m κ [W/m/K]	44	26	33	50-80	138	173
Volumetric heat capacity c_v [J/cm^3/K]	2.24	1.7	1.6	3.2-4.8	2.6	3.4
CLIP [%] [60]	25	0.03	25	7	0.07	0.002

Tab. 2.1: List of potential materials with relevant parameters [61, 62, 56]. CLIP - Contamination concentration limit in ignited plasma. For SnLi alloy only lithium is evaporated (See Section 2.2.3).

2.3 Liquid metal based plasma facing components technologies

One of the main obstacles in a liquid PFC design, is the fluidity of the metal. A support structure that wild hold the metal in place has to be carefully designed. There are several approaches currently being investigated as potential solutions.

The "simplest" solution is a flowing limiter [63]. In this design the liquid metal flows along a solid wall (See Fig. 2.3). The liquid lithium flow is driven (and regulated), by DC current. This concept has been successfully tested at EAST tokamak, resulting in improved plasma parameters (lower impurity presence, repressed recycling etc.) likely as a result of Li wall conditioning [54, 53].

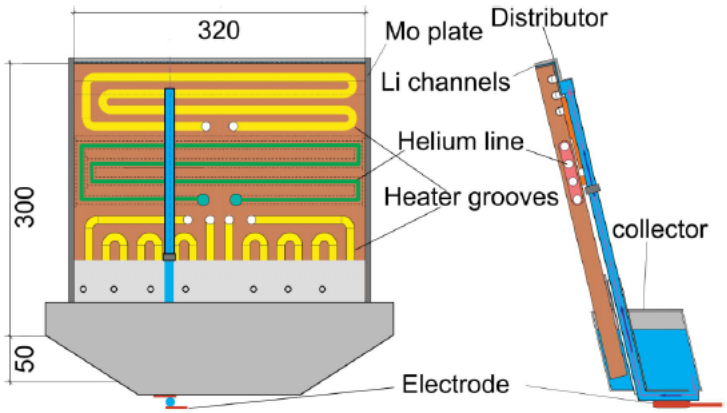

Fig. 2.3: Design of the flowing Li limiter tested at EAST tokamak. Dimensions in mm. Courtesy of [63].

Apart from direct DC current the thermo-electrical properties of the liquid metal can be utilized in flow drive. The so called Lithium–metal infused trenches design utilizes this concept [64]. The vertical temperature gradient in the liquid lithium creates a current density and the resulting $\mathbf{j} \times \mathbf{B}$ force with external magnetic field is driving the liquid metal (See Fig. 2.4). This flow is then used as a supporting heat removal mechanism, furthering the cooling potential of the system.

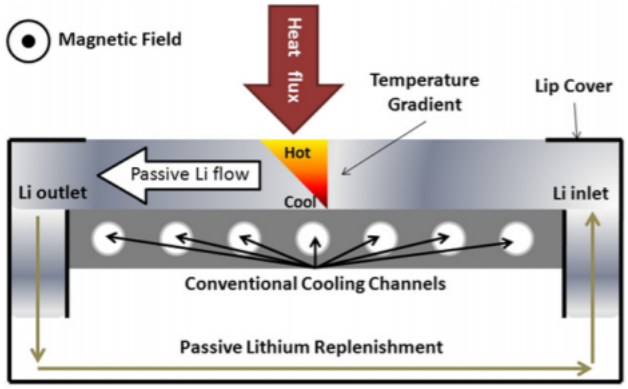

Fig. 2.4: Design of the Lithium–metal infused trenches (LiMIT) PFC. Courtesy of [64].

The flowing concepts could prove to be problematic, if implemented as a shield for the main heat load (divertor strike points) and potential transient events, where strong $\mathbf{j} \times \mathbf{B}$ forces can be induced. A more probable is the utilization of an approach where the stability of the liquid is greatly improved through capillary forces [64]. The stability of capillary based liquid metal PFCs is discussed in Section 2.4 [65].

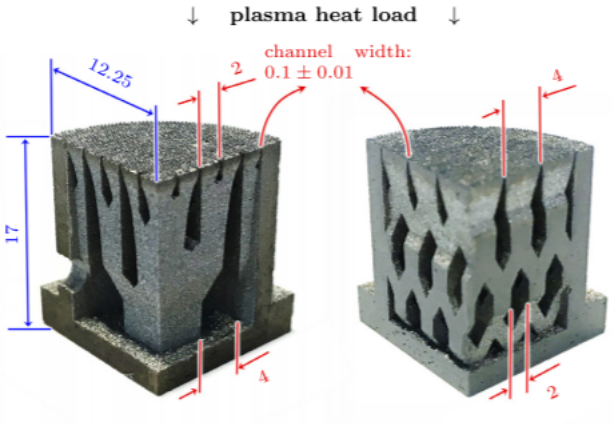

Fig. 2.5: Two designs of the 3D printed LMD. Courtesy of [65].

Capillary porous structure (CPS) is a technology utilizing capillary forces to hold a wetting liquid in a solid mesh. In tokamaks this can be used as a support structure in the construction of a liquid plasma facing component (mainly the divertor). If subjected to a high heat flux, the temperature of the CPS component rises up to the boiling point of the liquid and rises further only after the liquid is boiled away, as demonstrated by several experiments in linear devices and tokamaks (Fig. 2.6). For heath fluxes relevant for tokamak operation, the equilibrium between the heat flux and the cooling effects is established well below the boiling point. This effect could protect the currently used tungsten based divertors from high temperature rise resulting in the damage of the PFCs. The present liquid in the vacuum vessel in a plasma device also has several disadvantages, such as high particle release, due to sputtering and evaporation. [25, 50, 66].

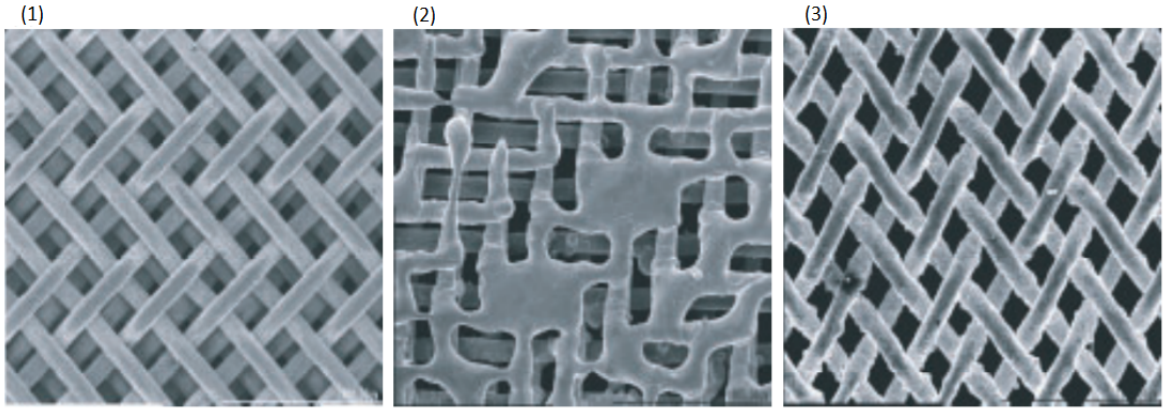

Fig. 2.6: Photographs of the CPS mesh (1) CPS wetted with Li, (2) CPS without Li after one discharge of energy Q = 4MJ/m^2, and duration t = 250 μs, (3) CPS with lithium after 22 discharges. Courtesy of [67].

The development of the CPS technology is currently focused on other porous structures, that would further increase the stability of the liquid, due to increased capillary forces. This presents a opportunity to utilize CPS based plasma facing components even in devices, where the standard mesh based CPS would not be sufficient. The mesh based CPS is however sufficient with a high margin for increase in instability inducing forces. The CPS has therefore the potential

to be magneto-hydrodynamically stable eve during otherwise destructive events such as plasma disruptions [56, 68, 69].

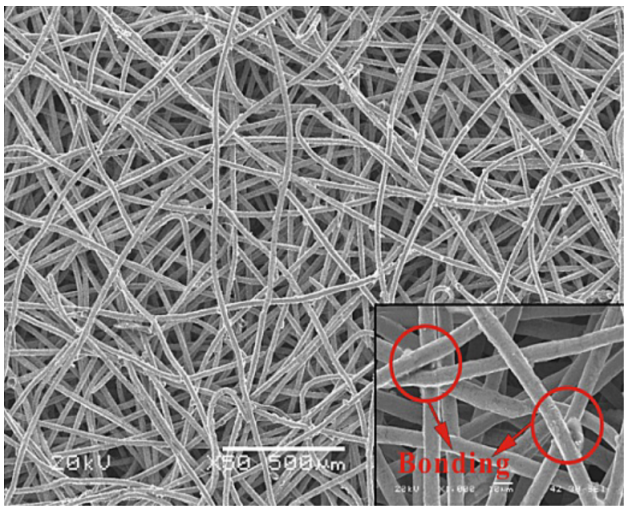

Fig. 2.7: Morphology of a stainless-steel felt with 10 μm wire thickness. Courtesy of [34].

2.4 Stability of capillary liquid metal plasma facing components

Liquid based plasma facing surfaces might be subjected to magneto-hydrodynamic instabilities 1.7. In tokamaks and other devices with strong magnetic fields the instability can be driven by the plasma pressure itself (strong shear force with small flux lines pitch angles) and also by induced currents and electromagnetic fields. The main instabilities that can develop are the Rayleigh-Taylor instability and the Kelvin-Helmholtz instability [21]. The plasma pressure itself can eject droplets from flash melted tungsten surface as shown in an experiment at the QSPA-T device [70]. For fully liquid wall MHD instabilities play significant role. If a sufficient current density is induced in the liquid metal, a strong $\mathbf{j} \times \mathbf{B}$ will be induced capable of creating unstable perturbation and subsequent droplet release, a catastrophic event in terms of plasma discharges.

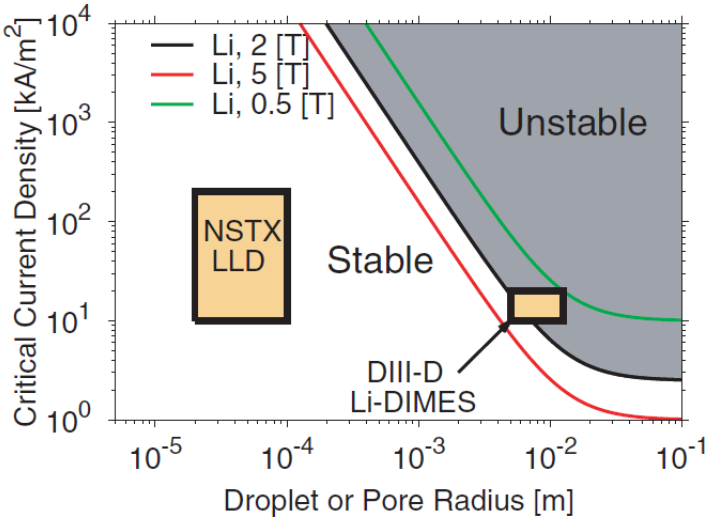

Fig. 2.8: Calculated stability diagram of LMD magneto-hydrodynamical stability. The NSTX and DIII-D operation regions highlighted. Courtesy of [21].

The theoretical stability limits calculated in [21] (See Fig. 2.8) show, that for pore sizes of the current CPS structures of 5-50 μm the system is stable for current densities (for $\mathbf{B} = 5$ T) even in ranges of hundreds of kA/m^2 to several MA/m^2, values achievable during disruption current quenches [71]. This implies the MHD stability of the CPS technologies is well above the maximal current densities predicted with sufficiently large margin for increase.

2.5 Lithium or tin based PFC in tokamaks with deuterium plasma

In tokamak experiments the most common form of erosion of the liquid surface is from deuterium ions. Effects such as preferential or self-sputtering are present, although as the amount of lithium/tin or other impurities diluted in the liquid is negligible and the energy of the ionized lithium/tin is relatively low, these can be neglected. The dominant effect will be physical sputtering, thermal sputtering or evaporation based on the surface temperature. There is no general limit, where for example evaporation will dominate because sputtering is apart from surface temperature dependent mainly on the number of impacting ions .

Sputtering

Physical sputtering of lithium or tin by deuterium ions has been experimentally measured [48], and empirical formulas giving the sputtering yields as functions of ion energy have been derived (See. Fig. 2.9).

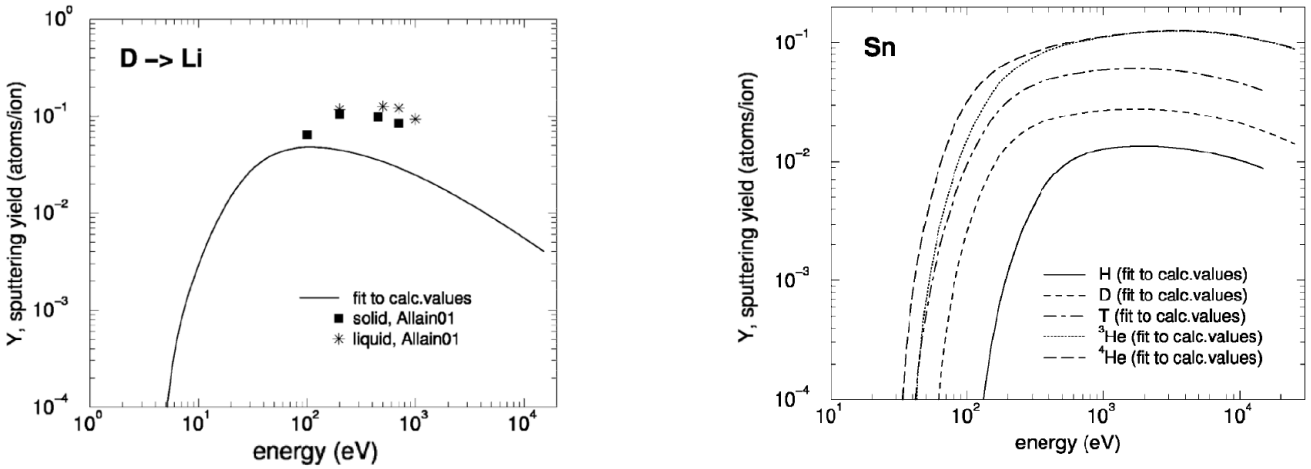

(a) Lithium **(b)** Tin

Fig. 2.9: Sputtering yields as functions of ion energy. Courtesy of [48].

The measured physical sputtering yields do not cover the total amount of the sputtered particles in the tokamak conditions. Thermal, chemical, and other effects influence to total yields. A dedicated measurement with tokamak relevant conditions had to be therefore conducted to measure and compensate for the discrepancy [49, 50]. The thermal spike model and the adatom model are the two candidates for the description in the thermal dependence of the sputtering yield. Since the thermal sputtering yield saturates, description by the adatom model is generally accepted to be more precise and is used to adjust the total yields [49, 50]. Since the chemical and other effects are not eliminated in the experiment, they are incorporated in the resulting empirical formula and do not have to be incorporated separately (the effects are minimal). The resulting formula (added to the physical sputtering) for lithium is

$$Y_{\mathrm{Li}}(T) = \frac{Y_{\mathrm{ad}}}{1 + A\exp(\frac{E_{\mathrm{eff}}}{k_{\mathrm{B}}T})}. \tag{2.2}$$

Where $Y_{\mathrm{ad}} = 2.9$ represents the effective yield based on the areal density and lifetime of adatoms, $E_{\mathrm{eff}} = 0.7$ eV is the sublimation energy of adatoms and $A = 9.6 \times 10^{-6}$ [49, 50]. The experimental data used as a basis for the formula are in Fig. 2.10.

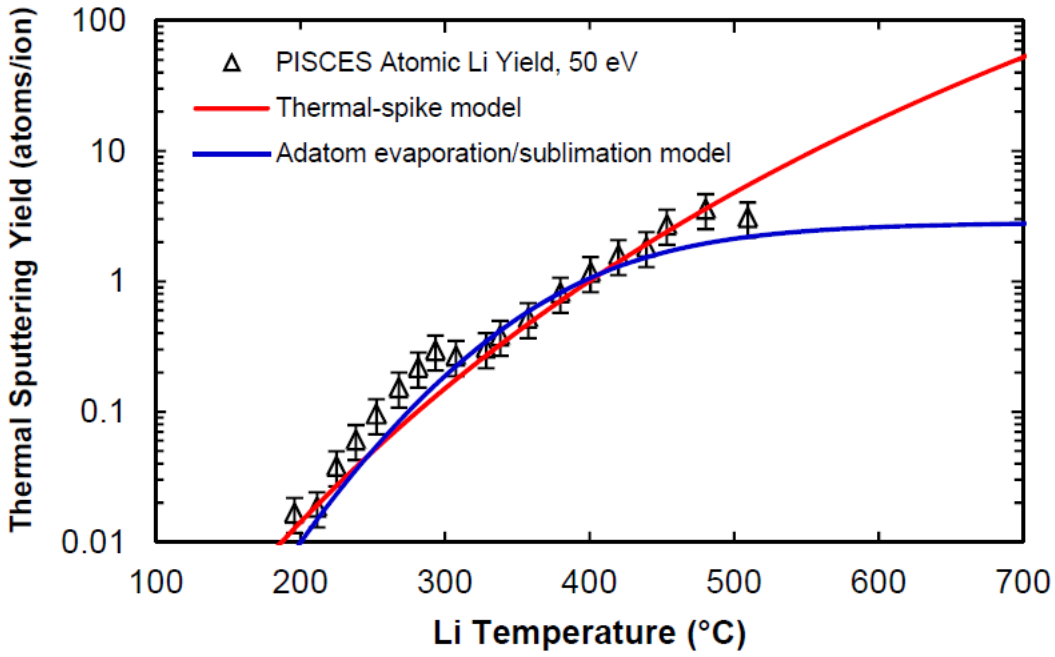

Fig. 2.10: Li by D at 50 eV thermal sputtering measurement at PISCES-B. Red line is Eq. 2.2 Courtesy of [72].

Tin sputtering increase due to the increasing temperature can be expressed with the empirical formula

$$Y_{\mathrm{Sn}}(T) = Y_{\mathrm{eff}} \exp(-\frac{E_{\mathrm{eff}}}{k_{\mathrm{B}}T}). \tag{2.3}$$

$Y_{\mathrm{eff}} = 0.2$ $E_{\mathrm{eff}} = 0.27$ eV [50]. The fact that the resulting adatom bond energy $E_{\mathrm{eff}} = 0.27$ is five times lower than for argon or helium implies, that not only thermal effects change the total yield in case of hydrogen erosion, but a chemical reactions contribute as well. This would imply a chemical reaction. Formation of stannane (SnH_4) is has been proposed as the solution, however the gas should quickly decompose in the experimental conditions. More research is needed to correctly explain the discrepancy [73].

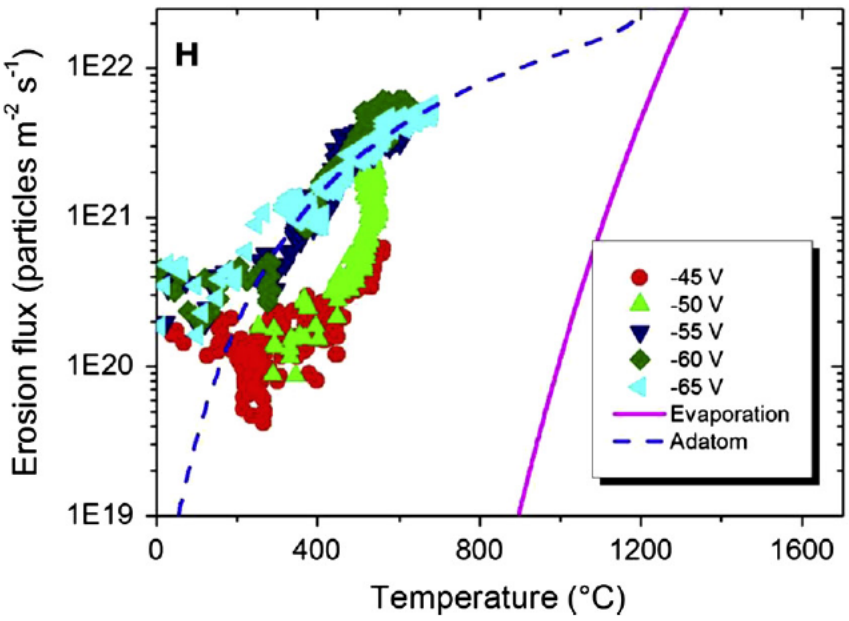

Fig. 2.11: Experimental results of anomalous tin sputtering from the Pilot-PSI device. Dashed blue line corresponds to Eq. 2.3. Courtesy of [50].

Evaporation

Calculation of lithium and tin evaporation rates can be done through the Langmuir formula (2.1). In tokamak experiments conditions, the vacuum expansion assumption can be made, making the calculation easier. With the vapor pressure values at given temperatures, the equation (2.1) results in evaporation flux rate as a function of surface temperature. The resulting evaporation flux rates are in Fig. 2.12. Interesting and notable observation is, that in case of tin-lithium alloy, only lithium atoms are evaporated, probably due to a preferential effect as described in Section 2.2.3. [62, 25, 74].

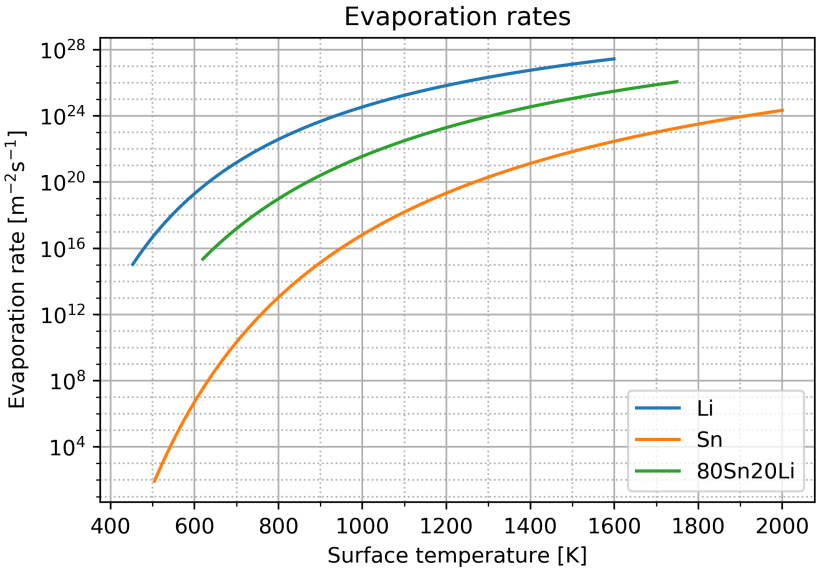

Fig. 2.12: Evaporation rates of Li, Sn and 80Sn20Li alloy.

Vapor shielding

The eroded (sputtered or evaporated) atoms cool the surface of the plasma facing component. The first part of the cooling is the subtraction of evaporation latent heat. Latent heat is the heat required for a change of state. This energy is equal to the binding energy in the liquid. For lithium $\boldsymbol{E_{Li} = 1.41\ eV}$ and for tin $\boldsymbol{E_{Sn} = 3.07\ eV}$ per particle.

The second cooling mechanism is the radiation (dominantly line-radiation) of the neutral cloud formed around the surface from the exhausted atoms. For the purposes of thermal study of the liquid surface, the crucial parameter is the total radiated power (from all sources). Due to the complexity of the system, the state distribution, which along with density determines the total power has to be calculated numerically. One of the numerical models used mainly in spectroscopy is the FLYCHK model [43]. The total radiated power in a given density and temperature is part of the AMDIS database [75]. However, the FLYCHK code is imprecise for fully ionized plasma or plasma close to this state [43]. This means the results for tin are to be trusted more than the results for lithium as lithium plasma can be fully ionized even in the SOL or in the vicinity of the LM surface. The reason is the higher importance of collision caused radiation in the Li plasma. For that reason, it is much preferable to utilize data from models dedicated more to the conditions near the liquid metal surface. The calculations done as a part of the vapor-box divertor concept in [76] serve this purpose. The radiated power per particle for lithium is in Fig. 2.13 and for tin in Fig. 2.14.

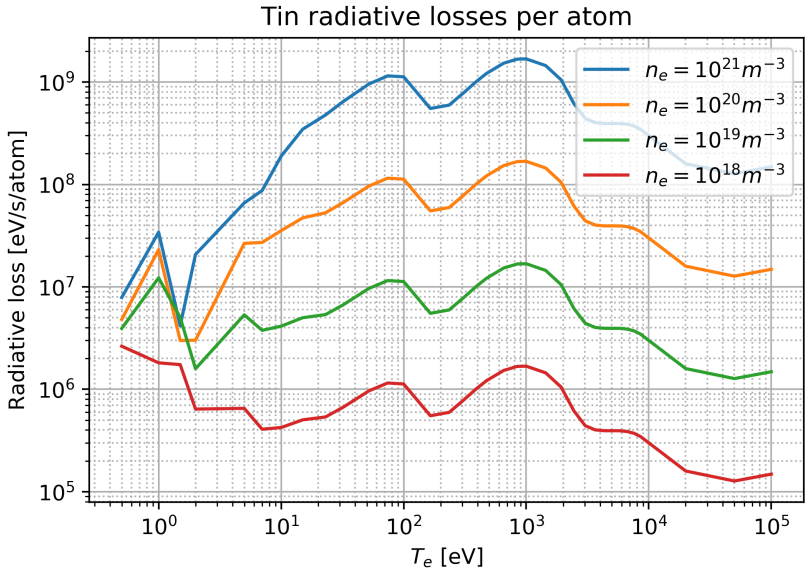

Fig. 2.14: Total radiation power of Sn at given electron temperatures T_e and densities n_e per second by one atom. Results from FLYCHK model [43] at AMDIS database [75].

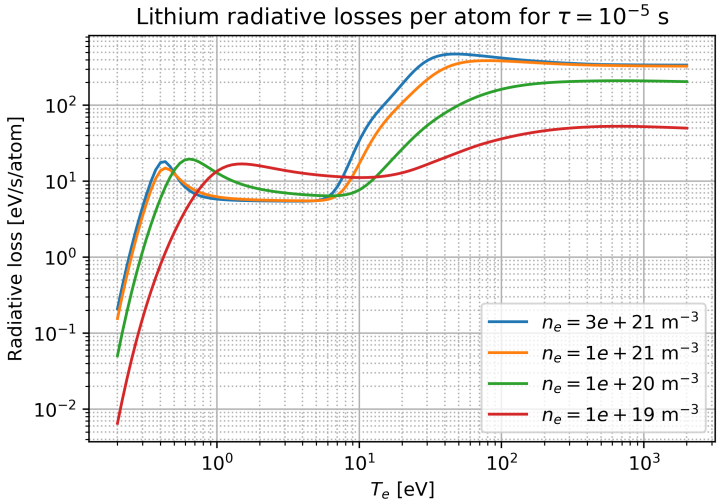

Fig. 2.13: Total radiation power of Li at given electron temperatures T_e and densities n_e for Li atom residence time $\tau = 10^{-5}$ s. Calculated by J. Schwartz through [77].

3. Modeling of a Capillary porous structure (CPS) divertor thermal behavior

3.1 3D Heat Transport model

For the purposes of the liquid metal experimental campaigns at the COMPASS tokamak and other experimental campaigns, a 3D heat model has been developed. The 3D Heat transport model consists of two parts. One is the three dimensional thermal diffusion based on the thermal conduction equation and cooling effects of the particle release (sputtering and evaporation) and radiative cooling based on the Stefan–Boltzmann law $P_{\mathrm{SB}} = \sigma T^4$. The simulated target is divided into finite number of block of constant temperature. The input into the model is perpendicular heat flux $q_{\perp}(x, y, t)$ where the x coordinate corresponds to radial position and y to the toroidal coordinate [78, 56].

3.1.1 Heat conduction

The thermal conduction inside a material follows the heat equation

$$\frac{\partial T}{\partial t} = -\frac{1}{c_{\mathrm{v}}} \nabla \cdot [\kappa(T) \nabla(T)] \,, \tag{3.1}$$

where T is temperature, c_v and κ is heat conduction [15, 79].

The equation is derived from equations for heat flux and heat flux caused temperature change

$$\mathbf{q} = -\kappa \nabla(T), \tag{3.2}$$

$$\frac{\partial T}{\partial t} = \frac{1}{c_{\mathrm{v}}} \nabla \cdot \mathbf{q}. \tag{3.3}$$

Effectively, equations (3.1) and (3.3) are used to calculate the temperature in the simulated area in up to three dimensions. Heat flux from the plasma causes a temperature increase by Eq. (3.3) and the heat equation (3.1) gives the solution for the temperatures of the remaining parts. The temperature gradient is responsible for cooling of the surface until the temperatures at each boundaries are equal. These possible boundary conditions are utilized for the back side of the target:

- No boundary condition (only initial value) - the block is bordered by vacuum (thermal radiation is negligible for temperatures $T < 3000$ K.)
- Back temperature set to fixed value - The target is actively cooled by a flowing medium of the given temperature.

3.1.2 Particle exhaust cooling

The effects of particle exhaust on the surface temperature are incorporated as a correction of heat flux q to the surface. The cooling power is calculated as a product of particle exhaust flux and cooled energy per particle.

$$q' = q - (\Gamma_{\mathrm{sp}} + \Gamma_{\mathrm{vap}})(1 - R)(\epsilon_{\mathrm{cool}} + E_{\mathrm{vap}}). \tag{3.4}$$

Γ_{sp} is the flux of sputtered particles, Γ_{vap} is the flux of evaporated particles, R is the prompt redeposition coefficient, ϵ_{cool} is the energy cooled by radiation and ionization in the neutral cloud per released particle and E_{vap} is the latent heat of evaporation per released particle. [78, 56]. In Section 4.2.2 it is shown, the heat flux can be calculated from Eq. (4.2). Important note is this gives the parallel heat flux. The actual perpendicular heat flux is $q_{\perp} = \sin(\alpha) q_{\parallel}$ i.e. the parallel heat flux multiplied by sinus of the angle between the surface and the field flux line.

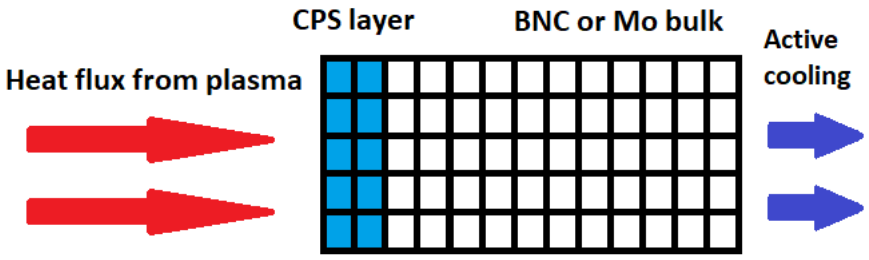

Fig. 3.1: A schematic diagram of the 3D heat model simulation of a CPS plasma facing component.

Eq. (3.4) assumes the vapor shielding is *local*, meaning the power loss due to radiation is subtracted at the location of the particle release. This is the case for instances where the mean free path of the released of the neutral L_{mfp} is shorter, than the grid block size, or at least smaller than the hot-spot radius r_{hs}.
If the mean free path L_{mfp} of the neutral is longer, the radiation will be spread over a larger area effectively decreasing the cooling capacity (and cooling outside the hot spot). The latent heat is always subtracted at the point of release and is therefore always local. To correctly model the situation where the cooling is *global*, the Eq. (3.4) has to be modified.
The local part of the cooling by latent heat will be

$$q_{\mathrm{loc}}^{\mathrm{cool}} = (\Gamma_{\mathrm{sp}} + \Gamma_{\mathrm{vap}})(1 - R)(E_{\mathrm{vap}}). \tag{3.5}$$

The spreading neutral radiating cloud can be approximated by a sphere. The radiative cooling will then be distributed in the volume of the sphere, and the cooling power density proportionally lowered. With accommodated projection of the sphere on the surface, the resulting *global* cooling will be

$$q_{\mathrm{glob}}^{\mathrm{cool}} = \int_{S_{\mathrm{LMD}}} \frac{(\Gamma_{\mathrm{sp}} + \Gamma_{\mathrm{vap}})(1 - R)\epsilon_{\mathrm{cool}} \mathrm{d}S}{L_{\mathrm{mfp}}^2}, \tag{3.6}$$

i.e. the cooling power density integrated over the LMD surface (or rather the hot-spot, as cooling power is negligible outside of it), divided by the sphere projection surface.
It is apparent, that a large radiating sphere lowers the cooling power density. This formula is

universal, even though it would diverge to infinity for small radiating spheres, however this is a non-physical scenario, as the sphere cannot be smaller than the hot-spot itself, i.e. the radiative cooling is essentially local . The resulting cooling power at a given coordinate will be

$$q' = q - q_{\text{glob}}^{\text{cool}} - q_{\text{loc}}^{\text{cool}}. \tag{3.7}$$

If $L_{\text{mfp}} << r_{\text{hs}}$, $q_{\text{glob}}^{\text{cool}}$ can be added into one term.

The variability of the model allows it to be used in simulations of overly different scenarios, from simulations of LMD behavior to predictions of probe heating. In the following sections simulations of LMD behavior at COMPASS-U tokamak (Section 4) and at ALIMAT-F experiment (Section 5) are discussed [78, 56, 80, 81].

3.2 Simulations of the COMPASS tokamak liquid metal experiment

The model described in this chapter, was successfully used for simulations of the COMPASS tokamak liquid metal CPS experiments power handling [56, 82, 80, 83]. The campaign consisted of plasma exposure of two LMD cylindrical-like targets with dimensions of $45 \times 25 \times 21$ mm covered with 1 mm thick CPS layer (several planes of the mesh) with wire diameter of 100 μm and pore thickness of 75 μm wetted by pure lithium and 80Sn-20Li alloy with molybdenum and CPS bulk respectively. The targets were exposed to both L-mode and H-mode plasma with maximal heat fluxes $q = 17$ MW/m^2 (Li L-mode), $q = 12$ MW/m^2 (Li and Sn-Li H-mode). The high heat fluxes were given by large incidence angles (up to 45°), achieved through vertical insertion above neighboring divertor tiles (Fig. 3.2) [80].

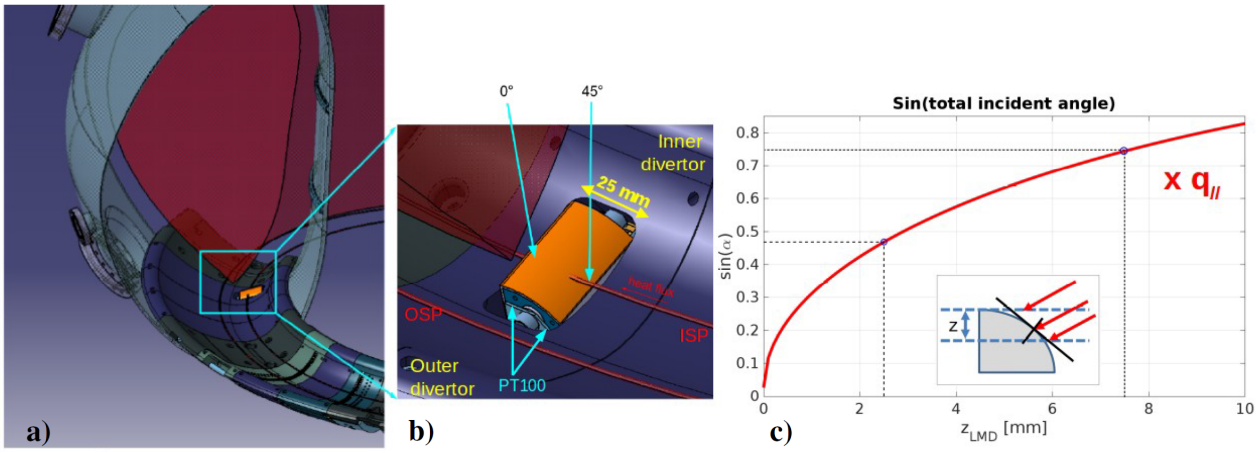

Fig. 3.2: a) CAD model of the LMD target in the COMPASS tokamak chamber b) Zoomed view c) Graph and diagram of the field lines incidence angle as a function of insertion height z. Courtesy of [80].

The simulations revealed, no significant effect of vapor shielding has been achieved, due to the large mean free path of the neutral lithium. The radiating cloud with a diameter of 12 cm was significantly larger than the 10 mm hot spot, thus radiating and cooling plasma outside the heated area. This led to the separation of the always local cooling effect by latent heat subtraction and possibly global effect of radiative cooling. The global effect of the cooling caused by the radiation was decreased from ≈ 15 MW/m^2 to ≈ 0.15 MW/m^2, i.e. by a factor of 100 [82, 56], which led

to the correct correlation of surface temperature time evolution from IR camera measurement and the simulations (Fig. 3.3).

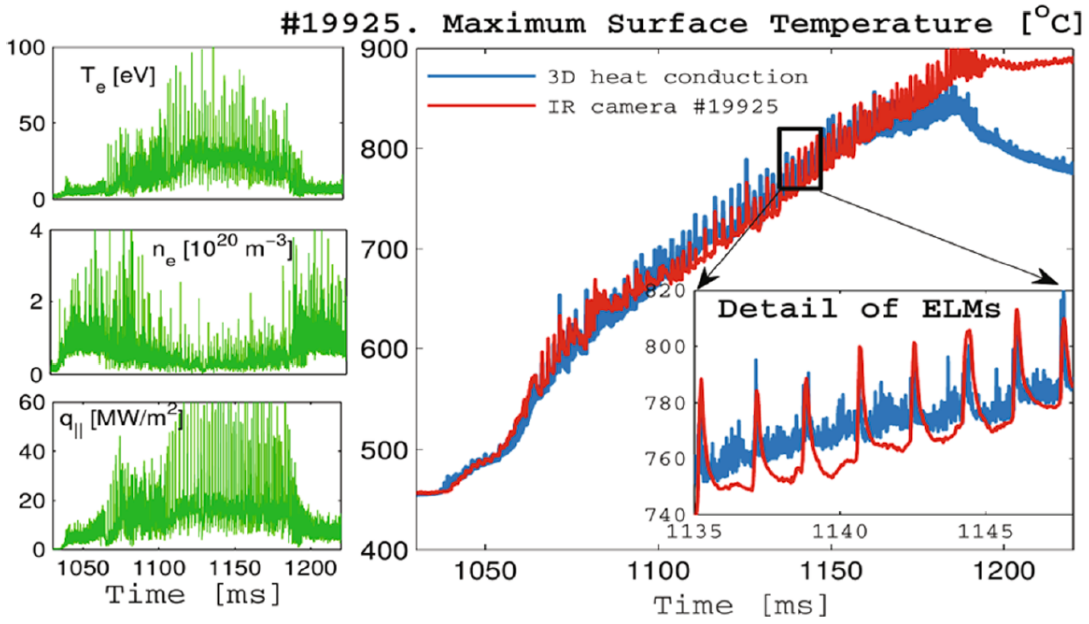

Fig. 3.3: Temporal evolution of the LMD maximal surface temperature from IR camera measurement (red) and the simulation (blue), with input data from divertor probe array (left in green), during discharge #19925. Courtesy of [56].

One of the main goals of the experimental campaign, to achieve balance of power between the heat flux from plasma and conduction and vapor cooling was however not achieved. Partly due to low parameters (heat flux and discharge length) and, in case of the Sn-Li BNC target, partly by low insertion into plasma. The effects of the power balance with continuing particle exhaust are crucial in determining the viability of the LMD technology for future fusion devices. For that reason, it is expected to continue with these experiments in the new COMPASS-U tokamak, currently under construction [84].

4. Simulations of COMPASS Upgrade liquid metal experiments

4.1 COMPASS Upgrade

COMPASS Upgrade, abbreviated *COMPASS-U*, is a new medium size tokamak currently in the design stage at the Institute of Plasma Physics of the Czech Academy of Sciences in Prague, Czech Republic. With the high toroidal magnetic field, densities, and extensive plasma heating (Tab. 4.1 it will provide a unique opportunity to study advanced plasma physics configurations, operation regimes and other related fields under ITER and DEMO relevant conditions. One of the distinct characteristics of the COMPASS-U tokamak will be its metallic wall capable of operation at temperatures up to 500 C°. This and the possible plasma regime with ITER and DEMO relevant heat-fluxes make a perfect device to study plasma facing components designs and the related physics, one of which are the liquid metal plasma facing components technologies [84].

COMPASS-U parameters		
Quantity		value
Toroidal field	B_t	≤ 5 T
Plasma current	I_p	≤ 2 MA
Major radius	R	0.9 m
Minor radius	a	0.27 m
Triangularity	δ	0.3-0.6
Elongation	κ	≤ 1.8
Plasma volume	V	2.1 m^3
Plasma surface at separatrix	S	13 m^2
NBI heating power (initially)	P_NBI	4 MW
ECRH heating power (initially)	P_ECRH	1-2 MW

Tab. 4.1: COMPASS Upgrade tokamak designed parameters [84].

The first liquid metal experiment at the COMPASS-U tokamak will consist of a single divertor tile mounted on a horizontal manipulator in the divertor area. The tile will be covered with a CPS layer and wetted with a liquid metal with an inside reservoir for replenishment of the metal exhausted from the surface due to interaction with the plasma. The schematics of the COMPASS-U first wall and divertor are in Fig. 7.11 and a close-up with the CPS tile is in Fig. 4.1.

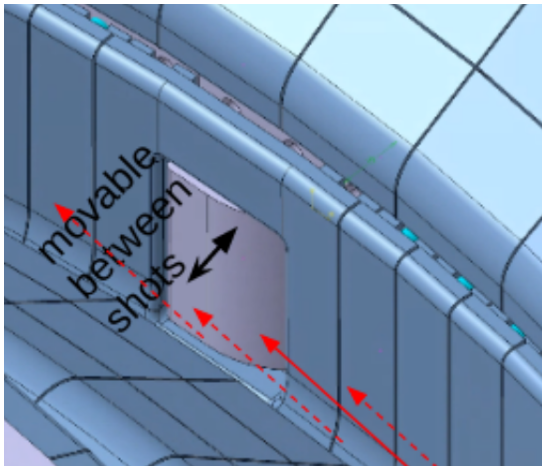

Fig. 4.1: Close-up schematics of the COMPASS-U divertor port with the future LMD tile. Courtesy of [81].

The simulations of the COMPASS-U liquid metal experiments presented in this chapter considered two possible H-mode regimes of operation (in Tab. 4.2).

Regime	B_t [T]	I_p [MA]	n_e [m^{-3}]	q_{95} [-]	β_n [-]	P_{Ohm} [MW]	P_{NBI} [MW]	P_{ECRH} [MW]
3200	2.5	0.8	1×10^{20}	3.4	1.28	0.4	1.8	0
6400	5	2	2.2×10^{20}	2.7	1.05	1.2	3.6	1.7

Tab. 4.2: COMPASS-U H-mode regimes utilized in the LMD experiments simulations.

4.2 COMPASS Upgrade divertor heat fluxes

As part of the liquid metal divertor simulations, correct input data have to be obtained. The main plasma parameters influencing the simulations are:

- Perpendicular heat flux $P_\perp$ - Surface temperature
- Electron temperature - Vapor cooling intensity
- Plasma density - Vapor cooling intensity, sputtering flux

There are several approaches to obtain the correct values of these quantities. One is to calculate the divertor heat fluxes from known power that crosses separatrix and is then mapped to the divertor through magnetic field geometry. From the calculated heat flux, density and temperature is derived. Another approach is to scale measured densities and temperatures from other devices and subsequently derive the resulting divertor heat flux profile.

4.2.1 Calculation from P_{SOL}

Power crossing the separatrix is dependent on the Ohmic heating, auxiliary heating (NBI, ECRH etc.) and fusion power. In case of COMPASS-U, fusion power is negligible because tritium will not be used as a fuel. To precisely calculate the separatrix crossing power a numerical model

has to be used. Calculations of various predicted scenarios for COMPASS-U have been conducted in the METIS code.

METIS is a comprehensive numerical code utilizing 1D current diffusion and 2D equilibrium models as well as various heat and particle transport models to provide complex results of various plasma parameters for predictions and analysis of plasma experiments [85].

Along with the calculated power P_{SOL} the power decay length λ_{q} is calculated. λ_{q} can be calculated from an empirical scaling formulas [86] incorporated in the METIS code. The FIESTA code was used to calculate magnetic equilibrium for COMPASS scenarios [87]. These two parameters can be then used to map the heat flux to the divertor. The scaling law used to calculate the heat flux profile is

$$q_{\parallel}(\overline{r}) = \frac{q_{0\parallel}}{2}\exp\left(\left[\frac{S}{2\lambda_{\mathrm{q}}}\right]^2 - \frac{\overline{r}}{\lambda_{\mathrm{q}}}\right)\operatorname{erfc}\left(\frac{S}{2\lambda_{\mathrm{q}}} - \frac{\overline{r}}{S}\right), \tag{4.1}$$

where $q_{0\parallel}$ is the peak heat flux, $\overline{r} = r - r_{\mathrm{sep}}$ is the radial distance from the separatrix. The parameter S describes the heat flux spreading into the SOL and the private flux region [88, 31]. The resulting divertor heat flux profile is in Fig. 4.2.

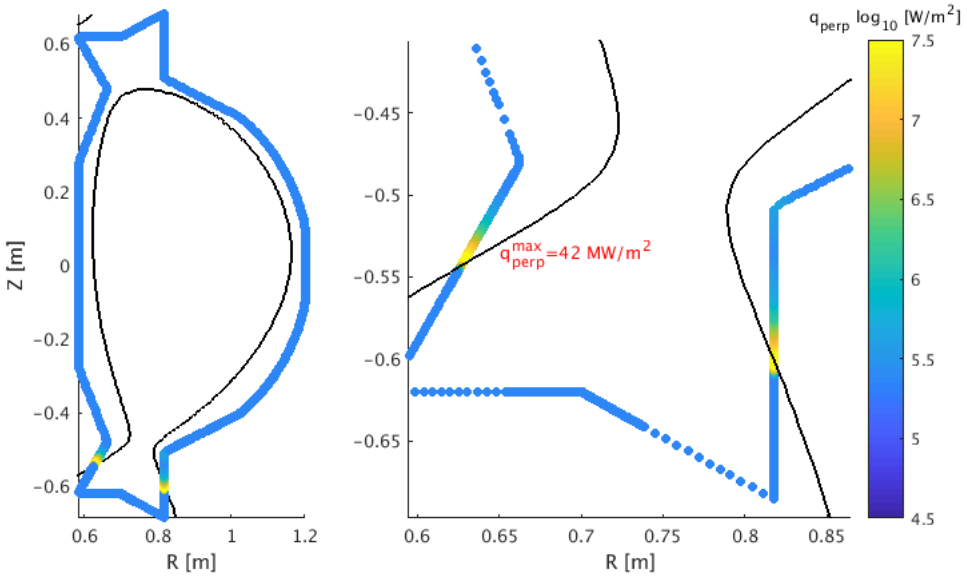

Fig. 4.2: Predicted heat fluxes to the wall at COMPASS-U during scenario #6400 ($B_{\mathrm{t}} = 5$ T, $I_{\mathrm{p}} = 2$ MA) during flat top with maximal heating (4 MW NBI and 2 MW ECRH), peaking at 42 MW/m^2.

This approach is easily applied for various scenarios (provided the METIS and FIESTA calculations are available). However, it only results in a L-mode profile. Since the study of ELM influence on the liquid metal divertors is highly desirable, this approach is insufficient. But as it was readily available and the first baseline simulations are best done in L-mode discharges, it served as a basis for the COMPASS-U simulations, which benefited the continuing design of the experiment (See Section 4.3).

4.2.2 Heat flux scaling from COMPASS probe measurements

The other approach for COMPASS-U heat flux scaling is to scale-up experimentally obtained values of $q_{\perp}, n_{\mathrm{e}}$ and T_{e} from COMPASS. The new divertor probe array is highly suitable for this

approach as it provides measurements of these quantities with microsecond temporal resolution [89, 11]. This allows H-mode ELM/inter-ELM phases to be differentiated with even the ELM filaments to be recognizable with temporal resolution in microseconds.

Divertor probe array measurement of the parallel divertor heat flux

Parallel divertor heat flux can be obtained from the equation

$$q_{\parallel} = \gamma j_{\mathrm{sat}}^{\mathrm{i}} T_{\mathrm{e}}, \tag{4.2}$$

i.e. as the product of sheath heat transmission coefficient γ, ion saturation current density $j_{\mathrm{sat}}^{\mathrm{i}}$ and the electron temperature T_{e}, where the ion temperature equal to the electron temperature and no secondary electron emission are assumed.

- **Sheath heat transmission coefficient**
  The value of sheath heat transmission coefficient for COMPASS tokamak has been experimentally evaluated through comparison of divertor heat flux profiles measured by the probe array and IR camera (spatial-temporal temperature measurement of a designated graphite tile and subsequent calculation in the THEODOR code) to be $\gamma = 11$ [90].

- **Ion saturation current density**
  If a Langmuir probe is biased to a high enough negative potential, it will repel essentially all incoming electrons. The resulting electrical current measured by the probe is called the *ion saturation current*. The ion saturation current density $j_{\mathrm{sat}}^{\mathrm{i}}$ is therefore equal to the ion saturation current divided by the facing surface of the probe. The electron saturation current (similar but with positively biased probe) could in principle also be used to measure the parallel heat flux, but as seen in the probe I-V characteristics in Fig. 4.3, the electron saturation region is not as clear as the ion one and is several times higher, meaning correct measurements require more robust diagnostic electronics.

- **Electron temperature** Although only a single Langmuir probe is sufficient to measure the electron temperature (through fitting of the probe I-V characteristics), if a set of a Langmuir and a ball-pen probe is used the temporal resolution of the temperature measurement is increased to ≈ 1 μs. The electron temperature can be obtained as

  $$T_{\mathrm{e}} = \frac{\Phi^{\mathrm{BPP}} - V_{\mathrm{fl}}}{\alpha}, \tag{4.3}$$

  where Φ^{BPP} is the ball-pen probe measured plasma potential, V_{fl} is the Langmuir probe measured floating potential and $\alpha = \alpha_{\mathrm{LP}} - \alpha_{\mathrm{BPP}}$ is a coefficient given by the probes characteristics as

  $$\alpha_{\mathrm{probe}} = \ln\left(\frac{I_{\mathrm{sat}}^{\mathrm{e}}}{I_{\mathrm{sat}}^{\mathrm{i}}}\right).$$

  For COMPASS tokamak deuterium plasma the coefficients are $\alpha_{\mathrm{LP}} = 2$ and $\alpha_{\mathrm{BPP}} = 0.6$ thus $\alpha = 1.4$.

This approach of parallel heat flux measurement is also beneficial as it directly gives the electron temperature and the ion saturation current, which are essential in vapor cooling effects calculations (T_{e} for radiative cooling evaluation and $j_{\mathrm{sat}}^{\mathrm{i}}$ for ion impact flux $\Gamma_{\mathrm{D}} = j_{\mathrm{sat}}^{\mathrm{i}}/e$ and plasma density at the target $n_{\mathrm{e}}^{\mathrm{t}} = j_{\mathrm{sat}}^{\mathrm{i}}/c_{\mathrm{s}}e$).

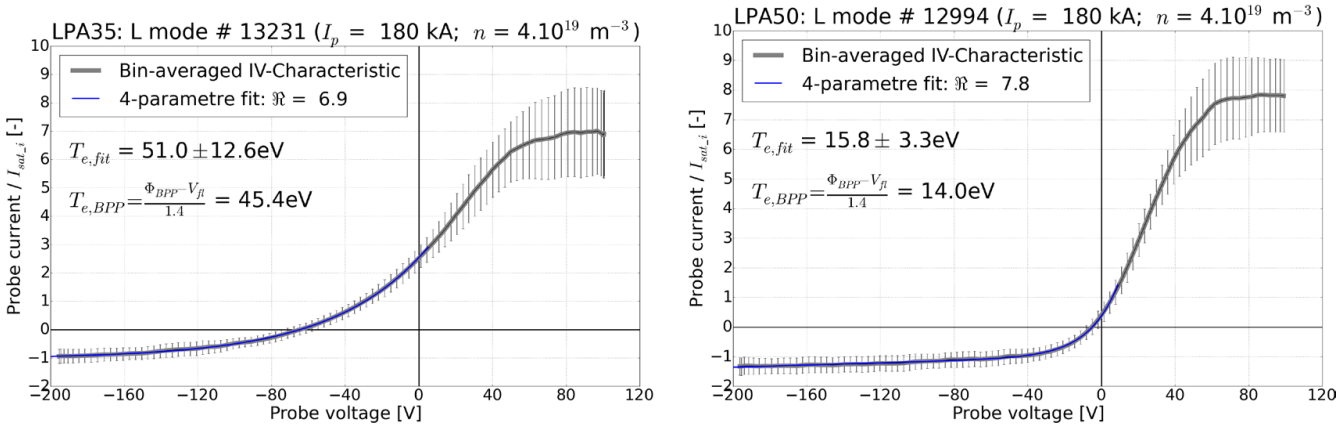

Fig. 4.3: Probe I-V characteristics in the vicinity of the LFS strike-point (left) and far in SOL on the LFS (right) taken over the whole flattop phases of two similar L-mode COMPASS tokamak discharges. Both characteristics are normalized to the ion saturation current. Courtesy of [11].

COMPASS-U divertor parameters

The inter-ELM parallel heat flux at COMPASS divertor $q_{\parallel}^{\mathrm{C}}(t,R)$ given by Eq. (4.2) from electron temperature $T_{\mathrm{e}}^{\mathrm{C}}(t,R)$ and ion saturation current density $j_{\mathrm{sat}}^{\mathrm{C}}(t,R)$, measured by the new COMPASS divertor probe array (See. Section **??**), was scaled according to the predicted Eich profile [88], similarly to the first case. The resulting heat flux profile for COMPASS-U (in Fig 4.5) provided through Eq. (4.2) the formula to calculate the ion saturation current $j_{\mathrm{sat}}^{\mathrm{C}}(t,R)$ with respect to the expected electron density at the divertor $T_{\mathrm{e}}^{\mathrm{CU}}(t,R)$.

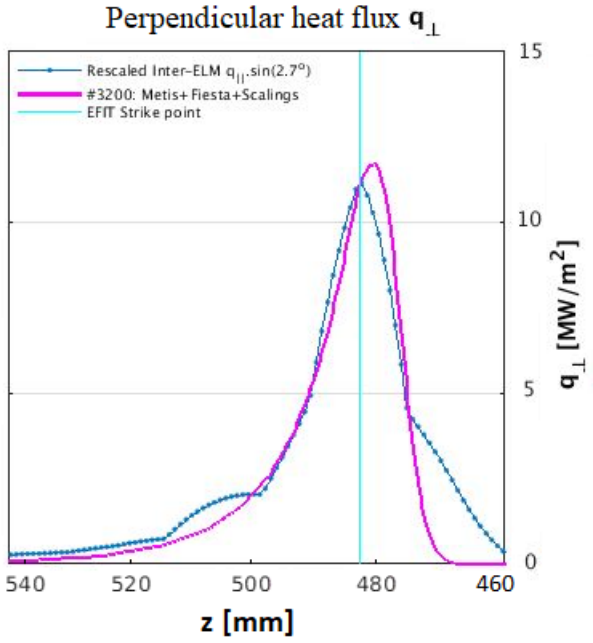

Fig. 4.4: Heat flux profile averaged over a part of COMPASS-U flat top phase (t = 1.11-1.13 s) of scenario #3200. Comparison of the METIS+FIESTA+Eich profile (magenta) and the profile scaled from COMPASS divertor probes measurement (blue). Teal is EFIT position of the strike point on COMPASS for reference.

Both FIESTA modeling and the simple two point model (See. Section 1.5.2) were used to evaluate the divertor electron temperature $T_e^{CU}(t, R)$. This proved to be problematic, as the operation regime of COMPASS-U seems to be at the threshold between the low and high recycling regimes, manifesting in the fact, that a small variation in the input parameters (temperature and density at the pedestal) resulted in a high variation in the divertor parameters. After a thorough investigation a possible electron temperature range of 10-30 eV has been agreed upon, by the COMPASS team. The densities were also changed accordingly so that the heat flux is the same. The two resulting n_e profile sets are in Fig. 4.7 and 7.3. The T_e profiles are in Fig. 4.6 and Fig. 7.2.

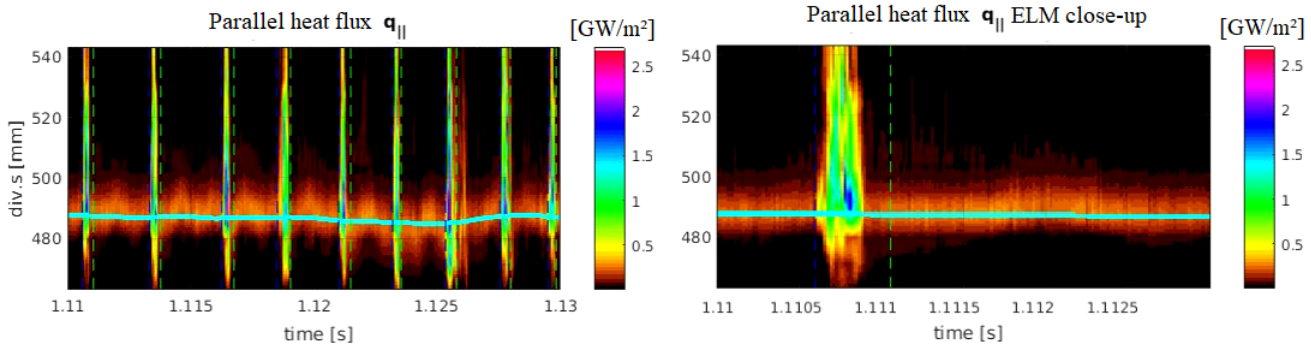

Fig. 4.5: Heat flux profile during a part of COMPASS-U flat top phase (t = 1.11-1.13 s) of scenario #3200, scaled from COMPASS divertor probes measurements (left) and ELM zoom-in (right).

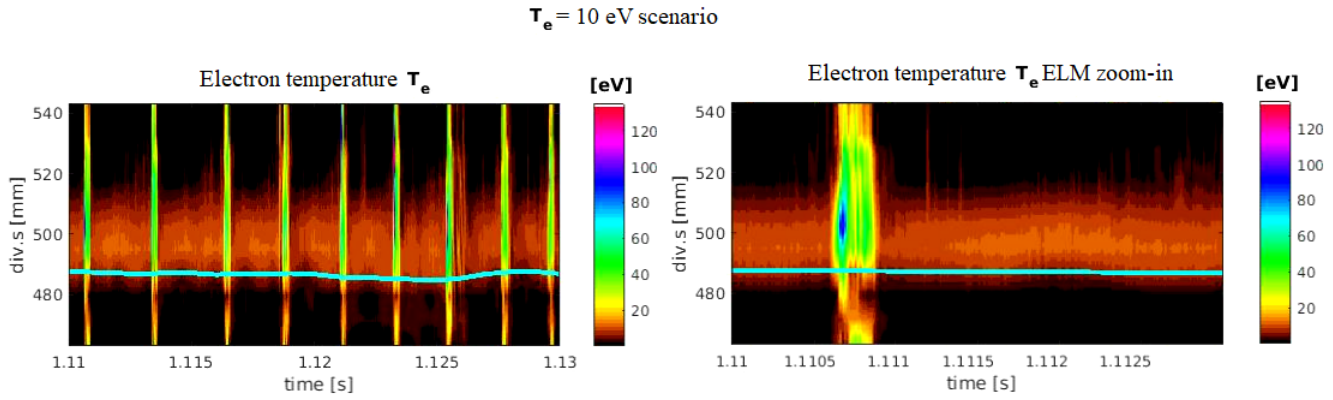

Fig. 4.6: Electron temperature profile during a part of COMPASS-U flat top phase (t = 1.11-1.13 s) of scenario #3200 with T_e = 10 eV, scaled from COMPASS divertor probes measurements (left) and ELM zoom-in (right).

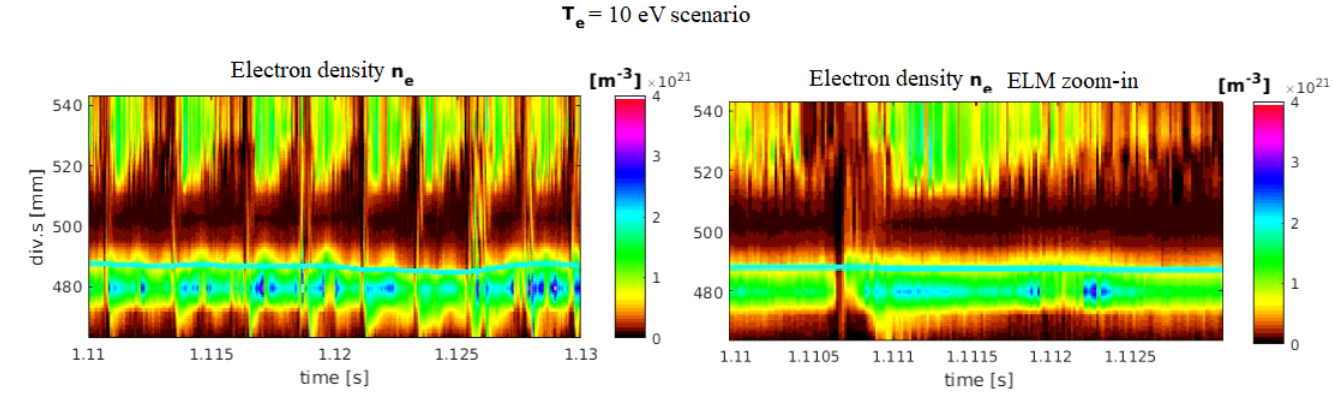

Fig. 4.7: Electron density profile during a part of COMPASS-U flat top phase (t = 1.11-1.13 s) of scenario #3200 with T_e = 10 eV, scaled from COMPASS divertor probes measurements (left) and ELM zoom-in (right).

The scaling law (4.1) does not applies only to L-mode or inter-ELM H-mode phases. In order to correctly scale ELM parameters, other approach has to be used. According to the ELM energy fluence scaling law (1.16), for COMPASS-U scenario #3200 $\varepsilon_{\parallel} \approx 300$ KJm^{-2}. Assuming the same timescale and temporal profile of the divertor heat flux as for COMPASS ($t_{\mathrm{ELM}} \approx 0.5$ ms), the heat flux during COMPASS-U ELMs was derived (peaking at $q_{\parallel,\mathrm{ELM}} \approx 1$ GW/m^2). ELM divertor electron temperature is assumed to be 10-20 % of the pedestal temperature i.e. $T_{\mathrm{e,ELM}} = 150$ eV, similar to the electron temperature at JET tokamak [91]. Density is given from Eq. (4.2), from the derived heat flux and electron temperature. The two resulting n_e profile sets are in Fig. 4.7 and 7.3. The T_e profiles are in Fig. 4.6 and Fig. 7.2.

4.3 Simulations of COMPASS-U scenario #6400

The first simulations of a COMPASS-U liquid metal divertor target experiment were performed for the scenario #6400, the scenario with maximal power (See Tab. 4.2). The design of the tested target was a CPS covered target inserted through the divertor port (Fig. 4.1) with surface parallel to the neighboring divertor tiles. Therefore, the heat load on the target would be the same as on the rest of the divertor, simulating in a smaller scale a scenario with a full liquid metal divertor. The simulations immediately showed, this would be an unrealistic experiment, as the tungsten would be melted during the discharge, even in L-mode discharges. This scenario would likely require extensive impurity seeding to keep the tungsten divertor from melting. Even though testing LMD technologies supported by impurity seeding is an interesting concept, the first stage of testing should focus solely on the liquid metal divertor, as the impurity seeding would bring more complexity impeding interpretation of the experiment.
The reasons mentioned resulted in a change of the assumed regime for the first liquid metal experiments to a regime with lower parameters (e.g. #3200, in Tab. 4.2).

4.4 Simulations of COMPASS-U scenario #3200

The effect of electron temperature change

As mentioned in the previous section, the idea to utilize scenario #3200 instead of the scenario with maximal power #6400, is derived from the melting of the tungsten divertor, without countermeasures. The lower power loads of the utilized scenario (See Tab. 4.2) would not be sufficient to achieve notable results, i.e. testing the limits of the LMD technologies. For this reason, a cylindrical target inserted into plasma, above the divertor is assumed, similarly to the COMPASS LMD experiments [80]. The increased incidence angle results with higher heat fluxes. $q_\perp = \sin(3°)q_\parallel \approx 0.05q_\parallel$ versus $q_\perp = \sin(45°)q_\parallel \approx 0.71q_\parallel$ (Fig. 3.2). More on this subject in [56, 80]. The increased heat flux (and shocks of transients) will result in higher surface temperature, and subsequent particle release, allowing a more detailed study of the effectiveness of the heat shield and the effect of the released atoms on the plasma.

Apart from the incident heat flux, the other two most important quantities in LMD performance are the plasma (electron) temperature and density (See Section 3.1). It is therefore crucial to assess the values of these quantities correctly, otherwise the results of the simulations might be incorrect. For example, concerning the electron temperature, which influences the radiation vapor cooling, if the temperature changes from 10 eV to 100 eV, the per particle cooling changes by a factor of 50 (See Fig. 2.13). The change in the expected temperature results in a change of electron density as well, which also effects the vapor cooling power significantly.
The agreed upon temperature range for COMPASS-U scenario #3200 is 10-30 eV (See Section 4.2.2). For this reason, two simulations with a lithium wetted target have been done, to evaluate the effect of the temperature change. The complete notable results are in Fig. 7.4 and Fig. 7.5. The most important parameters for the heat shield and the effect on plasma is the surface temperature at which the thermal equilibrium is achieved and the number of released atoms. The comparison between those two is in Fig. 4.8.

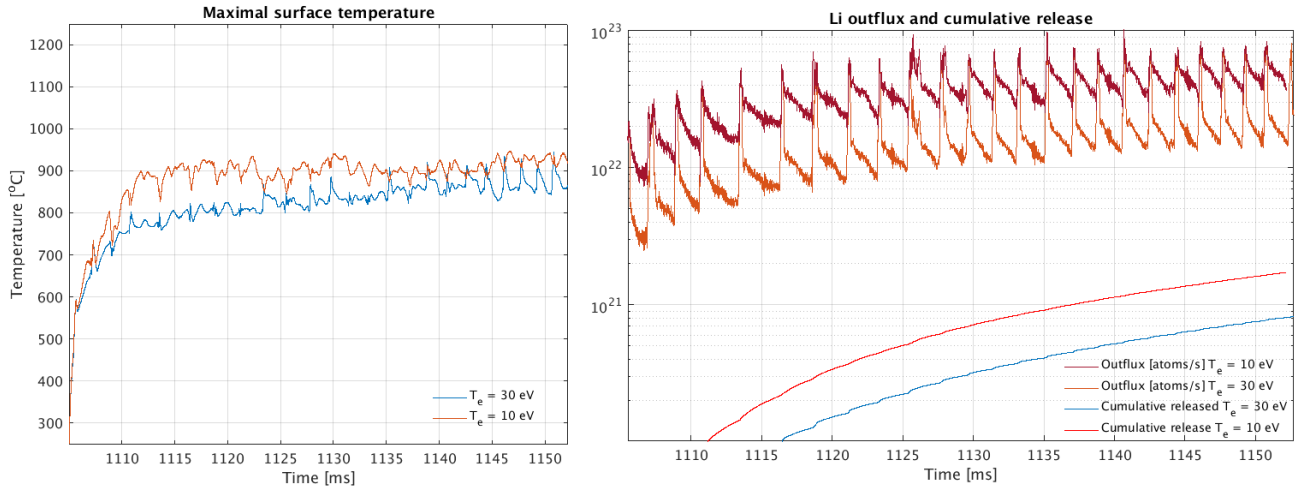

Fig. 4.8: Comparison of the maximal surface temperature (left) and particle release, both out-flux and cumulative release, (right) over time for the LMD cylindrical target simulations in the $T_e = 10$ eV and $T_e = 30$ eV cases of the COMPASS-U scenario #3200.

The temperature difference of the two scenarios is approximately 100 °C in the first half of the simulation, however the temperature of the target in the 30 eV simulation rises after $t = 1130$ ms to approximately 850 $°C$, but the fluctuation increases as well, prohibiting any concrete conclusion. It can be stated, that at the temperature difference is not substantial and will have no effect on the cooling and power handling of the LMD target (excluding vapor cooling).
The difference in vapor cooling capabilities is apparent in the second graph (right in Fig. 4.8). The inter-ELM out-flux, and cumulative release, is three times lower for the 30 eV case. As the conductive cooling is essentially the same, the only reason for the lower particle release in the 30 eV scenario is an increased per particle cooling capability. This result indicates that an operation regime with higher temperature is more favorable under COMPASS-U conditions. In the next COMPASS-U simulations presented in this thesis, only the 30 eV scenario has been arbitrarily assumed, as it is still unclear, which value of the divertor electron temperature is correct.
During ELMs, where the electron temperature and density is the same for both scenarios, the out-flux reaches the same values, which is an expected result, as the vapor cooling capabilities are the same in that instance, as the two scenarios differ only in the inter-ELM phase.
It is apparent from the temporal evolution of the maximal surface temperatures in both scenarios (Fig. 4.8), that a quasi-stable state is achieved after 10 ms of rapid surface temperature increase. This is caused by the prompt response of the vapor shielding effect to the conditions at the surface of the LMD (ion flux from plasma, surface temperature, electron temperature etc.). Since the vapor cooling power exceeds 100 MW/m^2 at the point of maximal temperature, any active cooling system would play a negligible role in the power balance. The surface temperature is either too low to create a sufficient temperature gradient, or the vapor shielding effect will be significantly larger than the conduction cooling, limited by the ability of the cooling system (See Section 1.9.4).

Cylindrical target simulations

One of the most important questions, in the liquid metal heat shield research is, which wetting metal is the most beneficial. Currently the most investigated candidates are lithium, tin and 0.75Sn0.25Li alloy (See Section 2.2). Simulations for each candidate have been done for the 30 eV

scenario #3200 with the cylindrical target, as each can be potentially tested at COMPASS-U. The complete notable results are in Fig. 7.5, Fig. 7.6 and Fig. 7.7.

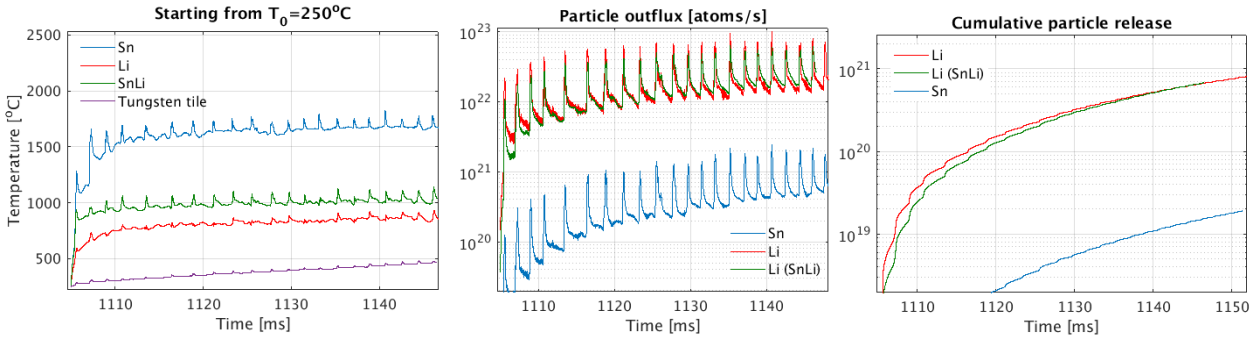

Fig. 4.9: Comparison of the surface temperature (left), particle out-flux (middle) and cumulative release (right) over time, for lithium, tin-lithium alloy, and tin wetted target for the COMPASS-U scenario #3200 with $T_e = 30$ eV.

The main difference between the possible candidates is again in the surface temperature and the particle release (Fig. 4.9). If compared with the referential tungsten tile, where the surface temperature gradually increases throughout the whole simulation, in all three LMD cases, an equilibrium is achieved, after around 10 ms. The difference between Li and SnLi alloy, 800 °C and 1000 °C respectively is caused by the lower sputtering of the alloy (0.25 of pure Li sputtering and no Sn sputtering) and lower evaporation rate of the alloy over pure lithium at a given temperature (Fig. 2.12). Thus, with essentially no conduction cooling, the offset is compensated by the higher surface temperature. The maximal surface temperature of the tin wetted target is 1700 °C, caused again by the lower evaporation rate of tin. The pure tin LMD is more efficient with an active cooling system and a potential pure tin plasma facing component would only rely on vapor cooling during non-steady state events (ELMs, disruptions etc.) as the release of tin is generally undesirable.

The Li out-flux and the cumulative release for pure lithium and SnLi alloy is almost identical. The reason is that only Li release is assumed for the alloy thus the total vapor cooling power is directly proportional to the number of released particles. This clearly shows, that the SnLi alloy is more efficient than pure lithium only with an active cooling system, where conduction cooling is relevant, similarly to pure tin. In case of the tin target, the tin release is two orders of magnitude lower, due to the fact, that tin radiates considerably more than lithium (Fig. 2.13, Fig. 2.14). It has to be noted, that the simulation covers only 50 ms. As the discharge length is more than 1 s, the total amount of released particles per one discharge is 20 times higher, than the cumulative release at the end of each simulation. For the tin target, the total release per discharge would exceed 4×10^{20} atoms, more than the line averaged plasma density (Tab. 4.2). In case of lithium release the values are orders of magnitudes larger. The study of propagation, redeposition and the overall effect on plasma by the metals is therefore imperative in LMD technology research.

Full toroidal divertor simulations

The target of the liquid metal plasma facing component research is a test of a full toroidal divertor. As the shaped inserted target shades the divertor and receives a considerable fraction of the incident heat load (1/3 in the COMPASS experiment [80, 56]), the total amount of released

particles should not be drastically different. Furthermore, the design allows for conductive cooling, either active by a coolant or a thick layer made from a conductive material such as copper, to be incorporated, decreasing the overall particle release. Simulations with Li, Sn and SnLi of a COMPASS-U full toroidal outer target divertor have been conducted.

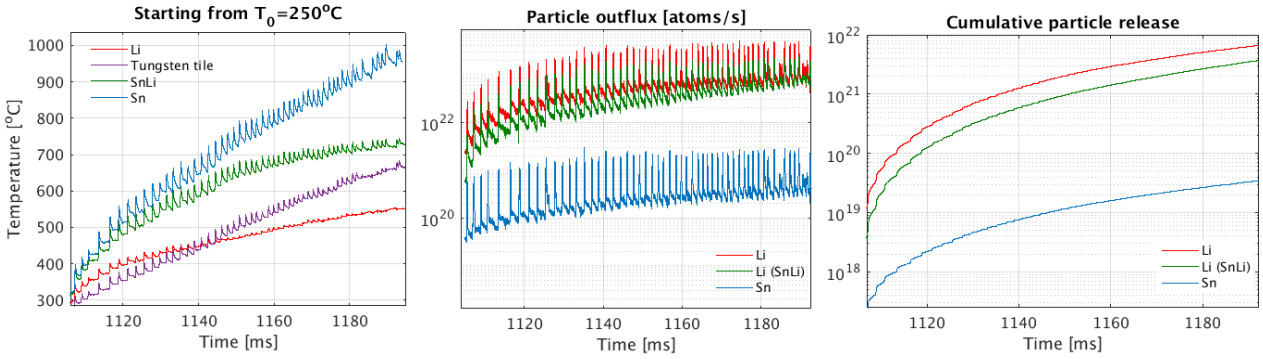

Fig. 4.10: Comparison of the surface temperature (left), particle out-flux (middle) and cumulative release (right) over time, for lithium, tin-lithium alloy and tin wetted full toroidal divertor for the COMPASS-U scenario #3200 with $T_e = 30$ eV. The out-flux is scaled from the simulated target to the whole surface of the divertor.

The most apparent feature of the temporal evolution of the maximal surface temperature is the faster temperature increase of the LMD targets over the tungsten tile (slower for pure Li where vapor shielding effects start sooner). The faster increase is caused by the lower conductivity and heat capacity of the liquid metals over tungsten (Tab. 2.1). In the simulation, where the mesh CPS technology is assumed, the conductivity is given mainly by the liquid metal, as the solid molybdenum substrate is a set of mesh layers, thus with questionable thermal conductivity, due to a large number of thermal contacts. A design, where the thermal conductivity would be given by the solid material, ideally tungsten, would further increase the LMD viability, for example the 3D-printed tungsten system (See Section 2.3). Therefore the study of thermal properties of liquid metal based structures should also be focused on.

The maximal surface temperature difference between lithium and SnLi alloy is almost two times larger than in the cylindrical target case. The reason is a strong sputtering from the pure lithium divertor. In Fig. 7.8 it can be seen that the vapor cooling is caused exclusively by sputtering (Li evaporation is low at 500 °C).
The Li out-flux from the pure lithium and SnLi alloy divertors converge to the same value, as conduction cooling importance decreases over time. The effect of conduction is clearly apparent even in these simulations, where the design is such, that conduction is as low as possible.

As explained above, the increased effect of conduction in a full toroidal divertor case over the inserted target case is apparent in the cumulative particle release of tin, which is only around on half of the release from the shaped target (at $t = 1150$ ms). In case of pure lithium, the cumulative release (at $t = 1150$ ms) is two times higher than for the target case, due to strong sputtering. The tin lithium alloy is in the middle with Li release approximately the same as from the target. This result would strongly support tin as the best LMD candidate, with the SnLi alloy being still better then pure lithium, however the considerable Li release, even from the pure Li target, might prove to be non-discrediting, as much higher concentration of lithium over tin, is acceptable in the plasma (Tab. 2.1).

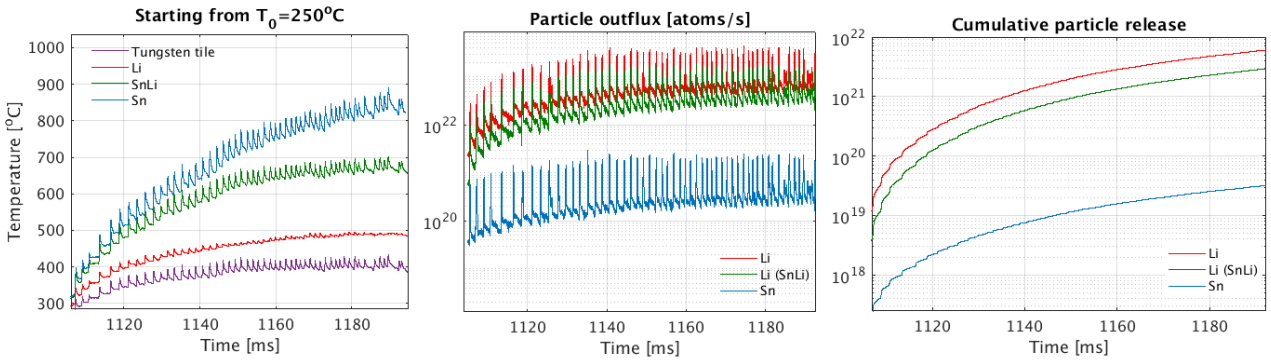

Fig. 4.11: Comparison of the surface temperature (left), particle out-flux (middle) and cumulative release (right) over time, for lithium, tin-lithium alloy and tin wetted full toroidal divertor for the COMPASS-U scenario #3200 with $T_e = 30$ eV. The out-flux is scaled from the simulated target to the whole surface of the divertor. Simulation includes an active cooling system, by having the back temperature fixed at $T_0 = 250$ °C.

The resulting maximal temperatures and particle releases of the simulations with a full toroidal divertor with an active cooling system (back temperature fixed at $T_0 = 250$ °C) in Fig. 4.11 show, that the effect of the active cooling system on the simulation result is insignificant, even though the increased conductive cooling power caused a decrease in maximal surface temperature in all three cases. The maximal surface temperature was decreased by ≈ 100 °C for tin and tin-lithium divertors and by ≈ 50 °C for the pure lithium divertor, but the impact on the out-fluxes and cumulative release is negligible.
Tin-lithium alloy divertor out-flux is the only one, with non-marginal decrease in the cumulative release. The decrease is from 4×10^{21} to 3×10^{21} or by 25 %.
The main reason for the marginal difference in particle out-fluxes is the domination of sputtering over evaporation. In case of lithium (pure Li and SnLi alloy), the thermal sputtering yield saturates at ≈ 500 °C therefore the decrease of surface temperature to 500 °C (Fig. 2.10) will not affect it. I case of tin the change of the sputtering yield is also not substantial (Fig. 2.11).
The other reason for the ineffectiveness of the active cooling system can be explained by the low thermal conductivity of the CPS layers. The conductive cooling power depends not only on the difference in temperatures, but also on thermal conductivity.
This hypothesis is supported by the considerable change in maximal surface temperature of the tungsten tile. The uncooled tile maximal surface temperature was 650 °C (not saturated), whereas the maximal surface temperature of the cooled tile was 400 °C (saturated).
These results further support the need for liquid metal thermal conductivity research with the goal of designing a liquid metal system with higher thermal conductivity (e.g. the 3D printed tungsten system or the copper poloidal trench system).
The utilization of an active cooling system is still preferred, as it is the future mode of operation in large devices (e.g. DEMO). In devices with relatively short discharges (e.g. COMPASS-U) it can be implemented through a thick highly conductive (copper) layer, that is not fully heated during the discharge.

Impact of high density on lithium and tin sputtering

The general idea of the vapor cooling concept is, that as the temperature raises, evaporation flux overtakes sputtering flux and strongly dominates. This is indeed true; however, no clear

surface temperature threshold can be determined. The reason for the inability is the linear dependence of sputtering flux on the number of impacting particles (plasma density). The sputtering yield is influenced by temperature, chemical or preferential effects, however the empirical formulas describing them (2.2), (2.3) show, these effects converge to $Y_t^{Li} \approx 3$ for Li and $Y_t^{Sn} \approx 0.2$ for tin. This means the dependency on plasma density of sputtering is approximately linear for high temperatures. Evaporation flux depends exponentially on the surface temperature.

If the plasma density is sufficient, a state where the particle exhaust is dominated by sputtering even with high heat loads, where normally the target would be heated to such extent that evaporation would dominate, can be achieved. To my best knowledge, the experiments with liquid metal plasma facing components both in linear devices and tokamaks conducted so far have not shown this effect, as the plasma density was not high enough. The simulations of the liquid metal experiment on COMPASS-U scenario #3200 (for the full toroidal divertor) show, the conditions mainly the high divertor plasma density result in heating equilibrium at the strike point of around 600 °C, around 2/3 of the temperature achieved in the COMPASS experiment [56, 80] with similar heat flux.

Power handling effects of ELMs

Another notable result is the temperature does not always spike during ELMs (in some cases even decreases). The rapid increase in the electron temperature during ELMs causes a spike in the cooling per particle energy, thus increasing the total cooling power up to ten times, with the same number of radiating atoms. As seen in Fig. 2.13 and discussed in this section, the per particle cooling energy difference in ranges of 10-100 eV can vary by factor of more than 10.

This effect of course assumes the high energy ELM electrons do collide with the exhausted neutrals and do not "burn" through the neutral cloud. It is unclear if this is the case, or for example is only under certain conditions and only for one of the metals. However, this is a complicated issue, that can probably be investigated only experimentally or through extensive kinetic modeling. If this however is the case, several advantages and disadvantages arise.

An advantage of a sputtering driven cooling over evaporation driven cooling is the prompt response to density and electron temperature spikes making the target surface temperature and exhaust flux more stable even during transient events. In case of the evaporation driven cooling, the spike in cooling with the increase of the electron temperatures occurs as well, but the inertia of the exhaust due to the crude surface temperature dependency makes the vapor cooling and exhaust not as responsive to the immediate plasma conditions as in the sputtering driven cooling regime. The main disadvantage of the liquid metal divertor is the exhaust flux. If substantial amount of the metal crosses separatrix fuel dilution or even radiation disruption can occur. As shown in Fig. 7.8, in the sputtering driven cooling regime excessive exhaust fluxes occur even with relatively low surface temperatures. Without any countermeasure to prevent the lithium atoms from crossing separatrix, sufficient active cooling would have to be provided.

Liquid metal	Li	Li	SnLi	Sn
Divertor T_e [eV]	10	30	30	30
Maximal T_{surf} [°C]	900	800	1000	1700
Active cooling (Y/N)	N	N	N	N
Inter-ELM $q_\perp$ [MW/m^2]	160	160	160	160
Sputtering cooling [MW/m^2]	60	90	10	10
Evaporation cooling [MW/m^2]	100	70	150	150
Atoms released (after 40 ms)	1×10^{21}	5×10^{20}	5×10^{20}	1×10^{19}

Tab. 4.3: Results of the COMPASS-U liquid metal experiments with the cylindrical target simulations.

Liquid metal	Li	SnLi	Sn	Li	SnLi	Sn
Maximal T_{surf} [°C]	550	730	950	500	650	850
Active cooling (Y/N)	N	N	N	Y	Y	Y
Inter-ELM $q_\perp$ [MW/m^2]	12	12	12	12	12	12
Sputtering cooling [MW/m^2]	6	5	3	3	3	0
Evaporation cooling [MW/m^2]	0	5	0	0	2	0
Atoms released (at 40 ms)	6×10^{21}	4×10^{21}	3×10^{19}	6×10^{21}	3×10^{21}	3×10^{19}

Tab. 4.4: Results of the COMPASS-U liquid metal experiments with the full toroidal divertor simulations, with $T_e = 30$ eV. The remaining power is cooled by conduction.

5. Simulations of the ALIMAT-F liquid metal experiments

5.1 ALIMAT-F device

ALIMAT-F is an experimental device currently under construction at the Institute of Plasma Physics of the Czech Academy of Sciences in Prague [92]. The device will consist of two neutral beam injectors serving as sources of high energy deuterium neutrals (plus ions), which will bombard a test target inside a vacuum chamber. The particle beams will be used to test heat shields technologies for fusion devices and other technologies requiring resistance to extreme conditions, the device can create (Tab. 5.1). The operation regimes of ALIMAT-F will allow the replication of the condition in high temperature tokamak plasma similar to H-modes (periodic short high energy ELM like pulses). The described conditions will be eligible to test the CPS technology and evaluate various concepts of its utilization as a plasma facing component.

Parameter/Regime	Baseline	With residual ions
Pulse length [s]	2	2
Particle energy [keV]	80	80
Power [MW]	1	1.8
Deposition surface [m^2]	3.33×10^{-2}	3.33×10^{-2}
Heat flux [MW/m^2]	30	54

Tab. 5.1: ALIMAT-F parameters for the possible regimes of operation [92].

ALIMAT-F is based on the neutral beam injection technology. Ionized deuterium gas is accelerated in an electric field and run through the neutralizer. In the neutralizer the ions are neutralized by charge exchange. Strong magnetic field (optional) then diverts the remaining ions into a dump. This creates a beam of high energy neutral particles, targeted at the test subject. The objective of the device is not only to test heat load resistance of the tested materials but also resistance to high energy particles and neutron fluxes (secondary effect of deuterium bombardment) [92].

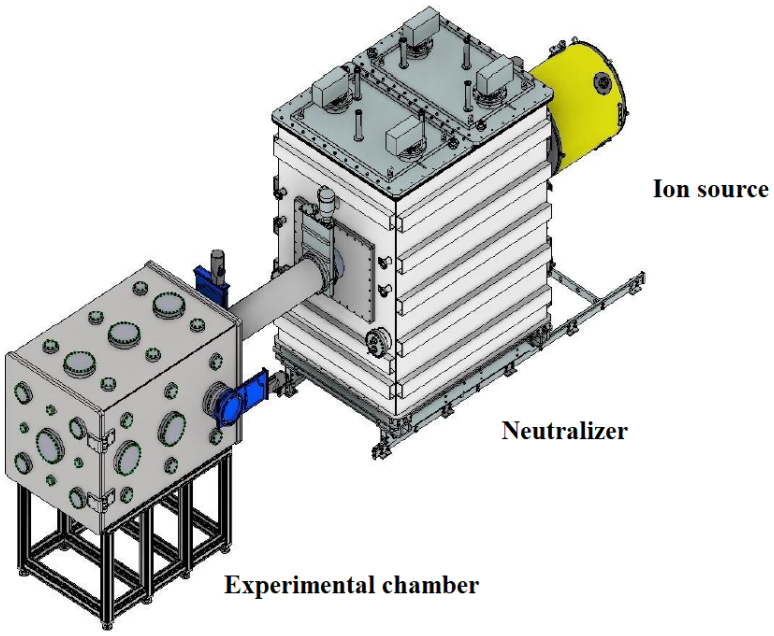

Fig. 5.1: Model of the ALIMAT-F experimental setup. Deuterium is ionized in the ion source (yellow) and is then run through the neutralizer into the experimental chamber [92].

5.2 Experiments with liquid metals on ALIMAT-F

With the energy of $E_\mathrm{k} = 80$ keV and power $P = 1$ MW, the current of the neutral beam is $I = 12.5$ A and the current density at the focal point is $j = 375$ A/m^2. The total particle impact flux will be $\Gamma_\mathrm{n} = 1.4 \times 10^{15}$ m^{-2}. This means the sputtering caused by the impact of the neutrals will be negligible in comparison to the evaporation, for the following reasons. The current density at tokamak divertor, where sputtering is relevant is orders of magnitude higher (See. Section 4.4). The vapor cooling of the target will be also negligible. From the total energy of the neutral $E_\mathrm{k} = 80$ keV, only around 40 eV $= 80\frac{m_\mathrm{e}}{m_\mathrm{e}+m_\mathrm{p}}$ keV is carried by the electron. This would be enough to cause sufficient radiation through interaction with the released liquid metal, however the density of the beam electrons at the target will not be sufficient to accommodate relevant number of interactions with the released metal. As a result, the vapor cooling effects caused by the line radiation of the evaporated metal will also be negligible. Therefore, the only effect, apart from heat conduction, cooling the surface of the target will be the latent heat of evaporation (Tab. 2.1). The calculations assume only atomic hydrogen present in the beam, i.e. the best case scenario for the beam energy efficiency. In reality the presence of other species, such as molecular hydrogen, H_3^+, H_3O^+ etc. would only worsen the effects of radiative cooling and sputtering. However, line radiation will be an important part of the experimental diagnostics setup.
The energy cooled by one exhausted particle, given only by the latent heat, will be one to two orders of magnitude lower than in typical tokamak conditions (See. Section 4). The result of this will be a much higher equilibrium temperature at the same heat flux and thus considerably higher particle exhaust. This finding can be utilized in several ways in the tasks set for this experiment.

Heat load testing

The first and the most obvious characteristics of a LMD technology to test is the heat load endurance. The heat fluxes achievable at ALIMAT-F of up to 30 MW/m^2, are well over 16 MW/m^2 the limit predicted for ITER or DEMO (See. Sections 1.9.2 and 1.9.3). However, the ability of LMD technologies to withstand such heat fluxes has been already thoroughly tested and proven to be more than sufficient [15, 73, 93]. For this reason, the primary objective of the liquid metal experiments should be focused on different aspects of LMD operation (discussed below), and the heat flux resistance should be only of secondary importance.

Erosion of the liquid metal target by particle impact

One of the key characteristics of the liquid metal plasma facing component designs is the erosion of the PFC. Even though the liquid surface itself cannot be eroded, the particle exhaust and subsequent redeposition can play an important role in the LMD operation, especially for lithium or tin-lithium alloy, which are strongly eroded even under relatively weak conditions (See. Fig. 2.9a, 2.10 and 2.12). The question of fuel retention also persists. Even though it has been presented in [55], that at increased temperatures ($\approx$ 300-400 °C) the hydrogen retention in lithium decreases strongly, it is still highly desirable to test this capability as it can be a crucial obstacle in usage of lithium as a plasma facing component. In case of tin a crucial and potentially insurmountable obstacle in LMD usage is the formation of stannane SnH_4 and potentially bubbles of this gas [50, 57, 59]. The parameters of ALIMAT-F (1 s pulses with low fluence of highly energetic particles) are however not optimal for such study, as a steady state device with high particle fluence, such as Magnum-PSI [73] is more equipped to study this characteristics.

Liquid metal deposition on the surrounding walls

If the whole first wall of the fusion device is not deliberately covered by a liquid metal layer, deposition of the exhausted liquid metal on undesired areas is inevitable. This is a pressing issue not only because the balance of the liquid metal supply could be shifted, but also because it can deposit on surfaces, where the presence of an element with the properties of the liquid metal (Li, Sn) can be problematic, such as diagnostics or cryopumps. It is therefore crucial to study the deposition and potential collection of the exhausted metal, to evaluate if a state, where minimal amount of the metal is lost to the vessel and with acceptable effects on the rest of the equipment, can be achieved. The unique parameters and versatility of the ALIMAT-F device can serve as a valuable base for this study.

From the listed areas, the most promising to be investigated in the ALIMAT-F experiments seems to be the problem of liquid metal deposition and collection. The remaining two topics should however be also incorporated in the experiment, as both are crucial in the determination of LMD feasibility.

5.3 Simulations of liquid metal experiments on ALIMAT-F

In order to design the tested LMD target and predict its behavior under the ALIMAT-F NBI beam, simulations in the Heat3D (See. Section 3.1) code have been conducted. Both lithium and tin have been used as the wetting metal. Per the results of the COMPASS-U simulations, showing similar behavior of lithium and the tin-lithium alloy with only shifted temperature, the tin-lithium

alloy has not been employed (See. Section 4.4). As the primary objective of the experiment will be connected to the particle exhaust, the advantages of the alloy would not apply.
The baseline scenario, without residual ions, has been chosen (Tab. 5.1). If this scenario proves to be insufficient, the second scenario, with residual ions, can be used instead. A target of 40×40 cm has been chosen to be sufficiently larger than the deposition area The input parameters into the simulations are:

- $q_{\max} = 30$ MW/m^2 peak heat flux with 2D Gaussian profile (approximation of the beam profile at the focal point).
- Particle flux $\Gamma_n = 1.4 \times 10^{15}$ m^{-2}s^{-1} and particle energy $E_k = 80$ keV - based on the parameters of the NBI beam (See. Section 5.2) $\rightarrow$ minimal sputtering of the liquid metal.
- No prompt redeposition for both lithium and tin (no magnetic and electric fields assumed).
- No radiative cooling (plasma density is too low for a significant power to be radiated) $\rightarrow$ only local surface cooling by latent heat subtraction and heat conduction.

5.3.1 Results of lithium experiment simulation

The first preliminary simulation was done with a lithium target, with 1 mm CPS layer and a 2 mm BNC layer (essentially no heat conduction cooling capability). This simulation revealed that the decreased vapor cooling effect, due to insignificant radiation, results in excessive particle exhaust, dominantly by evaporation, to accommodate temperature equilibrium. The particle out-flux and the cumulative amount of released lithium is in Fig. 5.2a. The total amount of released lithium during the first 0.13 s of the discharge would be $\approx 10^{23}$. This equals to $m = 6.94 \times 10^{23}/N_A = 1.16$ g or $V_{Li} = 2.26$ cm^3 ($N_A = 6.022 \times 10^{23}$ is the Avogadro constant and 6.94 u is the atomic mass of lithium). The amount of lithium released per one discharge would therefore be more than 10 grams.

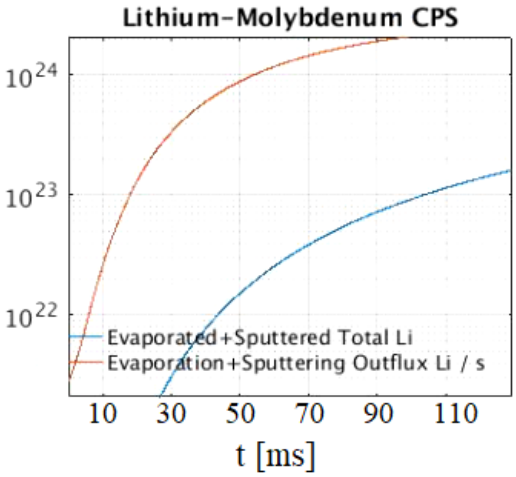

(a) Particle out-flux and total amount of released Li.

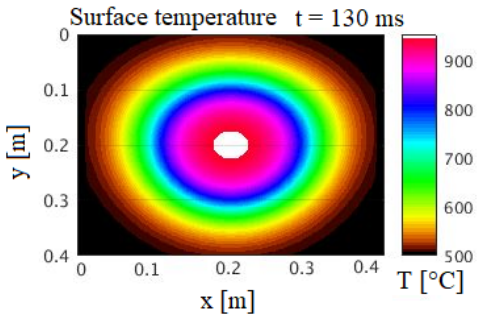

(b) Surface temperature of the target at $t = 130$ ms.

Fig. 5.2: Results of the first simulation of the ALIMAT-F LMD experiment with the 1 mm CPS layer and a 2 mm BNC layer target. First 0.1 s of the discharge simulated.

Such a large amount of lithium released during a single discharge would mean a sufficient lithium reservoir would be required for a prolonged campaign. For a campaign where dozens of discharges are desired a reservoir of more than 1000 g would be required. With the low density of lithium (0.512 g/cm^3 [61], or around one half of water density), such a large reservoir would have to be carefully designed, to accommodate the loss of lithium during the campaign, if even possible. Another issue would be the excessive lithium release itself. Release of tens of grams of lithium into the vacuum chamber could result in surface layers thick enough to prevent port window transparency and other problems with experimental and diagnostic devices to jeopardize the whole experiment.
The findings of the first simulation led to the change in the design of the test target. A 5 mm layer of copper has been added instead of the 2 mm layer of BNC to provide cooling through conduction, thus decreasing the need for excessive particle exhaust.

The change from 2 mm BNC to 5 mm copper substrate and the subsequent increase in conductive cooling capability resulted in a decrease of peak surface temperature from $T_{\max} \approx 1000$ °C in the first simulation to $T_{\max} = 850$ °C. This change in surface temperature caused a decrease in the total amount of released lithium during the first 0.1 s of the discharge to $\approx 10^{22}$ i. e. $m \approx 1$ g during the whole discharge. This is a much more favorable value for the experiment and for the design of the target.

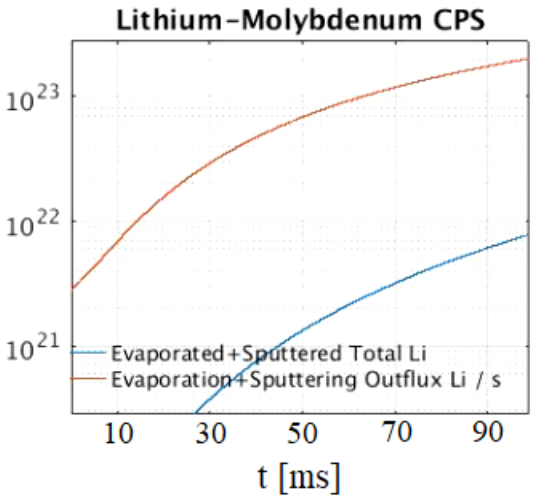

(a) Particle out-flux and total amount of released Li.

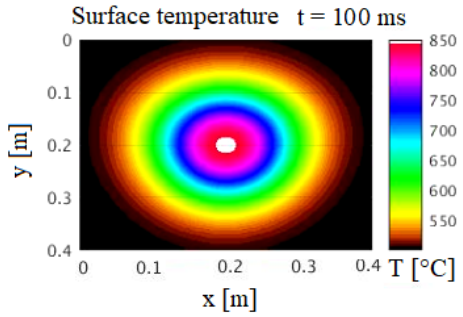

(b) Surface temperature of the target at $t = 100$ ms.

Fig. 5.3: Results of the final simulation of the ALIMAT-F LMD experiment with the 1 mm CPS layer and a 5 mm copper layer target. First 0.1 s of the discharge simulated.

The simulation shows, the design of the target is crucial for the performance. For example, if an active cooling system was installed, the total amount of exhausted lithium would drop even further. However, as the primary objective of the experiment should be studying of the exhaust effects, the active cooling system would be redundant, if not even counterproductive.

5.3.2 Results of tin experiment simulation

The main advantage of tin in case of LMD technologies over other potential candidates (Li, Sn-Li) is the low evaporation/sputtering rates and higher radiative cooling power per one particle

(See 2.5). For this reason orders of magnitude lower number of released tin atoms are required to cool a given heat load. However, this only applies on tokamak (or similar conditions), high electron temperature and density, required for sufficient radiative cooling (See 4.4). If the temperature and density conditions prohibit relevant radiative cooling (in ranges of MW/m^2), the vapor cooling behavior of a lithium and tin surfaces becomes much more similar. This is due to the lower ratio of cooling power per particle released. Assuming two scenarios, with radiative cooling (tokamak relevant $n_e = 10^{20}$ m^{-3}, $T_e = 30$ eV and cooling residence time $\tau_r = 10^{-5}$ s) and without radiative cooling, the difference in lithium and tin cooling becomes apparent:

- **With radiative cooling** For $n_e = 10^{20}$ m^{-3} and $T_e = 30$ eV the total energy cooled by one lithium atom $E_{Li} = \left(L_v^{Li} + \epsilon_{cool}^{Li}\right) = 1.41 + 40 = 41.41$ eV and by one tin atom $E_{Sn} = \left(L_v^{Sn} + \epsilon_{cool}^{Sn}\right) = 3.07 + 600 = 603.07$ eV (data in Fig. 2.13 and Fig. 2.14). The ratio is therefore $E_{Sn}/E_{Li} = 14.6$.
- **Without radiative cooling** If radiative cooling is taken out of the equation, and only the latent heat cooling remains, the ratio is then decreased to $E_{Sn}/E_{Li} = L_v^{Sn}/L_v^{Li} = 3.07/1.41 = 2.17$.

Important note is, that the first arbitrary scenario is by no means general, as the radiative cooling strongly depends on the temperature and density conditions, therefor the resulting ratio of cooling powers can vary accordingly. Tin however generally cools more power than lithium, just by the virtue of being a high Z impurity [44] and by higher heat conduction, as the surface temperature of liquid tin surfaces get to higher temperatures, under the same conditions, as the tin exhaust is lower when compared to lithium.
In case of the ALIMAT-F experiment, where no radiative cooling is expected, the second scenario applies. The 2.17 ratio essentially means, 2.17 times less atoms of exhausted tin are needed to cool the same amount of heat. The simulation without a copper substrate (no conductive cooling) result in total amount of released tin during the simulated time (first 0.1 s) of $\approx 3\times10^{22}$ (Fig. 5.5a). Using the same calculation as for lithium, the released amount equals to $m_{Sn} = 118.7\times3\times10^{22}/N_A = 5.91$ g or $V_{Sn} = 0.84$ cm^3 (less than half of the lithium volume released).

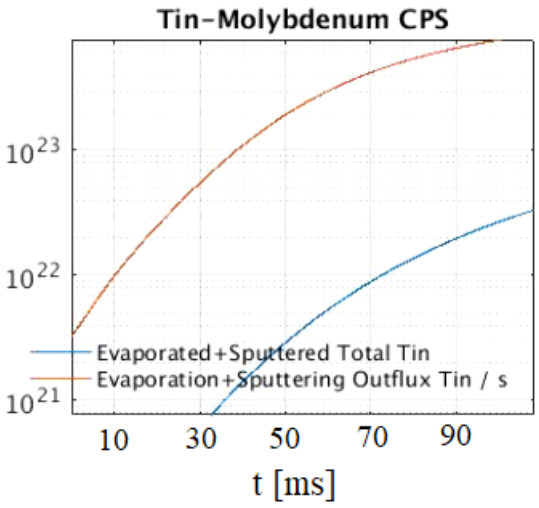

(a) Particle out-flux and total amount of released Sn.

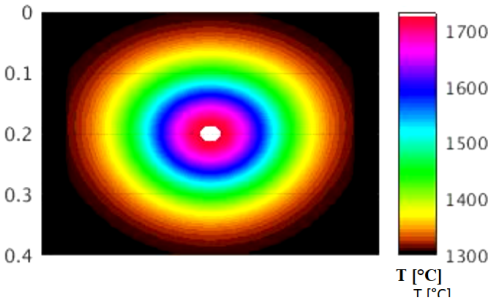

(b) Surface temperature of the target at $t = 100$ ms.

Fig. 5.4: Results of the simulation of the ALIMAT-F LMD experiment with the 1 mm CPS layer and a 2 mm BNC layer target. First 0.1 s of the discharge simulated.

The simulation of the tin target with the cooling copper layer also resulted in an out-flux decrease, as expected. The total amount of released tin during the first 0.1 s of the discharge is 1.3×10^{21} (around 0.3 g or 0.04 cm^3) a decrease by a factor of >20. The maximal surface temperature has been decreased from 2200 °C to 1750 °C. This implies the effect of an active cooling system has a strong influence on the behavior of a tin based liquid surface. In both Li and Sn cases, the effect of the copper layer can be substituted by a lower power load. However, since the copper layer heat sink can be expected to be implemented in the COMPASS-U experiments, it is more sensible to incorporate it in the ALIMAT-F experiments as well.

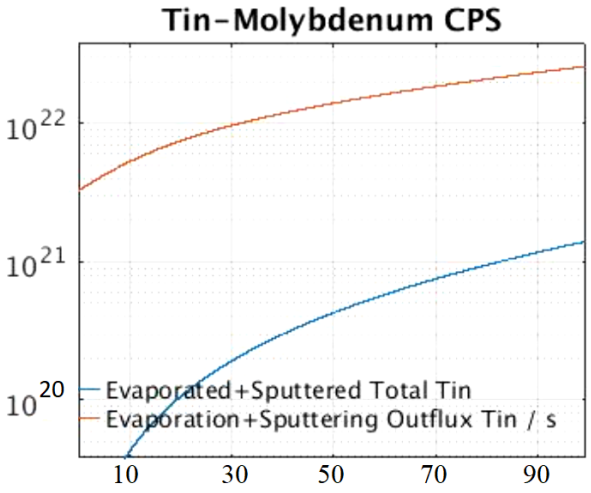

(a) Particle out-flux and total amount of released Sn.

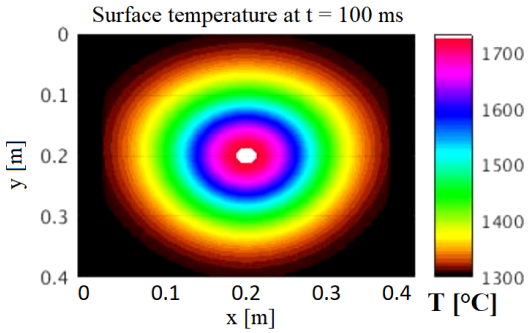

(b) Surface temperature of the target at $t = 100$ ms.

Fig. 5.5: Results of the simulation of the ALIMAT-F LMD experiment with the 1 mm CPS layer and a 5 mm copper layer target. First 0.1 s of the discharge simulated.

Liquid metal	Li	Li	Sn	Sn
Maximal T_{surf} [°C]	1000	850	2200	1750
Active cooling (Y/N)	N	Y	N	Y
Peak $q_\perp$ [MW/m^2]	30	30	30	30
Atoms released (after 100 ms)	2×10^{23}	7×10^{21}	3×10^{22}	1.3×10^{21}

Tab. 5.2: Results of the ALIMAT-F liquid metal experiments simulations. The active cooling is done through a thick copper layer.

6. Conclusion

This thesis summarized the current problems of the divertor and first wall over heating in fusion devices and focused on the potential solution of this problem through liquid metal technologies. The main part of this thesis was concerned with the simulations of the future COMPASS-U tokamak LMD experiments and the possible ALIMAT-F LMD experiments.

Liquid metals are a potential solution of the first wall over heating problem, however, excessive research is still required before a final decision regarding its viability can be made. Several approaches to the liquid metal wall are currently investigated, the mesh or felt capillary porous structure, the 3D printed structure and two flowing concepts.
The potential metals used as the liquid filler are lithium, tin, or their alloy (0.75Sn0.25Li). It is still unclear, which one will be the most efficient as each has its advantages and disadvantages over the others. Lithium is a great element in its wall conditioning properties but suffers a low boiling point and subsequent large evaporation (and sputtering) rate, at temperatures expected at fusion device operation ($\approx$ 500 °C). Tin has on the other hand comparably lower exhaust rate even at temperatures over 1200-1500 °C, well above the expected operation range. The largest and most important problem for tin, is the high atomic number ($Z = 50$), causing strong radiation even in core plasma. The tin-lithium alloy is somewhere in the middle, combining the advantages of both metals (lithium release but at higher temperatures), making it a promising candidate. Tin-lithium alloy does not oxidize. This is an important advantage especially in the upcoming experiments, where the oxidation of pure lithium could slow the experiments down and potentially set them back. In DEMO, or similar reactors, the continuous operation with minimal interference in operation might make the oxidation irrelevant. As seen in the simulations in this thesis, if sufficient cooling of the potential SnLi divertor proves to be problematic, the SnLi alloy would suffer the same problem as pure lithium. Other potential obstacle is the need for lithium replenishment in the alloy, while keeping it homogeneous.
Each of the considered metals can withstand considerable heat loads, well over the expected values at fusion power plants, meaning the practical limit for this technology will be the particle exhaust.

The simulations of the COMPASS-U LMD experiment showed, a more moderate scenario is preferable, rather than the operation scenario with the maximal power, as no heat load mitigation technique will be required. The moderate scenario #3200 will also be achievable much sooner. As the heat load will be lower a shaped target inserted above the divertor is preferable over an aligned tile. The resulting peak heat fluxes will be comparable or exceeding the heat fluxes expected for the devices with the highest energy density, making them highly relevant and important experiments. A pure lithium target and a SnLi alloy target will behave similarly under the COMPASS-U conditions, if no conductive cooling system is installed (active or passive). With no conduction cooling, the total cumulative release of lithium or tin will be high enough to be a concern. Vapor shielding effect shall be very strong dominating the temporal evolution of the surface temperature.

The experiment with a full toroidal divertor will be similar to the shaped target experiment in terms of particle exhaust. With a conduction cooling system, the particle exhaust can be even

smaller than in the shaped target experiment. This makes COMPASS-U ideal for full liquid metal toroidal divertor concept testing with ITER/DEMO relevant conditions.
The simulations also revealed an interesting behavior of the LMD in high density plasma. The pure lithium LMD power handling can be dominated by (thermal) sputtering causing considerable particle release even at relatively low temperatures (≈ 500 °C). However, it would provide a self-regulating cooling feedback with an immediate response, making the overall temperature of the surface more stable, even during transients. Provided the lithium exhaust will not be problematic, it would create a beneficial effect for the plasma facing component temperature stability.
The presence of a dense neutral cloud of either lithium or tin can suppress the effect of ELMs on the plasma facing component surface. As the electron temperature increases during ELMs, so does the radiative cooling, mitigating the destructive effect of the ELM. This applies only if the ELMs do not "burn" through the neutral cloud, which has to be further investigated.
The simulations of the full toroidal divertors indicate with active cooling, that the low thermal conductivity of the CPS layers decrease the effectiveness of active cooling. System with higher thermal conductivity (e.g. 3D printed) are therefore potentially more viable as the conductive cooling decreases particle exhausts and should be maximized. Another option is a thinner CPS layer; however, the stability of such system would have to be proven.

The ALIMAT-F LMD experiment could provide valuable information in LMD performance, mainly in the area of lithium/tin redeposition, cleaning etc. The parameters of the experiment make it non relevant in terms of heat load resistance as the heat flux is not as high as in other past LMD experiments nor is the discharge long enough to create an environment to study fuel retention. The proposed areas of study are important in the assessment of LMD viability. The ALIMAT-F LMD experiment is therefore relevant not only for the future research of liquid metals on COMPASS-U tokamak but research of liquid metal PFC in general.

Future work

In my doctoral study I plan to continue working on the topic of liquid metals, namely, to build up on the work in this thesis. I plan to rewrite the 3DHeat code from MATLAB into Python (or C++) and make it more robust and versatile. I also plan to participate and conduct the experiments modeled in this thesis, as well as cooperate with other teams working on the topic of liquid metal plasma facing components, especially with the usage of the 3DHeat code.

7. Attachments

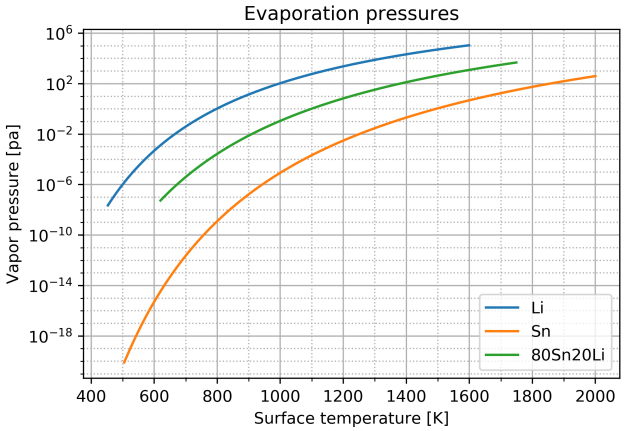

Fig. 7.1: Evaporation pressures of Li, Sn and 80Sn20Li alloy, from melting to boiling points [62, 25, 74].

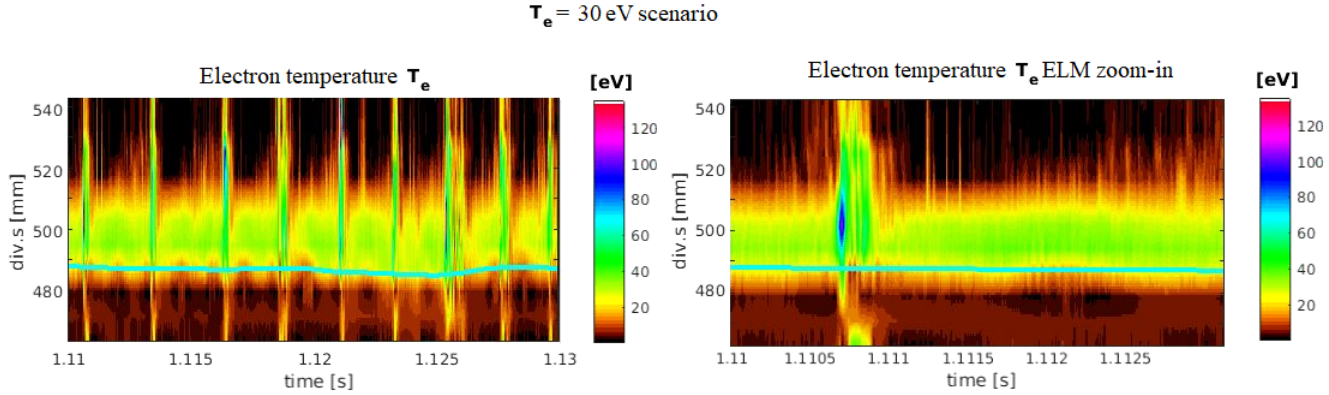

Fig. 7.2: Electron temperature profile during a part of COMPASS-U flat top phase (t = 1.11-1.13 s) of scenario #3200 with T_e = 30 eV, scaled from COMPASS divertor probes measurements (left) and ELM zoom-in (right).

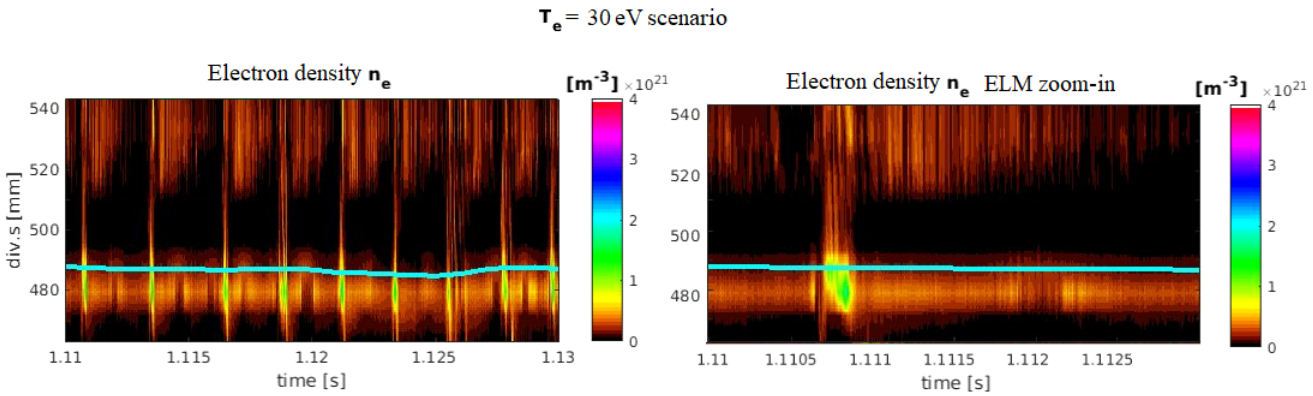

Fig. 7.3: Electron density profile during a part of COMPASS-U flat top phase (t = 1.11-1.13 s) of scenario #3200 with T_e = 30 eV, scaled from COMPASS divertor probes measurements (left) and ELM zoom-in (right).

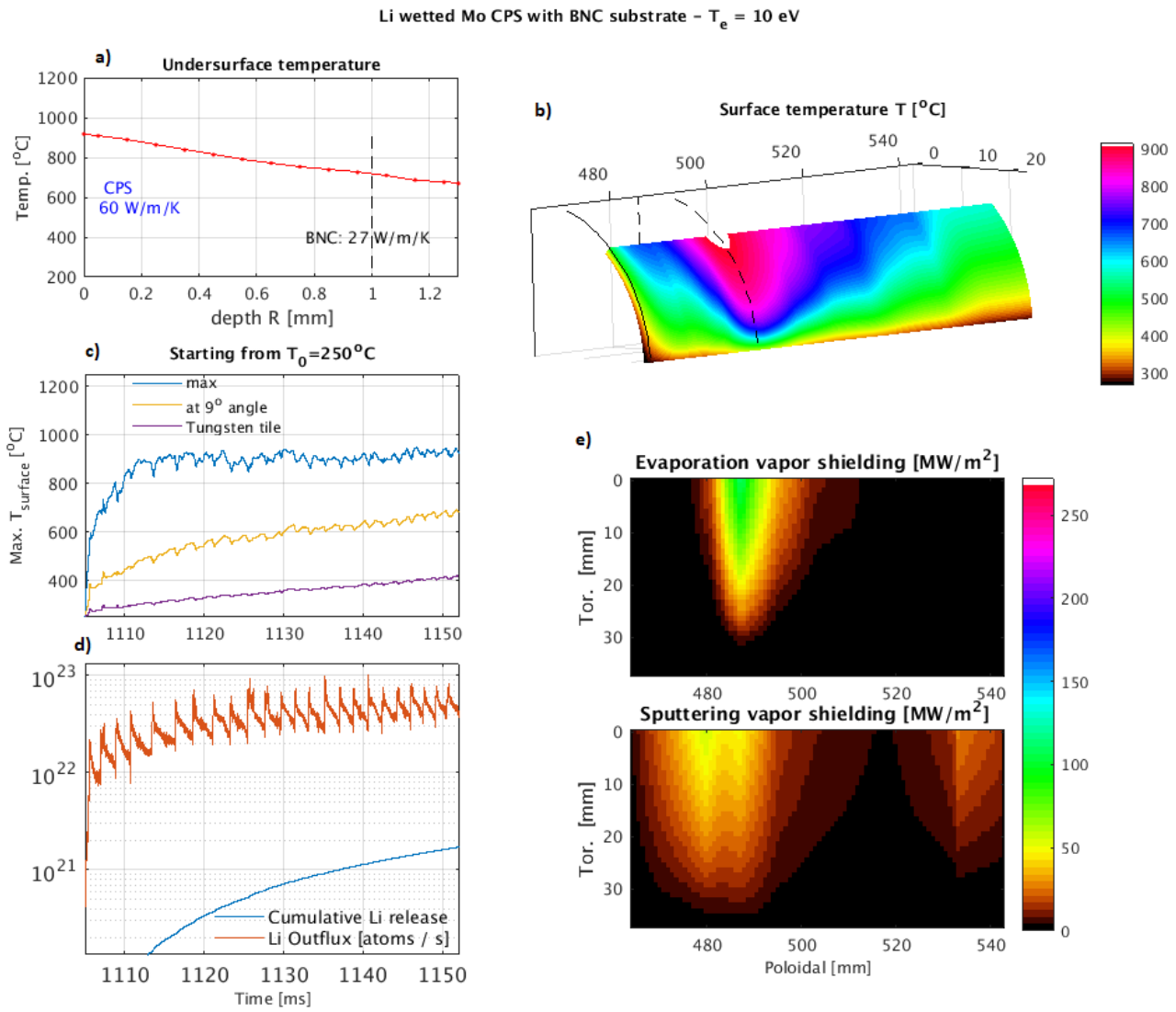

Fig. 7.4: Notable results of the Li LMD cylindrical target simulation for the COMPASS-U scenario #3200 with $T_e = 10$ eV. a) Undersurface temperature profile at the hotspot b) Surface temperature of the target c) Temporal evolution of the maximal surface temperature and surface temperature of the referential tungsten tile d) Li outflux from the target and cumulative release over time e) Vapor cooling power profile from evaporated (top) and sputtered (bottom) particles at the end of the simulation $t = 1151$ ms.

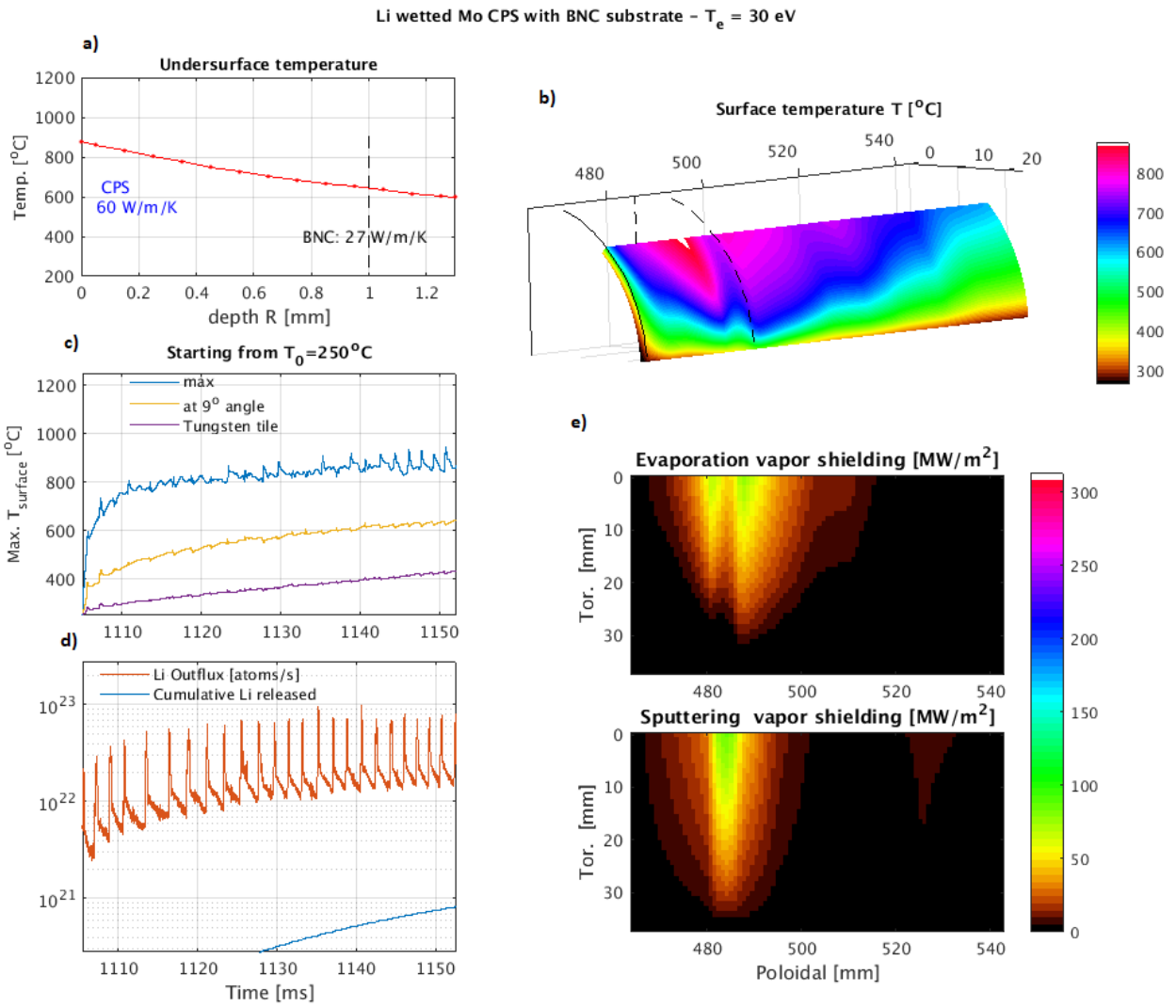

Fig. 7.5: Notable results of the Li LMD cylindrical target simulation for the COMPASS-U scenario #3200 with $T_e = 30$ eV. a) Undersurface temperature profile at the hotspot b) Surface temperature of the target c) Temporal evolution of the maximal surface temperature surface and temperature of the referential tungsten tile d) Li outflux from the target and cumulative release over time e) Vapor cooling power profile from evaporated (top) and sputtered (bottom) particles at the end of the simulation $t = 1151$ ms.

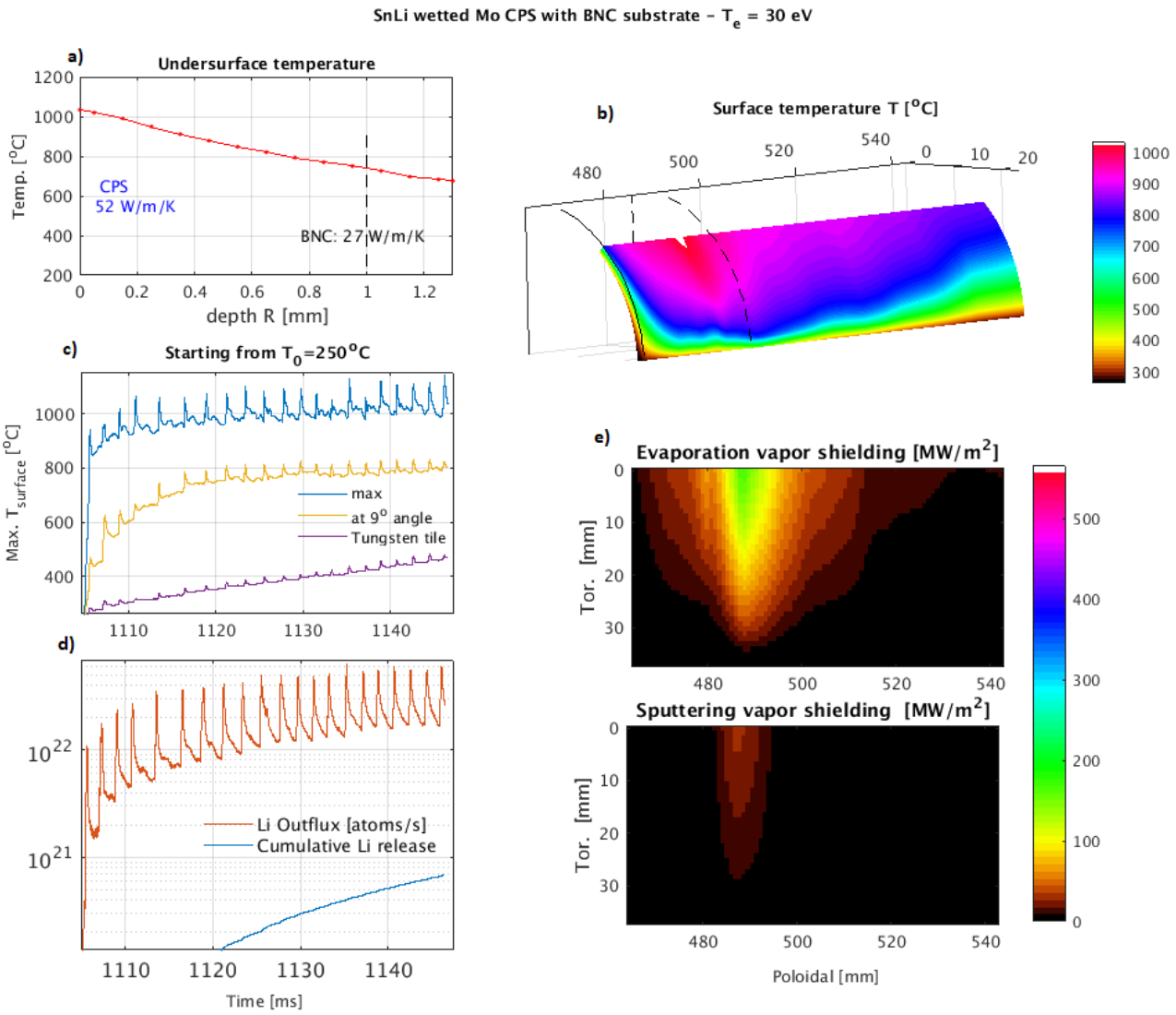

Fig. 7.6: Notable results of the SnLi LMD cylindrical target simulation for the COMPASS-U scenario #3200 with $T_e = 30$ eV. a) Undersurface temperature profile at the hotspot b) Surface temperature of the target c) Temporal evolution of the maximal surface temperature and surface temperature of the referential tungsten tile d) Li outflux from the target and cumulative release over time e) Vapor cooling power profile from evaporated (top) and sputtered (bottom) particles at the end of the simulation $t = 1151$ ms.

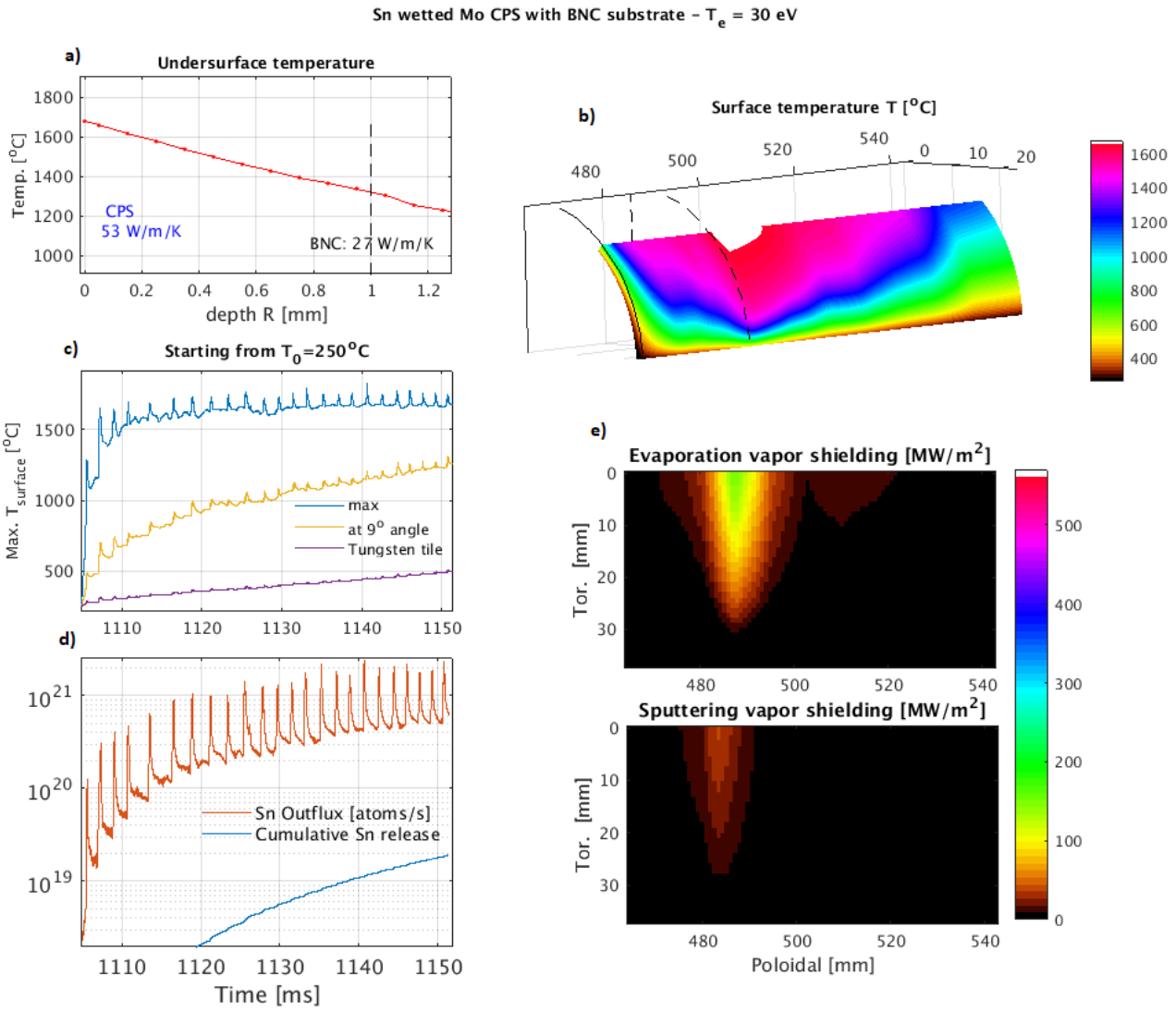

Fig. 7.7: Notable results of the Sn LMD cylindrical target simulation for the COMPASS-U scenario #3200 with $T_e = 30$ eV. a) Undersurface temperature profile at the hotspot b) Surface temperature of the target c) Temporal evolution of the maximal surface temperature and surface referential tungsten tile d) Li outflux from the target and cumulative release over time e) Vapor cooling power profile from evaporated (top) and sputtered (bottom) particles at the end of the simulation $t = 1151$ ms.

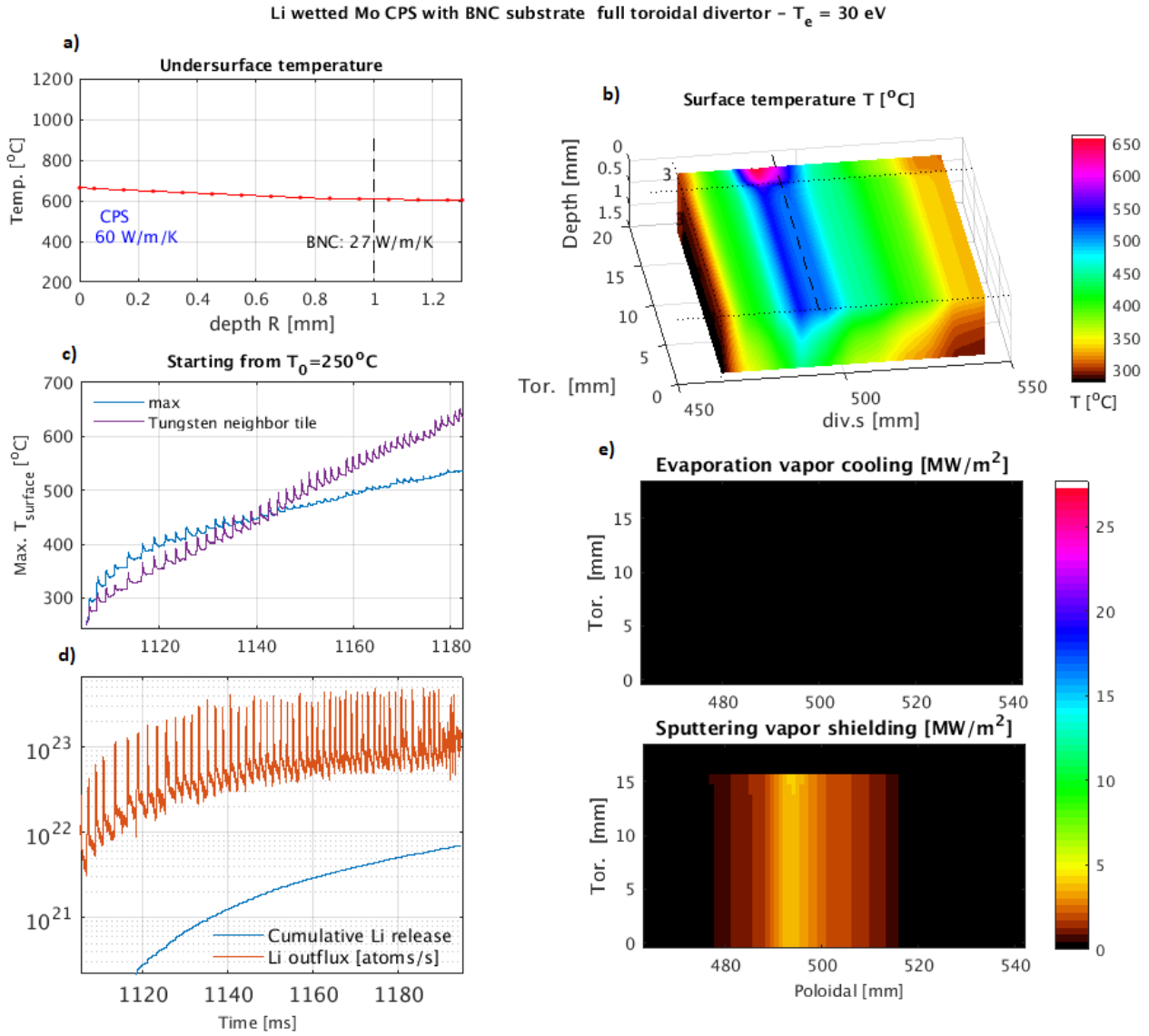

Fig. 7.8: Notable results of the full toroidal Li LMD target simulation for the COMPASS-U scenario #3200 with $T_e = 30$ eV. a) Undersurface temperature profile at the hotspot b) Surface temperature of the simulated tile c) Temporal evolution of the maximal surface temperature of the LMD and the surface temperature of the referential tungsten tile d) Li outflux and cumulative release over time (simulated tile scaled to the whole surface of the divertor) e) Vapor cooling power profile from evaporated (top) and sputtered (bottom) particles at the end of the simulation $t = 1200$ ms.

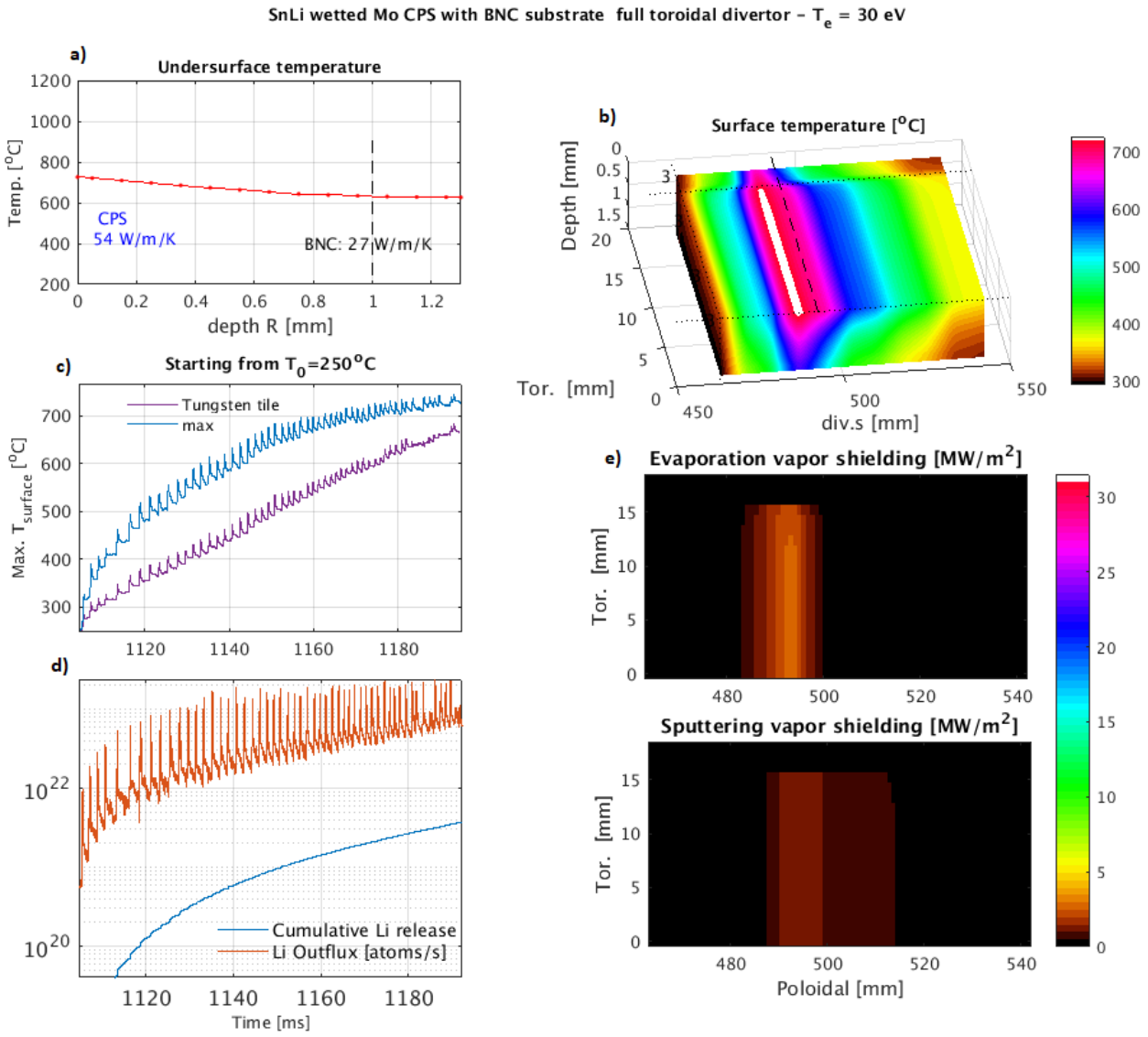

Fig. 7.9: Notable results of the full toroidal SnLi LMD target simulation for the COMPASS-U scenario #3200 with $T_e = 30$ eV. a) Undersurface temperature profile at the hotspot b) Surface temperature of the simulated tile c) Temporal evolution of the maximal surface temperature of the LMD and the surface temperature of the referential tungsten tile d) Li outflux and cumulative release over time (simulated tile scaled to the whole surface of the divertor) e) Vapor cooling power profile from evaporated (top) and sputtered (bottom) particles at the end of the simulation $t = 1200$ ms.

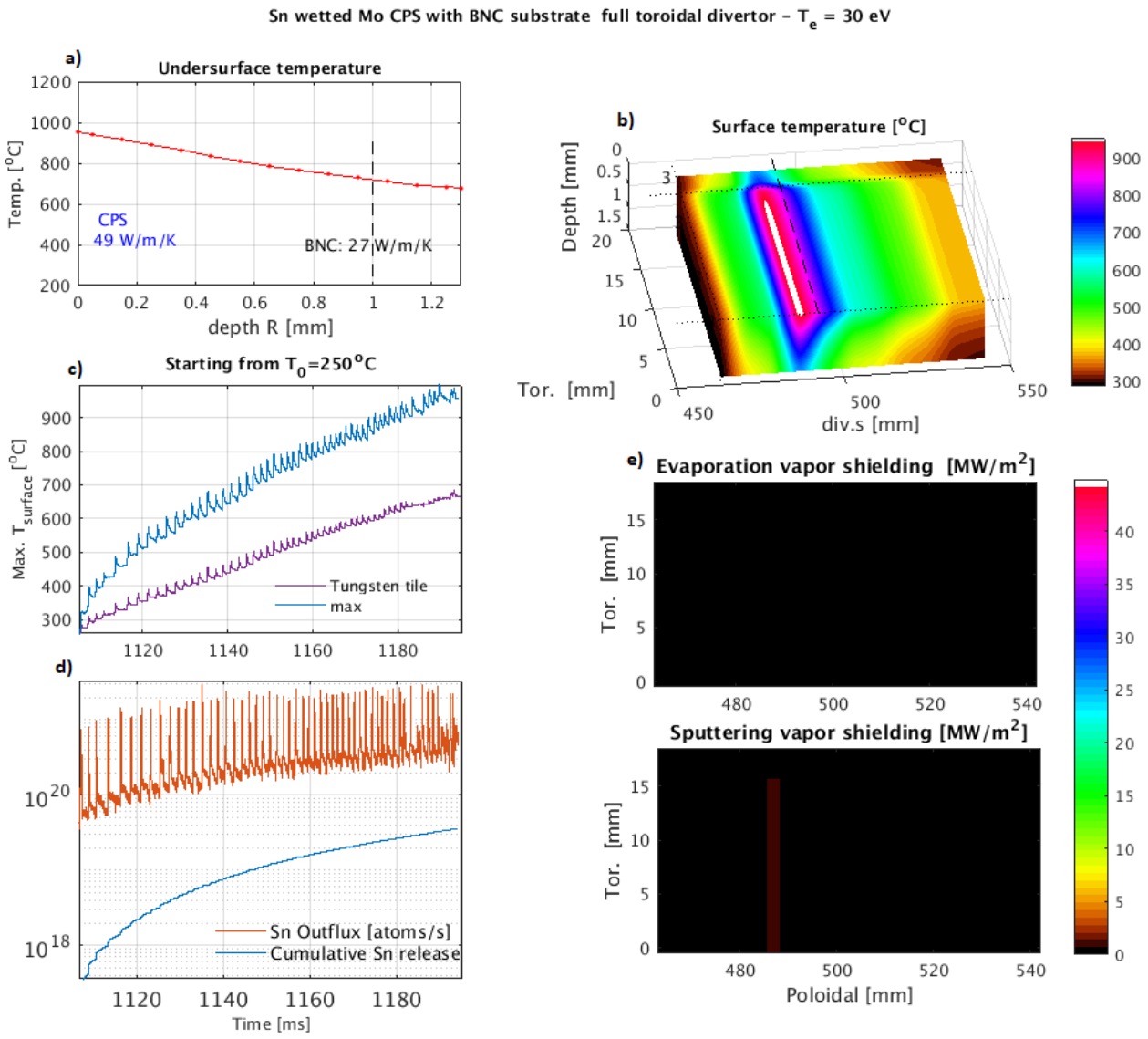

Fig. 7.10: Notable results of the full toroidal Sn LMD target simulation for the COMPASS-U scenario #3200 with $T_e = 30$ eV. a) Undersurface temperature profile at the hotspot b) Surface temperature of the simulated tile c) Temporal evolution of the maximal surface temperature of the LMD and the surface temperature of the referential tungsten tile d) Li outflux and cumulative release over time (simulated tile scaled to the whole surface of the divertor) e) Vapor cooling power profile from evaporated (top) and sputtered (bottom) particles at the end of the simulation $t = 1200$ ms.

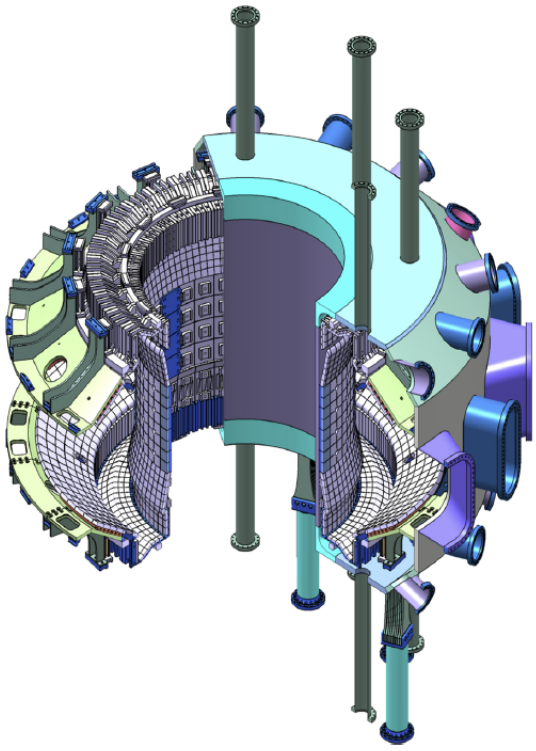

Fig. 7.11: Schematics of the COMPASS-U plasma facing components. Courtesy of [84].

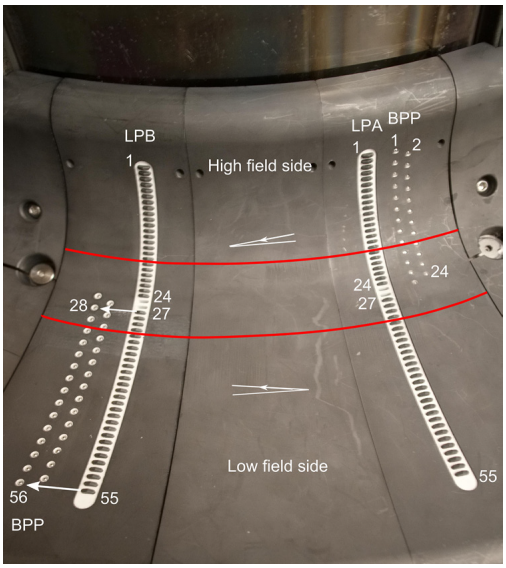

Fig. 7.12: The new COMPASS divertor probe array with two sets of Langmuir probes LPA and LPB and a set of ball-pen probes BPP. The red lines indicate the approximate positions of the strike points during the flattop of a L-mode discharge (#13025). Courtesy of [11].

Bibliography

[1] Petr Kulhánek. *Úvod do teorie plazmatu*. AGA, Prague, Czech Republic, 2011.

[2] A. S. Eddington. The Internal Constitution of the Stars. *The Scientific Monthly*, 11(4):297–303, 1920. URL: https://www.jstor.org/stable/6491.

[3] Edward Morse. *Nuclear Fusion*. Springer Nature Switzerland, Cham,Switzerland, 2018. doi: https://doi.org/10.1007/978-3-319-98171-0.

[4] Eurofusion. 50 years of Lawson criteria. Accessed: 2005-12-3. URL: https://www.euro-fusion.org/fileadmin/user_upload/Archive/wp-content/uploads/2005/12/dec05-jg04-480-2c-m.jpg.

[5] Hartmut Zohm. *Magnetohydrodynamic Stability of Tokamaks*. John Wiley & Sons Incorporated, Wienheim, Germany, 2015.

[6] Richard A. Pitts. Fusion: the way ahead. *Physics World*, 19, 2006. URL: https://physicsworld.com/a/fusion-the-way-ahead/.

[7] Peter C. Stangeby. *The Plasma Boundary of Magnetic Fusion Devices*. IOP Publishing, Bristol, UK, 2000.

[8] M. Keilhacker. H-mode confinement in tokamaks. *Plasma Physics and Controlled Fusion*, 29:1401–1413, 1987. doi:https://doi.org/10.1088/0741-3335/29/10A/320.

[9] JET-EFDA. Limiters and Divertors, 2011.

[10] Jan Horáček et al. Narrow heat flux channels in the COMPASS limiter scrape-off layer. *Journal of Nuclear Materials*, 463:385–388, 2015. doi:https://doi.org/10.1016/j.jnucmat.2014.11.132.

[11] J. Adámek et al. Electron temperature and heat load measurements in the COMPASS divertor using the new system of probes. *Nuclear Fusion*, 57(11), 2017. doi:https://doi.org/10.1088/1741-4326/aa7e09.

[12] Jan Horáček. Turbulent structures in tokamaks. Master's thesis, Faculty of mathematics and physics, Charles University, Prague, Czech Republic, 2000.

[13] A. W. Leonard. Plasma detachment in divertor tokamaks. *Plasma Physics and Controlled Fusion*, 60(4), 2018. doi:https://doi.org/10.1088/1361-6587/aaa7a9.

[14] T. Ravensbergen et al. Real-time feedback control of the impurity emission front in tokamak divertor plasmas. *Nature Communications*, 12, 2021. doi:https://doi.org/10.1038/s41467-021-21268-3.

[15] Jan Horáček et al. Plans for Liquid Metal Divertor in Tokamak Compass. *Plasma Physics Reports*, 44:652–656, 2018. doi:https://doi.org/10.1134/S1063780X18070024.

[16] John Reel Walk. *Pedestal Structure and Stability in High-Performance Plasmas on Alcator C-Mod*. PhD thesis, Department of Nuclear Science and Engineering, Massachusetts Institute of Technology, Cambridge, MA, US, 2014.

[17] François Orain. *Edge Localized Mode control by Resonant Magnetic Perturbations in tokamak plasmas*. PhD thesis, Université d'Aix-Marseille, Marseille, France, 2014.

[18] K. Farrell, A. C. Schaffhauser, and J. O. Stiegler. Recrystallization, grain growth and the ductile-brittle transition in tungsten sheet. *Journal of Less Common Metals*, 13(2):141–155, 1967. doi:https://doi.org/10.1016/0022-5088(67)90177-4.

[19] Thomas Eich et al. ELM divertor peak energy fluence scaling to ITER with data from JET, MAST and ASDEX upgrade. *Nuclear Materials and Energy*, 12:84–90, 2017. doi:https://doi.org/10.1016/j.nme.2017.04.014.

[20] Jan Horáček. Heat Transport in Tokamak Plasma Boundary. https://www.researchgate.net/publication/336375219_Horacek_Res_Prof_thesis_short_A5_version, 2019. Research prof. thesis, IPP CAS.

[21] M. A. Jaworski et al. Liquid lithium divertor characteristics and plasma–material interactions in NSTX high-performance plasmas. *Nuclear Fusion*, 53(8), 2013. doi:https://doi.org/10.1088/0029-5515/53/8/083032.

[22] Amir Faghri and Yuwen Zhang. *Transport Phenomena in Multiphase Systems*. Academic Press, Burlington, MA, USA, 2006. doi:https://doi.org/10.1016/B978-0-12-370610-2.50002-7.

[23] C. Scott and S. Derry. Catalytic recombination and Space Shuttle heating. *3rd Joint Thermophysics, Fluids, Plasma and Heat Transfer Conference*, 1982. doi:https://doi.org/10.2514/6.1982-841.

[24] Richard A. Pitts et al. Physics basis for the first ITER tungsten divertor. *Nuclear Materials and Energy*, 20, 2019. doi:https://doi.org/10.1016/j.nme.2019.100696.

[25] F. L. Tabarés et al. Reactor plasma facing component designs based on liquid metal concepts supported in porous systems. *Nuclear Fusion*, 57(1), 2017. doi:https://doi.org/10.1088/0029-5515/57/1/016029.

[26] Raphaël Mitteau et al. The design of the ITER first wall panels. *Nuclear Materials and Energy*, 88:568–570, 2013. doi:https://doi.org/10.1016/j.fusengdes.2013.05.030.

[27] M. Kocan et al. Impact of a narrow limiter SOL heat flux channel on the ITER first wall panel shaping. *Nuclear Fusion*, 55(3), 2015. doi:https://doi.org/10.1088/0029-5515/55/3/033019.

[28] G.F.Matthews et al. Steady State and Transient Power Handling in JET. *19th Fusion Energy Conference, 14–19 October 2002, Lyon, France*, 2002.

[29] Richard A. Pitts et al. A full tungsten divertor for ITER: Physics issues and design status. *Journal of Nuclear Materials*, 438:S48–S56, 2013. doi:https://doi.org/10.1016/j.jnucmat.2013.01.008.

[30] Richard A. Pitts et al. Physics conclusions in support of ITER W divertor monoblock shaping. *Nuclear Materials and Energy*, 12:60–74, 2017. doi:https://doi.org/10.1016/j.nme.2017.03.005.

[31] Thomas Eich et al. Empiricial scaling of inter-ELM power widths in ASDEX Upgrade and JET. *Journal of Nuclear Materials*, 438:S72–S77, 2013. doi:https://doi.org/10.1016/j.jnucmat.2013.01.011.

[32] A. Loarte et al. High confinement/high radiated power H-mode experiments in Alcator C-Mod and consequences for International Thermonuclear Experimental Reactor (ITER) $Q_{DT} = 10$ operation. *Physics of Plasmas*, 18(5), 2011. doi:https://doi.org/10.1063/1.3567547.

[33] C. S. Chang et al. Constructing a new predictive scaling formula for ITER's divertor heat-load width informed by a simulation-anchored machine learning. *Physics of Plasmas*, 28(2), 2021. doi:https://doi.org/10.1063/5.0027637.

[34] Ze-Yu. Li et al. Prediction of divertor heat flux width for ITER using BOUT++ transport and turbulence module. *Nuclear Fusion*, 60(2), 2019. doi:https://doi.org/10.1088/1741-4326/ab5cdb.

[35] M.N.A. Beurskens et al. Pedestal and ELM response to impurity seeding in JET advanced scenario plasmas. *Nuclear Fusion*, 48(9), 2008. doi:https://doi.org/10.1088/0029-5515/48/9/095004.

[36] C. Giroud et al. Impact of nitrogen seeding on confinement and power load control of a high-triangularity JET ELMy H-mode plasma with a metal wall. *Nuclear Fusion*, 53(11), 2013. doi:https://doi.org/10.1088/0029-5515/53/11/113025.

[37] Jan Horáček et al. Feasibility study of fast swept divertor strike point suppressing transient heat fluxes in big tokamaks. *Fusion Engineering and Design*, 123:646–649, 2017. doi:https://doi.org/10.1016/j.fusengdes.2017.01.027.

[38] Gianfranco Federici et al. DEMO design activity in Europe: Progress and updates. *Fusion Engineering and Design*, 136:729–741, 2018. doi:https://doi.org/10.1016/j.fusengdes.2018.04.001.

[39] A. Q. Kuang et al. Divertor heat flux challenge and mitigation in SPARC. *Journal of Plasma Physics*, 86(5), 2020. doi:https://doi.org/10.1017/S0022377820001117.

[40] Frédéric Escourbiac et al. Experimental optimisation of a hypervapotron† concept for ITER plasma facing components. *Fusion Engineering and Design*, 66–68:301–304, 2003. doi:https://doi.org/10.1016/S0920-3796(03)00172-8.

[41] J. Milnes and B. Chuilon. JET Neutral Beam – Recent Structural Integrity Issues, 2007. CD/E&CG/T/086, UKAEA Fusion.

[42] Joseph Milnes. *Computational Modelling of the HyperVapotron Cooling Technique for Nuclear Fusion Applications*. PhD thesis, Cranfield University, Cranfield, UK, 2010.

[43] Hyun kyung Chung et al. FLYCHK: Generalized population kinetics and spectral model for rapid spectroscopic analysis for all elements. *High Energy Density Physics*, 1:3–12, 2005. doi:https://doi.org/10.1016/j.hedp.2005.07.001.

[44] Thomas Pütterich et al. Determination of the tolerable concentrations in a fusion reactor using a consistent set of cooling factors. *Nuclear Fusion*, 59(5), 2019. doi:https://doi.org/10.1088/1741-4326/ab0384.

[45] Weston M. Stacey. *Fusion Plasma Physics*. Wiley-VCH, Weinheim, Germany, 2005.

[46] G. Cima. Thermal, nonthermal, and stimulated fluctuations of tokamak electron cyclotron radiation. *Review of Scientific Instruments*, 63(10), 1992. doi:https://doi.org/10.1063/1.1143639.

[47] Daniel Post et al. Calculations of energy losses due to atomic processes in tokamaks with applications to the International Thermonuclear Experimental Reactor divertor. *Physics of Plasmas*, 2, 1995. doi:https://doi.org/10.1088/1741-4326/ab7e47.

[48] Rainer Behrisch and Wolfgang Eckstein. *Sputtering by Particle Bombardment: Experiments and Computer Calculations from Threshold to MeV Energies*. Springer, Berlin, German, 2007.

[49] Tyler W. Abrams. *Erosion and Re-deposition of Lithium and Boron Coatings Under High-Flux Plasma Bombardment*. PhD thesis, Princeton University, Princeton, NJ, USA, 2015.

[50] Thomas W. Morgan et al. Interaction of a tin-based capillary porous structure with ITER/DEMO relevant plasma conditions. *Journal of Nuclear Materials*, 463:1256–1269, 2015. doi:https://doi.org/10.1016/j.jnucmat.2014.11.085.

[51] Thomas W. Morgan et al. Liquid metals as a divertor plasma-facing material explored using the Pilot-PSI and Magnum-PSI linear devices. *Plasma Physics and Controlled Fusion*, 60(1), 2018. doi:https://doi.org/10.1088/1361-6587/aa86cd.

[52] Peter Rindt et al. Power handling limit of liquid lithium divertor targets. *Nuclear Fusion*, 58(10), 2018. doi:https://doi.org/10.1088/1741-4326/aad290.

[53] Yingjie Chen et al. Investigation of Z_{eff} and impurity behaviour in lithium coating experiments with full metallic first wall in HT-7 tokamak. *Plasma Physics and Controlled Fusion*, 57(2), 2014. doi:https://doi.org/10.1088/0741-3335/57/2/025012.

[54] A. Rohollahi et al. Effects of lithium coating of the chamber wall on the STOR-M tokamak discharges. *Nuclear Fusion*, 59(7), 2019. doi:https://doi.org/10.1088/1741-4326/ab1d89.

[55] A. N. Scherbak et al. Experiments on the Capture of Li, H, and D by Lithium Collectors at Different Surface Temperatures at the T-11M Tokamak. *Plasma Physics Reports*, 44:1001–1008, 2018. doi:https://doi.org/10.1134/S1063780X18110090.

[56] Jan Horáček et al. Modeling of COMPASS tokamak divertor liquid metal experiments. *Nuclear Materials and Energy*, 25:100860, 2020. doi:https://doi.org/10.1016/j.nme.2020.100860.

[57] J. Loureiro et al. Deuterium retention in tin (Sn) and lithium–tin (Li–Sn) samples exposed to ISTTOK plasmas. *Nuclear Materials and Energy*, 12:709–713, 2016. doi:https://doi.org/10.1016/j.nme.2016.12.026.

[58] W. Ou et al. Deuterium retention in Sn-filled samples exposed to fusion-relevant flux plasmas. *Nuclear Fusion*, 60(2), 2020. doi:https://doi.org/10.1088/1741-4326/ab5cd4.

[59] W. Ou, F. Brochard, and T. W. Morgan. Bubble formation in liquid Sn under different plasma loading conditions leading to droplet ejection. *Nuclear Fusion*, 61(6), 2020. doi:https://doi.org/10.1088/1741-4326/abf9e0.

[60] John Wesson and D. J. Campbell. *Tokamaks*. OUP Oxford, Oxford,UK, 2011.

[61] J. Mikulčák et al. *Fyzikální, matematické a chemické tabulky*. SPN, Prague, Czech Republic, 1988.

[62] Masatoshi Kondo and Yuu Nakajima. Boiling points of liquid breeders for fusion blankets. *Fusion Engineering and Design*, 88:2556–2559, 2013. doi:https://doi.org/10.1016/j.fusengdes.2013.05.049.

[63] J. Ren et al. A flowing liquid lithium limiter for the Experimental Advanced Superconducting Tokamak. *Review of Scientific Instruments*, 86(2), 2015. doi:https://doi.org/10.1063/1.4907622.

[64] D.N. Ruzic et al. Lithium–metal infused trenches (LiMIT) for heat removal in fusion devices. *Nuclear Fusion*, 51(10), 2015. doi:https://doi.org/10.1088/0029-5515/51/10/102002.

[65] Peter Rindt et al. Using 3D-printed tungsten to optimize liquid metal divertor targets for flow and thermal stresses. *Nuclear Fusion*, 59(5), 2015. doi:https://doi.org/10.1088/1741-4326/ab0a76.

[66] I. E. Lyublinski and A. V. Vertkov. Comparative assessment of application of low melting metals withcapillary pore systems in a tokamak. *Fusion Engineering and Design*, 89(12):2953–2955, 2014. doi:https://doi.org/10.1016/j.fusengdes.2014.09.015.

[67] V. A. Evtikhin et al. Lithium divertor concept and results of supporting experiments. *Plasma Physics and Controlled Fusion*, 44(6), 2002. doi:https://doi.org/10.1088/0741-3335/44/6/322.

[68] Wenqiang Li et al. Thermal behavior of porous stainless-steel fiber felt saturated with phase change material. *Energy*, 55:846–852, 2013. doi:https://doi.org/10.1016/10.1016/j.energy.2013.02.064.

[69] Alexander Vertkov et al. Liquid tin limiter for FTU tokamak. *Fusion Engineering and Design*, 117:130–134, 2017. doi:https://doi.org/10.1016/j.fusengdes.2017.01.041.

[70] B. Bazylev et al. Experiments and modeling of droplet emission from tungsten under transient heat loads. *Physica Scripta*, 2009(T138), 2009. doi:https://doi.org/10.1088/0031-8949/2009/T138/014061.

[71] V. Riccardo et al. Characterization of plasma current quench at JET. *Plasma physics and Controlled Fusion*, 47:117–129, 2005. doi:https://doi.org/10.1088/0741-3335/47/1/007.

[72] R. P. Doerner et al. Measurements of erosion mechanisms from solid and liquid materials in PISCES-B. *Journal of Nuclear Materials*, 290-293:166–172, 2001. doi:https://doi.org/10.1016/S0022-3115(00)00568-7.

[73] Thomas W. Morgan et al. Power handling of a liquid-metal based CPS structure under high steady-state heat and particle fluxes. *Nuclear Materials and Energy*, 12:210–215, 2017. doi:https://doi.org/10.1016/j.nme.2017.01.017.

[74] C. B. Alcock, V. P. Itkin, and M. K. Horringan. Vapour Pressure Equations for the Metallic Elements: 298–2500K. *Canadian Metallurgical Quarterly*, 23(3):309–313, 1984. doi:https://doi.org/10.1179/cmq.1984.23.3.309.

[75] AMDIS database - FLYCHK model results, tin radiation losses. https://www-nds.iaea.org/exfor/servlet/X4sZvd?file=https://www-amdis.iaea.org/FLYCHK/ZBAR/pw050.zvd. Accessed: 2021-4-4.

[76] R. J. Goldston et al. Recent advances towards a lithium vapor box divertor. *Journal of Nuclear Materials*, 12:1118–1121, 2017. doi:https://doi.org/10.1016/j.nme.2017.03.020.

[77] Jacob Alexander Schwartz. *Experimental and modeling studies for thedevelopment of the lithium vapor-box divertor*. PhD thesis, Princeton University, Princeton, NJ, USA, 2020.

[78] Jan Čečrdle. První experiment s tekutým lithiem na divertoru tokamaku COMPASS, 2019. Facuty of Nuclear Sciences and Engineering, Czech Technical University in Prague, Bachelor's thesis.

[79] A. Wolff. Heat conduction in the divertor target plate of the ITER tokamak, 2011. Faculty of Nuclear Sciences and Physical Engineering, Czech Technical University in Prague, Bachelor's thesis.

[80] Renaud Dejarnac et al. Overview of power exhaust experiments in the COMPASS divertor with liquid metals. *Nuclear Materials and Energy*, 25:100801, 2020. doi:https://doi.org/10.1016/j.nme.2020.100801.

[81] Jan Horáček et al. Predictive modelling of liquid metal divertor: from COMPASS tokamak towards Upgrade. *Submitted to Physica Scripta*, 2021.

[82] Jan Čečrdle. Experiment with liquid lithium and tin on tokamak COMPASS divertor, 2020. Facuty of Nuclear Sciences and Engineering, Czech Technical University in Prague, Research task.

[83] Samuel Lukeš. Analýza prvního experimentu s tekutými kovy na divertoru tokamaku COMPASS, 2020. Facuty of Nuclear Sciences and Engineering, Czech Technical University in Prague, Bachelor's thesis.

[84] Petr Vondráček et al. Preliminary design of the COMPASS upgrade tokamak. *Fusion Engineering and Design*, 169:112490, 2021. doi:https://doi.org/10.1016/j.jnucmat.2014.11.085.

[85] Jean-François Artaud et al. Metis: a fast integrated tokamak modelling tool for scenario design. *Nuclear Fusion*, 58, 2018. doi:https://doi.org/10.1088/1741-4326/aad5b1.

[86] Robert J. Goldston. Heuristic drift-based model of the power scrape-off width in low-gas-puff H-mode tokamaks. *Nuclear Fusion*, 52, 2011. doi:doi:10.1088/0029-5515/52/1/013009.

[87] Lukáš Kripner et al. Equilibrium Design for the COMPASS-U Tokamak, 2018. WDS'18 Proceedings of Contributed Papers - Physics, 99-104, Matfyz Press.

[88] Jan Horáček et al. Scaling of L-mode heat flux for ITER and COMPASS-U divertors, based on five tokamak. *Nuclear Fusion*, 60(6), 2020. doi:https://doi.org/10.1088/1741-4326/ab7e47.

[89] J. Adámek et al. Fast measurements of the electron temperature and parallel heat flux in ELMy H-mode on the COMPASS tokamak. *Nuclear Fusion*, 57(2), 2017. doi:https://doi.org/10.1088/0029-5515/57/2/022010.

[90] Petr Vondráček. *Plasma Heat Flux to Solid Structures in Tokamaks*. PhD thesis, Faculty of Mathematics and Physics, Charles University, Prague, Czech Republic, 2019.

[91] A. Loarte et al. Characteristics and scaling of energy and particle losses during Type I ELMs in JET H-modes. *Plasma Physics and Controlled Fusion*, 44(9), 2002. doi:https://doi.org/10.1088/0741-3335/44/9/303.

[92] M. Jeřáb. Pokročilé technologie tekutých kovů pro fúzní aplikace na infrastruktuře COMPASS, 2007. EF18_046/0016011, Operační program výzkum, vývoj, vzdělání, MŠMT. URL: https://www.isvavai.cz/cep?s=rozsirene-vyhledavani&ss=detail&n=0&h=EF18_046%2F0016011.

[93] R. E. Nygren and F. L. Tabarés. Liquid surfaces for fusion plasma facing components—A critical review. Part I: Physics and PSI. *Nuclear Materials and Energy*, 9:6–21, 2016. doi:https://doi.org/10.1016/j.nme.2016.08.008.